Doctoral Dissertation

Formation and Evolution of Star-Forming Filaments in Molecular Clouds

分子雲における星形成フィラメントの形成と進化

Daisei Abe

Graduate School of Science,
Nagoya University

Supervisor: Shu-ichiro Inutsuka

March 29, 2023

Abstract

Recent observations of molecular clouds show that dense filaments are the sites of present-day star formation. Thus, it is necessary to understand the filament formation process because these filaments provide the initial condition for star formation. Theoretical research suggests that shock waves in molecular clouds trigger filament formation. Since several different mechanisms have been proposed for filament formation, the formation mechanism of the observed star-forming filaments requires clarification. In this study, I perform a series of isothermal magnetohydrodynamics (MHD) simulations of filament formation and identify mechanisms for filament formation. I find that the dominant filament formation mode changes with the velocity of the shock wave triggering the filament formation. Moreover, I show that strong shock waves can naturally create high-line-mass filaments such as those observed in massive star-forming regions in a short time.

Observations show that a massive star cluster formation occurs where the peak of gas column density in a cloud exceeds 10^{23} cm^{-2}. I investigate how the initial conditions of massive star formation are realized by performing MHD simulations with gas inflow duration from the boundaries as a controlling parameter. Filaments expand after the duration time for short-duration models, whereas long-duration models lead to star formation by forming massive supercritical filaments. Moreover, when the shock duration is longer than two postshock free-fall times, the peak column density of the compressed layer exceeds 10^{23} cm^{-2}, and the gravitational collapse of the layer leads that the number of OB stars expected to be formed reaches the order of ten (i.e., massive cluster formation).

The filament width is an important quantity because it determines the fragmentation scale by self-gravity. Observations show that the width takes the universal value of 0.1 pc. However, theoretically, the width of the supercritical filaments should contract by self-gravity. Recent studies suggest that massive filaments are bound by the slow shocks that are caused by accretion flows onto the filaments. As the wavefront of such slow shock is known to be unstable (slow shock instability: SSI), the accretion ram pressure can be expected to convert into thermal/turbulent pressure across the shock front that potentially maintains the width. In the scale of dense filaments, ambipolar diffusion (AD) suppresses the SSI at small scales. I investigate the influence of AD on SSI using two-dimensional (2D) MHD simulations. The results demonstrate that the most unstable scale of SSI is approximately five times the length scale of AD calculated using post-shock variables. The filament would be sandwiched between two shocks. I investigate the linear growth of two adjacent slow shocks. The results show that the odd mode is unstable, whereas the even mode is stable. Furthermore, I find that turbulence is driven as a result of the nonlinear evolution of the SSI with AD. I also performed a 3D MHD simulation with self-gravity. For a massive filament of $\sim 70\ M_{\odot}$ pc^{-1}, the profile is consistent with observations and has a width of 0.06 pc. I propose that the width is maintained by turbulent pressure driven by SSI including AD.

Acknowledgments

First of all, I would like to thank my supervisors, Prof. Tsuyoshi Inoue and Prof. Shuichiro Inutsuka. Prof. Inoue was my official supervisor from the master's course to the first year of the doctoral program, where he guided my research. Even after he moved as a professor at Konan University, we have had many discussions through online meetings and my business trips to Konan University. I believe that I could complete my doctoral thesis under his guidance. He treated us as one researcher, I could set higher goals for my research. Prof. Inutsuka has been my official supervisor since the second year of the doctoral course, but he has had many discussions with me since the master's course. He encouraged us in discussions, so we could reconfirm the importance and interest of our research. I enjoyed my research thanks to his guidance and encouragement.

I would also like to thank my co-authors of the thesis, Prof. Tomoaki Matsumoto, Dr. Rei Enokiya, and Prof. Yasuo Fukui. I learned a great deal from discussions, comments, and revisions in the process of writing the paper. It is thanks to all the co-authors that I could grow as a researcher. The SFUMATO code developed by Prof. Matsumoto was used to produce the important results of this research. I would also like to thank Japan Student Services Organization. I could spend my research life without financial hardship. The numerical computations were carried out on the XC50 system at the Center for Computational Astrophysics (CfCA) of the National Astronomical Observatory of Japan. This work is supported by Grants-in-aid from the Ministry of Education, Culture, Sports, Science, and Technology (MEXT) of Japan (JP22J15861).

I would like to thank Associate Prof. Hiroshi Kobayashi, Dr. Jiro Shimoda, Mr. Kensuke Kakiuchi, and all the other students who were members of my laboratory at Nagoya University. The guidance and discussions by the lab members had a great influence on shaping my image as a researcher. I would like to thank my colleague Ryunosuke Maeda, with whom I spent my doctoral course, and my junior students Kanta Kitajima and Ryushi Miyayama, who not only discussed our research but also took me out for drinks on our days off. It was thanks to them that I could engage in friendly competition and work hard on my research. I would also like to thank our secretaries, Kyoko Yamazaki, Natsu Kato, Ayako Imai, Ritsuko Watanabe, and Yasuko Iwata for their support.

I would also like to thank Kazunari Iwasaki, Kengo Tomida, Masato I.N. Kobayashi, and Kei K.E.I. Tanaka, and Yoshito Shimajiri, with whom I have had many discussions. Especially, I would like to thank Kazunari Iwasaki, who taught me a lot of things because our research themes are close, and Kengo To-

mida, who is one of the developers of the Athena++ code used in this study, with whom I often consulted on simulation issues. Yuri I. Fujii, Kenji Kurosaki, Shinsuke Takasaka, Doris Arzoumanian, Gabriel Rigon, Keisuke Sugiura, Ryosuke Tominaga, Hidekazu Isoya, Kodai Ito, Yuto Inayoshi, Hana Nishikawa, Yoshiaki Misugi, Yuta Nakanishi, Naoki Nishida, Hiroki Nakatsugawa, and I would like to thank all of my juniors who graduated in that master's course. It was thanks to them that I enjoyed our research discussions and laboratory life. I would also like to thank my friends Katsuka T. Abe, Suchetha Cooray, Hiroto Kondo, Hayato Fukunaga, Kiichi Yoshida, Sayaka Nagasaki, and Shuntaro Yoshida from other theory groups at Nagoya University, with whom we took classes together, competed with each other in master's thesis defense, and had fun daily life.

Prof. Ryo Yamazaki, Assistant Prof. Yutaka Ohira, and Shota Kisaka, who were my mentors at the Yamazaki Laboratory of Aoyama Gakuin University when I was an undergraduate student, recommend me to enter Nagoya University and supported my decision when I decided to study star formation. I learned a lot from their severe comments on my research at that time. In particular, Ryo Yamazaki was my first supervisor and the first researcher with whom I had discussions. His attitude of enjoying research influenced me, and it was then that I decided to become a researcher. I would like to thank my undergraduate classmates Takafumi Kobayashi, Natsuki Ishizaka, Shoma Kamijima, Masashi Komai, Shuto Sei, Shun Masumoto, Yuto Obara, and Shin Kakuchi. I was anxious about being in the laboratory environment for the first time, but thanks to them I could enjoy my research and life in the laboratory. I would like to thank my friends Keisuke Yamamoto, Yukimaru Saito, Saki Ikeda, and all my friends from high school for their encouragement.

Finally, I would like to express my gratitude to my family. My father, Kazuki, is a restaurant owner, and to improve the service at his restaurant, he became a wine and sake sommelier. I sometimes helped him at his restaurant before he became a sommelier, and he found time to study for his certification while working. He is a person to look up to because of his strong commitment to what he decides to do. I was encouraged by his attitude toward work. My mother, Yukari, supported me more than anyone else. When I told her that I wanted to become a researcher, she was a little apprehensive, but she believed in me and let me do what I wanted to do. My younger brother, Issa is studying to become a fashion designer. Becoming a fashion designer seems to be difficult, and he is taking on the challenge. I am encouraged by the way he is growing up. I would like to thank my grandparents and relatives. They have always watched my growth and supported me.

Contents

List of Figures

List of Tables

Chapter 1

Introduction

Star formation and evolution is a fundamental physical process in molecular clouds in galaxies. Furthermore, stars cause stellar winds and supernovae, which affect galaxy evolution and supply the gas that is the ingredient of stars (see Fig.). Since the evolution of a star is determined by its mass, the origin of the initial mass function is important, which implies that it is important to understand the star formation process. Therefore, understanding the star formation process is essential to understanding the universe as a whole. However, the initial conditions of the star formation process have not yet been unknown. In this thesis, we investigate the formation and evolution of dense filamentary molecular clouds, sites of star formation, to understand the initial condition of star formation.

1.1 Overview of Molecular Cloud

1.1.1 Molecular Clouds Formation

In galaxies, there is multi-phase gas such as hot ionized medium, warm/cold neutral medium, molecular clouds, and HII region. We focus on warm/cold neutral medium because the former transit to molecular clouds and the latter are sites of star formation. The warm neutral medium is neutral hydrogen atomic gas whose density and temperature of ~ 0.1 cm^{-3} and ~ 8000 K, respectively. Almost all of the volume of a galaxy is occupied by the warm neutral medium and the hot ionized medium. The cold neutral medium is also neutral hydrogen atomic gas whose density and temperature of ~ 1 cm^{-3} and ~ 100 K, respectively. These two components can coexist because pressure equilibrium with ~ 1000 K cm^{-3} is realized between the warm and cold neutral medium. Therefore the warm/cold neutral medium is stable for linear perturbation. The molecular clouds are mainly composed of molecular hydrogen and range in size from a few pc to 100 pc. The density and temperature are more than 10^2 cm^{-3} and ~ 10 K cm^{-3}, respectively, that is pressure is larger than the warm/cold medium due to self-gravity.

We introduce how dense gas formation such as the cold neutral medium and the molecular clouds from diffuse atomic gas is achieved. The cooling and heating processes are essential to understand dense gas formation. Koyama & Inutsuka (2000) shows important cooling and heating process in interstellar medium (Fig.

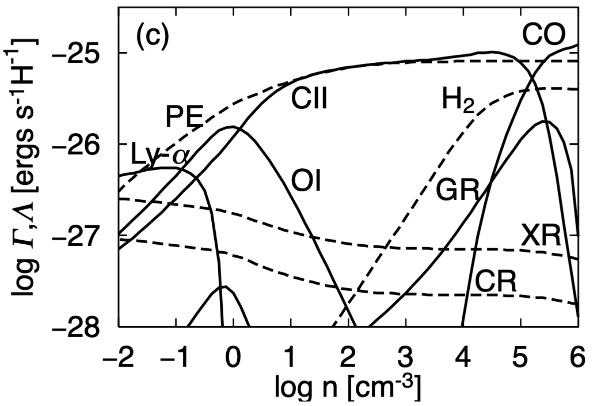

Figure 1.1: The dashed and solid lines show heating and cooling rates for unshielded gas per hydrogen nucleus at equilibrium, respectively. Heating processes are photoelectric from dust grains and PAHs (PE), X-ray (XR), cosmic ray (CR), and H_2 formation/destruction (H_2). Cooling processes are CII fine-structure (CII), OI fine structure (OI), hydrogen Lyα (Ly-α), CO rotation/vibration line (CO), and atomic and molecular collisions with dust grains (GR).

1.1). The dashed and solid lines show heating and cooling rates for unshielded gas per hydrogen nucleus at equilibrium, respectively. The heating mechanisms are the photoelectric emission from dust grains and PAHs (Polycyclic Aromatic Hydrocarbons), ionization by cosmic rays and soft X-rays, and the formation and photo-dissociation of H_2. The local far-ultraviolet (FUV) field is set to 1.7 times Habing's estimate (Wolfire et al., 1995). The dominant cooling processes are the line emission from H, C, O, Si, and Fe, by rotation/vibrational line from CO, as well as by atomic and molecular collisions with dust grains.

Adiabatic fluid is stable for an increment of density because of pressure enhancement. However, if there is a cooling process, it can be unstable. Field (1965) studies the stability conditions of a uniform medium about heating and cooling and shows that a phase transition (warm neutral medium becomes cold one) due to thermal instability occurs when the following conditions are satisfied

$$\left(\frac{\partial \mathcal{L}}{\partial T}\right)_{\mathrm{P}} < 0 \Leftrightarrow \left(\frac{\partial P}{\partial \rho}\right)_{\mathcal{L}} < 0 \tag{1.1}$$

where, $\mathcal{L} = \rho\Lambda - \Gamma$, $\rho\Lambda$ denote the cooling function per volume and Γ denotes the heating function. This instability occurs for temperatures between $\sim$ 100 and $\sim$ 5000K in the interstellar medium. In Figure 1.2, we show the dispersion relation for thermal instability Koyama & Inutsuka (2000). The dashed curve represents the dispersion relation for the case of the unperturbed state in equilibrium. (The solid curve is the dispersion relation for the case of an isobarically contracting unperturbed state[1].) Thermal conduction stabilizes the perturbations with smaller

---

[1] Their motivation to create this curve is that they consider thermal instability shocked layer. We will mention below the importance of shock compression

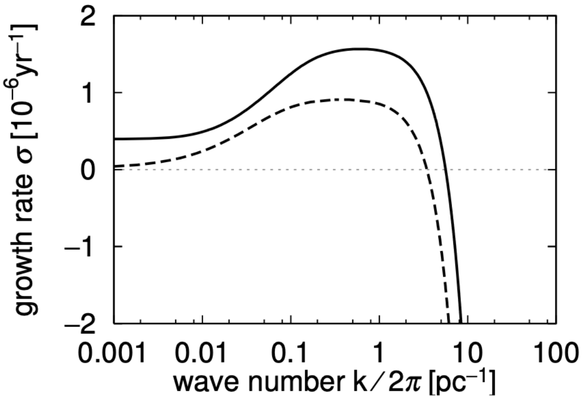

Figure 1.2: Dispersion relation for thermal instability. The dashed curve represents the dispersion relation for the case of the unperturbed state in equilibrium. The solid curve shows the dispersion relation for the case of an isobarically contracting unperturbed state.

wavelengths. The critical wavelength is

$$\lambda_{\rm c} = 2\pi \left\{ \frac{\rho}{K} \left[\frac{\partial \mathcal{L}}{\partial T} \right]_{\rm P} \right\}^{-1/2} \sim \sqrt{\frac{KT}{\rho^2 \Lambda}} \tag{1.2}$$

where K denotes the coefficient of thermal conduction. Cold neutral medium around this scale forms. The molecular cloud that eventually forms by this instability has a clumpy structure.

As we mentioned, the warm/cold neutral medium is stable for linear perturbation. Thus, a nonlinear trigger is necessary to create the cold neutral medium. One of the triggers is a shock wave. A shock wave is caused by gas collision, feedback from massive stars including supernovae and expanding HII regions, and encounters with galactic spiral shock. In Figure 1.3, we show the phase diagram and schematics of the evolution track for interstellar medium (Inoue & Inutsuka, 2009). Inoue & Inutsuka (2009) indicates that the direct formation of molecular clouds from a warm neutral medium is not a typical molecular cloud formation process unless the direction of shock wave propagation is biased to the orientation of the mean magnetic field. Thus, they emphasize the importance of multiple compression, as a typical formation process of molecular clouds.

1.1.2 Properties of Molecular Clouds and Star Formation

Isothermal Approximation

In molecular clouds, the dominant heating source is cosmic rays. Dominant cooling sources are CO rotation/vibration line emission and dust cooling at higher densities ($> 10^5$ cm^{-3}). The balance between them maintains a temperature of approximately 10 K (sound speed $c_{\rm s} = 0.2$ km s^{-1}). Using the cooling rate at the

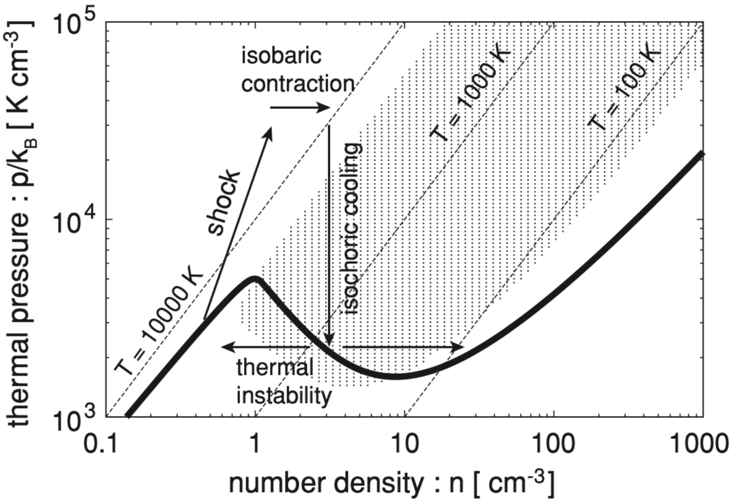

Figure 1.3: Phase diagram of the interstellar medium. The thick line shows the thermal equilibrium state. In the dotted region, gas is thermally unstable. Arrows represent schematical evolution tracks for gas.

thermal equilibrium of the molecular gas, the cooling time $t_{\rm cool}$ can be written as

$$t_{\rm cool} = \frac{k_{\rm B}T}{n\Lambda} \sim 10^4 \text{ yr}, \tag{1.3}$$

for $n = 100$ cm^{-3}. where $k_{\rm B}$ is Boltzmann constant. This timescale is smaller than the dynamical timescale of molecular clouds (see Figure 1.4). Therefore, the isothermal equation of state is justified in the molecular cloud.

MHD Approximation

The main component of molecular clouds is molecular hydrogen, i.e., uncharged particles, and there is a slightly ionized component (ionization degree of $\sim 10^{-7}$). However, these neutrals also interact indirectly with the magnetic field like charged particles, and as a result, the motion of the gas in the molecular cloud can be approximated to follow the ideal magneto-hydrodynamics (MHD) equation. The qualitative explanation is as follows. Electrons and protons have electric charges, and in the presence of a magnetic field, they are subject to the Lorentz force and orbit around the magnetic field lines. From a macroscopic point of view, a group of charged particles (plasma) couples with a magnetic field (magnetic frozen-in). On the other hand, neutral particles such as molecular hydrogen interact with charged particles via collisions. When plasma moves, the group of neutrals (neutral fluid) is dragged via collision with plasma. Since plasma couples with the magnetic field, The motion of neutral fluid, the magnetic field, and plasma couple. Therefore, molecular clouds behave just like a fully ionized plasma, and their motion can be described by the MHD equation.

We consider the specifics using the equations. The Lorentz force per unit

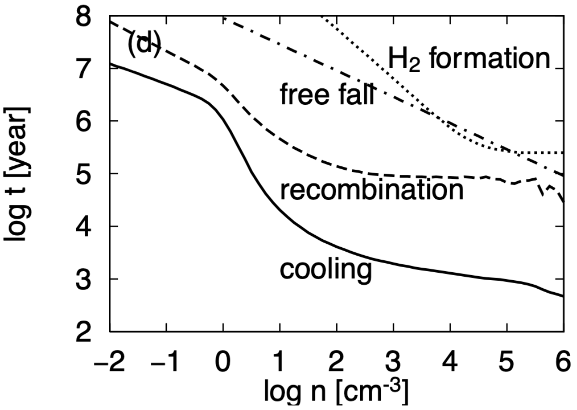

Figure 1.4: Various timescales, cooling time (solid line), recombination time (dashed line), free-fall time (dot-dashed line), and H2 formation time (dotted line).

volume is

$$\mathrm{f}_{\mathrm{L}} = \frac{1}{4\pi}(\nabla \times \mathbf{B}) \times \mathbf{B}, \tag{1.4}$$

where, **B** denotes magnetic field. The frictional force by ion fluid[2] on neutral fluid can be written as follows

$$\mathbf{f}_{\mathrm{d}} = \gamma_{\mathrm{in}}\rho_{\mathrm{n}}\rho_{\mathrm{i}}\left(\mathbf{u}_{\mathrm{i}} - \mathbf{u}_{\mathrm{n}}\right) \tag{1.5}$$

where, ρ_{n} and ρ_{i} denote the mass density for the neutral fluid and the ion fluid, respectively. When collision velocity between an ion and a neutral molecule is small, i.e., cold environment such as a molecular cloud, Osterbrock (1961) pointed out that Langevin cross section is correct for the cross-section between ions and neutrals, because the ion induces a dipole moment in the neutral molecule, effectively changing the collision cross-section. For the Langevin cross-section, since $\sigma_{\mathrm{in}} \propto w^{-1}$, γ_{in} becomes constant. Draine et al. (1983) computed the resulting value for $\gamma_{\mathrm{in}} = 3.5 \times 10^{13} \mathrm{cm}^3\mathrm{g}^{-1}\mathrm{s}^{-1}$. The interior of a molecular cloud is partially ionized by cosmic rays. If the ionization rate for a neutral particle is ζ, the ionization rate of the neutral particle per unit volume is ζn_{n}. On the other hand, the recombination rate of ions and electrons is proportional to the number density of both ions and electrons and is, therefore, proportional to $n_{\mathrm{i}}n_{\mathrm{e}} \propto n_{\mathrm{i}}^2$. Considering the steady state, the ionization and recombination are balanced and can be written using the mass density and the constant $C = 3 \times 10^{-16}\ \mathrm{cm}^{-3/2}\ \mathrm{g}^{1/2}$ as follows

$$\rho_{\mathrm{i}} = C\rho_{\mathrm{n}}^{1/2}. \tag{1.6}$$

Since the gas in the molecular cloud is dense enough to collide between gas particles, the Lorentz force and the frictional force are dominant over the other forces

---

[2] Ions, which are the most massive of the charged particles, are responsible for momentum exchange in collisions with neutral particles. Electrons have less mass than ions, so they contribute little to the momentum exchange. electrons do not contribute much to momentum exchange because they have less mass than ions.

(gravity and pressure gradient forces) and their sum is nearly zero. Therefore, considering $\mathbf{f}_{\rm L} = \mathbf{f}_{\rm d}$, the ion-neutral drift velocity is

$$\mathbf{v}_{\rm d} \equiv \mathbf{u}_{\rm i} - \mathbf{u}_{\rm n} = \frac{1}{4\pi\gamma\rho_{\rm n}\rho_{\rm i}}(\nabla \times \mathbf{B}) \times \mathbf{B} \tag{1.7}$$

To evaluate the drift velocity, we estimate the order of Eq. 1.7,

$$v_{\rm d} \sim \frac{B^2}{4\pi\gamma\rho_{\rm n}\rho_{\rm i}L} \approx \frac{v_{\rm A}^2}{V}, \tag{1.8}$$

where, $V \equiv \gamma\rho_{\rm i}L = \gamma CL\rho^{1/2}$. $v_{\rm A} \equiv B/\sqrt{4\pi\rho}$ denotes Alfvén velocity. We assume $\rho = \rho_{\rm n} + \rho_{\rm i} \approx \rho_{\rm n}$. When $L = 1$ pc, $n_{\rm n} = 100$ cm^{-3}, and $B = 10$ μG, then $V = 19$ km s^{-1} and $v_{\rm A} = 1.4$ km s^{-1}. Therefore, $v_{\rm d} \sim 0.1$ km s^{-1} $\ll v_{\rm A}$ is satisfied, indicating that the difference in motion between plasma and neutral fluid is small and the MHD approximation is justified. Note that we cannot neglect the effect of the slip of the magnetic field at the small scale.

Supersonic Turbulence

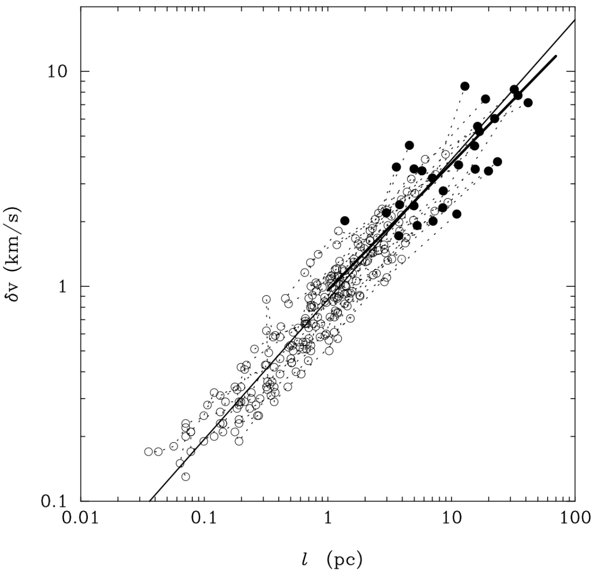

Figure 1.5: Observational data for velocity dispersion δv v.s. size of molecular clouds l (Heyer & Brunt, 2004).

One of the important features given by observation of ^{12}CO J=1-0 is the line width which is larger than the expected line width by the sound speed of gas, indicating that molecular clouds are super-sonically turbulent. In Figure 1.5, we show observational data for velocity dispersion δv v.s. size of molecular clouds l (Heyer & Brunt, 2004). There is typical relation of $\delta v \propto l^{0.5}$ (Larson, 1981). The super-sonic turbulence creates density inhomogeneity with a power spectrum of $(\log\rho)^2_{\rm k} \propto k^{-4}$ (Beresnyak et al., 2005; Elmegreen & Scalo, 2004; Scalo & Elmegreen, 2004).

Shock Wave

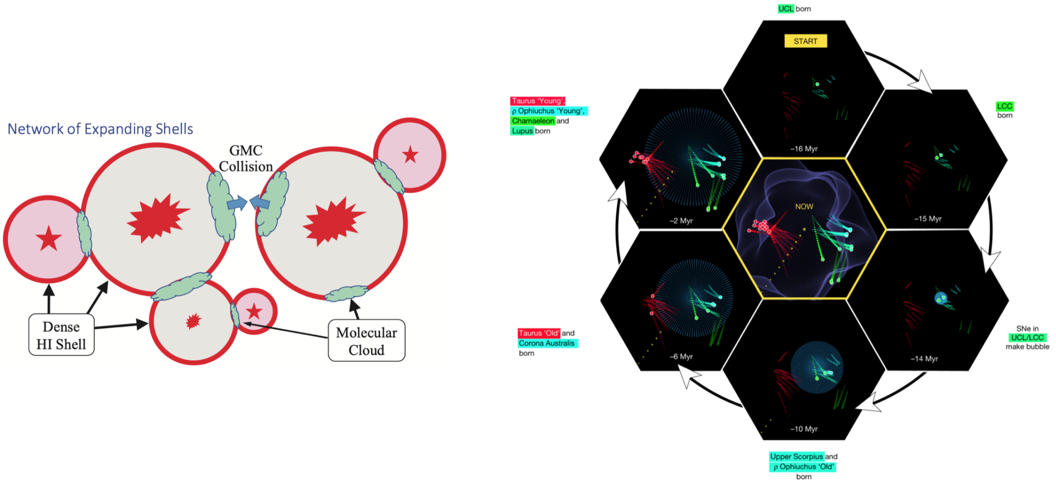

Figure 1.6: *Left panel*: A schematic illustration of multiple compression scenario of interstellar medium (Inutsuka et al., 2015) The thick red unfilled circles correspond to the dense multi-phase interstellar medium. *Right panel*: The evolution of the Local Bubble and sequential star formation at the surface of its expanding shell. The central panel shows the present day. Colored paths represent star cluster trace-backs. Before the cluster birth, the trace-backs are shown as unfilled circles, but after the birth, they are shown as filled ones. The purple sphere represents a model for the evolution of the Local Bubble. The yellow trace-backs show solar orbit (Zucker et al., 2022).

We should emphasize that shock wave is important for the dynamics of molecular clouds. As mentioned in §1.1.1, propagation of shock waves is ubiquitous in galaxies. Using supernovae as an example, we can estimate the time scale of shock wave sweeping for whole gas in a galactic disk,

$$t_{\rm swept} \sim \frac{V_{\rm galaxy}^{1/3}}{v_{\rm SN} N_{\rm SN}^{1/3}} \simeq 1 \ {\rm Myr} \tag{1.9}$$

where, $V_{\rm galaxy} \sim (10 \ {\rm kpc})^2 \times 100 \ {\rm pc}, v_{\rm SN} \sim 100 \ {\rm km \ s^{-1}}$, and $N_{\rm SN} \sim 10^6 \ {\rm yr}/100 \ {\rm yr}$ denote the volume of galactic disk, typical shock velocity of supernovae, and the number of supernovae of age one million year, respectively. We assume supernova explosions occur once 100 yr in a galaxy. Therefore, molecular clouds are shock compressed once per million year.

Inutsuka et al. (2015) found the resultant star formation efficiency $\epsilon_{\rm SF} \sim 10^{-2}$ within a cloud, which is consistent with observation (Zuckerman & Evans, 1974), based on the episodes of multiple supersonic compression. Zucker et al. (2022) reported an analysis of the 3D positions, shapes, and motions of dense gas and young stars within 200 pc of the Sun from *Gaia* data. They found that the most star-forming regions lie on the surface of the shock front of multiple supernovae (Local Bubble) and that their young stars show outward expansion mainly perpendicular to the bubble's surface (see Figure 1.6). These findings support the scenario that the expansion of the Local Bubble swept up the interstellar medium and drives star formation, in turn providing robust observational support for the theory of supernova-driven star formation (Inutsuka et al., 2015). When molecular clouds are shock-compressed, further dense structure formation occurs. This topic is our main target, details are shown in §1.2.

Self-gravitational Collapse in Molecular Clouds

Within the high-density region of a molecular cloud, a particularly dense region that is the parent body of a star is called a molecular cloud core. When the molecular cloud core gravitationally contracts, it evolves into a denser object, and eventually, hydrogen-burning reactions begin. The central body is then pressurized by the nuclear reaction energy, the gas sphere stops contracting and the radius of the central body remains constant. The central body at this stage is in the main sequence and can be said to have given birth to a star.

1.2 Filamentaly Molecular Clouds

Stars are formed in dense regions in molecular clouds (e.g., Lada et al., 2010; Enoch et al., 2007; André et al., 2014; Hennebelle & Inutsuka, 2019). Recent dust thermal emission observations by the *Herschel* space telescope (band: 70 μm–500 μm) revealed that dense filamentary structures are ubiquitous in nearby molecular clouds (e.g., André et al., 2010; Arzoumanian et al., 2011). Additionally, star-forming cores and young stellar objects are embedded along the filaments, which indicates their crucial role in star formation (Könyves et al., 2015). Therefore, comprehension of the formation and evolution mechanisms is significant to understand the star formation scenario and the initial condition of star formation.

1.2.1 Definitions

To understand the stability of filament, let us consider a uniform, infinitely elongated, axisymmetric, and cylindrical gas. The Poisson equation for self-gravity is

$$\nabla^2\phi = \frac{1}{r}\frac{d}{dr}r\frac{d\phi}{dr} = 4\pi G\rho, \tag{1.10}$$

where, ϕ, G is gravitational potential and constant, respectively. To get the gravitational force, multiplying r and integrate from $r = 0$ to outer edge of cylinder $r = R$,

$$R\left.\frac{d\phi}{dr}\right|_{r=R} = 2G\int_0^R 2\pi r\rho dr = 2GM_{\rm line}, \tag{1.11}$$

and,

$$F_{\rm g} = \left.\frac{d\phi}{dr}\right|_{r=R} = \frac{2GM_{\rm line}}{R} =\propto R^{-1}, \tag{1.12}$$

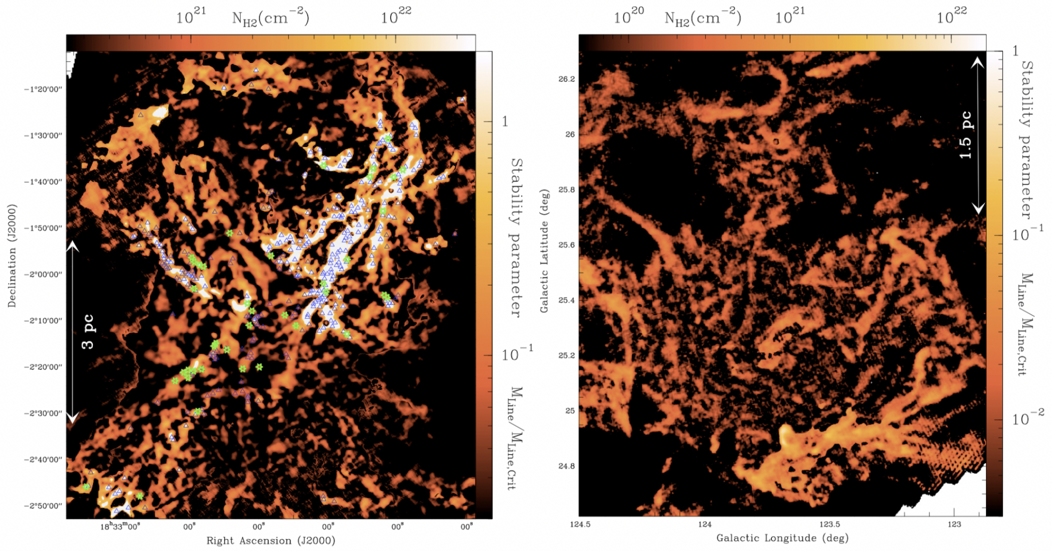

Figure 1.7: Column density (line-mass) map of molecular hydrogen in Aquila(left)/Polaris(right) molecular cloud given by *Herschel* telescope. The column density of molecular hydrogen is estimated from the intensity map of dust thermal emission. (The density of the molecular hydrogen column density can be estimated by considering that the more dust there is, the more molecular hydrogen is also present.) The color bar on the right of each figure indicates the line-mass normalized by the critical line-mass (Eq. 1.16), which is gravitationally unstable when it exceeds unity. The line-mass map is given by a typical filament width of 0.1 pc (see §1.2.4), and the column density can be compiled as the line-mass. The green stars and blue triangles in the left panel are candidates for Class 0 protostars and bound prestellar cores identified by Könyves et al. (2010) and Bontemps et al. (2010). While the line-mass is supercritical, i.e., the region of gravitational instability coincides with the region where the protostar/bound core is located, the right figure suggests that the filament is gravitationally stable and no star formation is currently taking place.

where, $M_{\rm line} \equiv \int_0^R 2\pi r \rho dr$ is mass per unit length (Line-mass). On the other hand, pressure gradient force is

$$F_{\rm p} = \rho^{-1} \left.\frac{\partial p}{\partial r}\right|_{r=R} \propto R^{-2\gamma_{\rm eff}+1}, \tag{1.13}$$

where, $p = K\rho^{\gamma_{\rm eff}}$ is pressure, $\gamma_{\rm eff}$ is effective specific ratio. The ratio of Eq. 1.12 and Eq. 1.13 is

$$\frac{F_{\rm p}}{F_{\rm g}} = R^{2(1-\gamma_{\rm eff})}. \tag{1.14}$$

For the isothermal cylindrical system ($\gamma_{\rm eff} = 1$), it is possible to become dynamical equilibrium when a filament has the critical line-mass. The hydro-static equilibrium distribution is given by

$$\rho_{\rm eq}(r) = \rho_c \left[1 + \left(\frac{r}{H_0}\right)^2\right]^{-2}, \tag{1.15}$$

where, ρ_c and $H_0 \equiv \sqrt{\frac{2c_\mathrm{s}^2}{\pi G \rho_\mathrm{c}}}$ are central density and scale-height. To create stars in filaments, their line-masses have to exceed the critical line-mass $M_\mathrm{line,cr}$ for gravitational instability,

$$M_\mathrm{line,cr,th} = \int_0^\infty 2\pi\rho_\mathrm{eq}(r) r dr = 2c_\mathrm{s}^2/G \simeq 17\ \mathrm{M}_\odot\ \mathrm{pc}^{-1}, \tag{1.16}$$

where, $c_\mathrm{s} \simeq 0.2$ km s^{-1} is the isothermal sound speed of typical molecular clouds (e.g., Stodólkiewicz, 1963; Ostriker, 1964; Inutsuka & Miyama, 1992a; Inutsuka & Miyama, 1997). Non-thermal velocity dispersion Δv, i.e., turbulence, makes the critical line-mass increase. Eq. 1.16 can be written as

$$M_\mathrm{line,cr,tot} = 2\left(c_\mathrm{s}^2 + \Delta v^2\right)/G \simeq 17 + 425\left(\frac{\Delta v}{1\ \mathrm{km\ s}^{-1}}\right)^2\ \mathrm{M}_\odot\ \mathrm{pc}^{-1}. \tag{1.17}$$

The magnetic field also makes the critical line-mass amplify. It is known that star-forming filaments are threaded by magnetic field perpendicularly (see details in §1.2.4). Tomisaka (2014) gave the formula of line-mass including the effect of the magnetic field is

$$M_\mathrm{line,cr,B} \simeq 2.2\left(\frac{w}{0.1\mathrm{pc}}\right)\left(\frac{B}{10\mu\mathrm{G}}\right) M_\odot \mathrm{pc}^{-1} + 13.9\left(\frac{c_s}{0.19\ \mathrm{km\ s}^{-1}}\right)^2 M_\odot \mathrm{pc}^{-1}, \tag{1.18}$$

where, w and B are the widths of a filament and magnetic field strength.

The column density profiles are parameterized by Plummer function,

$$N(x) = A_\mathrm{p}\frac{n_0 R_\mathrm{flat}}{\left(1 + (x/R_\mathrm{flat})^2\right)^{(p-1)/2}}, \tag{1.19}$$

where, A_p and x are constant and projected distance from filament's axis. $R_\mathrm{flat} \equiv N(0)/(n_0 A_\mathrm{p})$. The equilibrium filament width i.e., full-width-half-maximum of the Plummer function is given by

$$w_\mathrm{eq} = 2R_\mathrm{flat}\left(2^{2/(p-1)} - 1\right)^{1/2}. \tag{1.20}$$

For $p = 4$, Eq. 1.19 corresponds isothermal case, corresponding 3D profile is Eq. 1.15, $A_\mathrm{p} = \pi/2$, $R_\mathrm{flat} = H_0$, and $w_\mathrm{eq} \simeq 1.53 R_\mathrm{flat}$.

1.2.2 Formation

Previous theoretical research on filament formation proposed several types of mechanisms. We summarize the filament formation mechanism in the following, Figure 1.8, table 1.1.

Type G

The first one is a well-known self-gravitational fragmentation of a sheetlike cloud (Tomisaka & Ikeuchi, 1983; Miyama et al., 1987a,b; Nagai et al., 1998; Kitsionas & Whitworth, 2007; Balfour et al., 2015, 2017), which is created when molecular clouds

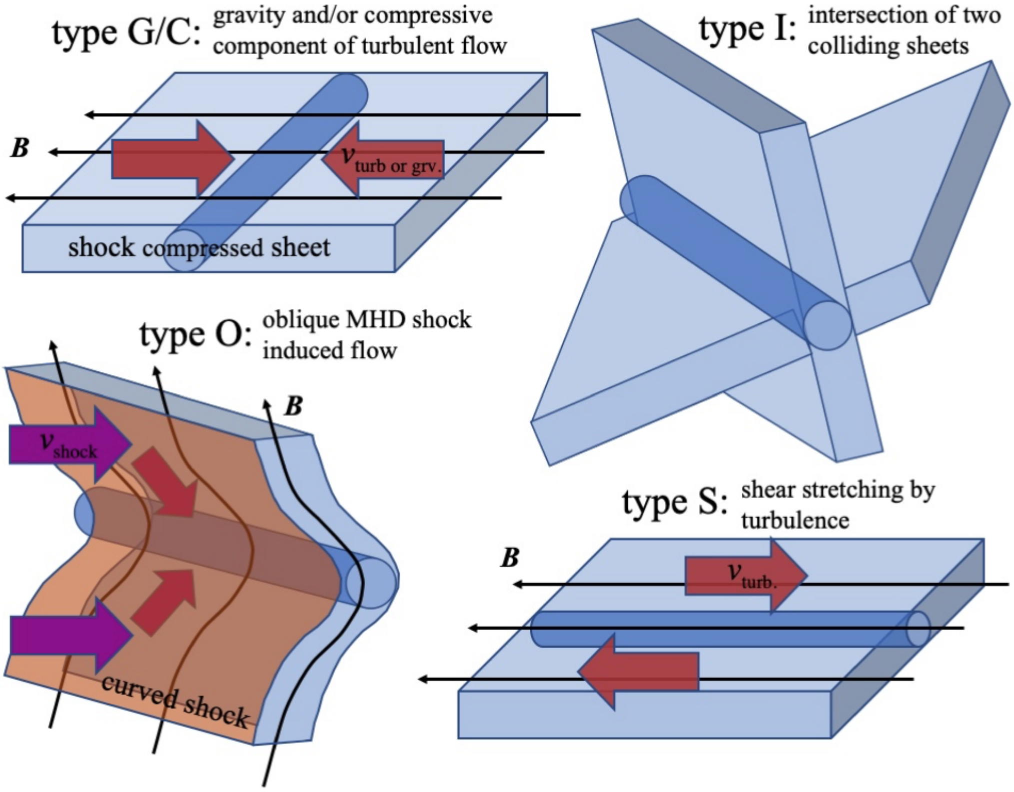

Figure 1.8: Schematic illustrations of filament formation mechanisms (Abe et al., 2021; Pineda et al., 2022). See also table 1.1

are shock-compressed. In this paper, we call this type of filament formation type G formation. According to linear stability analysis conducted by Nagai et al. (1998), gravitational instability creates filaments with line-masses larger than but comparable to the critical line-mass when the width of the sheet is comparable to the Jeans length (i.e., the self-gravity is important in the dynamics).

Type I

Padoan & Nordlund (1999), Pudritz & Kevlahan (2013), Matsumoto et al. (2015), and, Federrath (2016) showed filament formation induced by turbulence in molecular clouds by using three-dimensional magnetohydrodynamic (MHD) simulation. Padoan & Nordlund (1999) reported that the turbulent velocity given in an initially uniform molecular gas induces the formation of shock-compressed sheets, and then the interaction of two sheets creates a filament at the intersection of them. We call this mechanism type I filament formation. It should be noted that the type I process occurs in the super-Alfvénic case, in which the initial Alfvénic Mach number $\mathcal{M}_{\text{A,i}} \gtrsim 10$.

Type O

Inoue & Fukui (2013), Vaidya et al. (2013), Inutsuka et al. (2015), and Inoue et al. (2018) reported that the filaments are generated when a shock wave sweeps a cloud containing density inhomogeneity or clumps. In this case, a dense blob embedded in a magnetized molecular cloud is transformed into a dense filament in the shock-compressed layer owing to the effect of an oblique (or curved) MHD shock wave. Throughout this study, this filament formation mode is called type O mode. It should be noted that the effects of thermal instability and turbulence cause molecular clouds to be highly clumpy by nature (e.g., Inoue & Inutsuka, 2012a). Note that in most theoretical works that study structure formation in molecular clouds by turbulence, a uniform-density gas is used as an initial condition. Therefore the type O mode is missing in the studies that assume the uniform initial density. As we show subsequently, the type O mode dominates over other modes when the shock Mach number is high.

Type C

Chen & Ostriker (2014) and Chen (2015) showed another filament formation behind shock waves that is different from type O. They found that filaments are formed by converging gas flow components along the local magnetic field in the case the substantial turbulent motions are given in the initial condition. We call this mode type C filament creation mechanism. This mechanism creates the filaments that are perpendicular to the background magnetic field when the turbulence is sub-Alfvénic (Chen & Ostriker, 2014; Chen, 2015; Planck Collaboration XXXV, 2016). This is because the component of turbulent velocity perpendicular to the magnetic field is suppressed by magnetic tension force, and only motion parallel to the magnetic field can compress the gas. Padoan & Nordlund (1999) also reported the type C process in the trans-Alfvénic case ($\mathcal{M}_{\mathrm{A,i}} \sim 1$).

Type S

Hennebelle (2013) reported that a small clump in a turbulent molecular cloud is stretched by turbulent shear flows and evolves into a small line-mass filament parallel to the magnetic field (see also Inoue & Inutsuka, 2016, for the origin of HI filament/fiber). We call this mode type S mechanism, and this type S creates filaments that are parallel to the magnetic field lines in contrast to the other types that create filaments perpendicular to the magnetic field lines. Xu et al. (2019) showed that the anisotropic nature of turbulent MHD eddies results in filamentary structure formation parallel to a magnetic field.

1.2.3 Evolution

Accretion

Gas accretion onto filaments is a crucial process to determine the evolution and physical properties such as line-mass and width of filaments. Klessen & Hen-

Table 1.1: Filament formation mechanisms.

Category	Filament vs. Magnetic field	A brief description of the formation mechanism
type G	perpendicular	self-gravitational fragmentation of a sheetlike cloud
type I	-	the intersection of two shocked layers
type O	perpendicular	the effect of an oblique MHD shock wave
type C	perpendicular	converging gas flow components along the magnetic field in the post-shock layer
type S	parallel	stretching by turbulent shear flows, small line-mass

nebelle (2010) argued that turbulence is generated by the accretion in a general sense and that turbulence affects evolution. As mentioned in §1.2.2, the formation mechanisms of high-density filaments, which are important for star formation, are mainly Type G, C, and O. The common feature of these mechanisms is that filaments are formed by gas flowing perpendicular to the long axis of the filament (along the magnetic field) in a shocked-compressed sheet. Line observations also show the evidence of the perpendicular accretion onto filaments (Palmeirim et al., 2013; Shimajiri et al., 2019; Chen et al., 2020). Especially, Shimajiri et al. (2019) claimed that the accretion onto filaments in the shocked sheet. The accretion rate $\dot{M}_{\rm line}$ is estimated to range from a few 10 to a few 100 $M_\odot$ Myr^{-1} pc^{-1} (Palmeirim et al., 2013; Bonne et al., 2020). The accretion timescale can be written as

$$t_{\rm acc} = \frac{M_{\rm line}}{\dot{M}_{\rm line}}, \tag{1.21}$$

which is the order of ~ 0.1 Myr.

Shock wave with the Alfvén Mach number $\mathcal{M}_{\rm A} < 1$ and sonic Mach number $\mathcal{M}_{\rm s} > 1$ is called "slow (mode) shock." Given that the massive filaments are formed in the post-shock layer threaded by the strong magnetic field, the surface of the filament is naturally bound by the slow shocks. Lessen & Deshpande (1967) found through linear stability analysis that the slow shock front is corrugationally unstable (slow shock instability, hereafter SSI). The mechanism of SSI is as follows. For the slow shock, in contrast to the fast shock, the component of the magnetic field tangential to the shock surface decrease across the front. Thus, when the shock corrugates, magnetic field lines kink as red lines shown in Figure 1.9. Because gas flows along the magnetic field, the gas converges behind the peak of the shock, while it diverges behind the valley. Such flow patterns increase (decrease) the pressure behind the peaks (valleys), which further push up (pull down) the shock front unstably. Édel'Man (1989) showed that the approximated dispersion relation of SSI for $\mathcal{M}_{\rm A} \ll 1$ can be written as

$$\omega \sim -i\frac{\gamma - 1}{\gamma + 1} M_{\rm A}^2 v_{\rm sh} k, \tag{1.22}$$

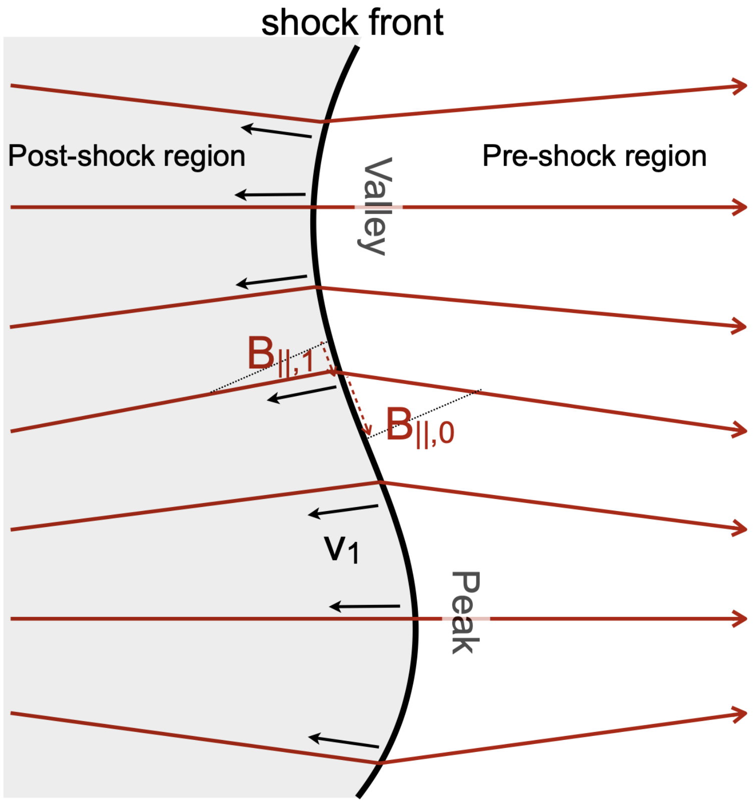

Figure 1.9: Schematic illustration of two-dimensional slow mode shock.

where, ω, $v_{\rm sh}$, and k are frequency, shock velocity, and wave number of the shock corrugation. As an more accurate solution, Édel'Man (1989) derived the approximate dispersion relation for $\gamma = 5/3$:

$$\omega \simeq -i\left(0.208M_{\rm A}^2 - 0.0775M_{\rm A}^4 + 0.06M_{\rm A}^6\right)v_{\rm sh}k. \tag{1.23}$$

Eqs. (1.22) and (1.23) show that the most unstable scale is infinitesimally small. This unphysical feature stems from ideal approximation and resulting discontinuous treatment of the shock. To know the physical scale length of the SSI, we have to take a non-ideal effect into account.

Fragmentation

Understanding the fragmentation of filaments is important since fragmentation results in core formation. Linear analysis by Stodólkiewicz (1963); Inutsuka & Miyama (1992b) shows the most unstable wavelength for self-gravitational fragmentation of filaments $\lambda_{\rm max}$,

$$\lambda_{\rm max} \sim 4 \times w_{\rm eq}. \tag{1.24}$$

The distance collects gas is typically four times its width when a filament fragments. Thus, (sub-) critical filaments will form equally spaced cores. The e-folding time for most unstable mode ($\lambda = \lambda_{\rm max}$) is

$$t_{\rm frag} = \frac{3}{2\sqrt{\pi G \rho_0}} = 1.66 \left(\frac{n_0}{10^3\ {\rm cm}^{-3}} \right)^{-1/2} {\rm Myr}. \tag{1.25}$$

However, the actual spacing of cores given by observations is not consistent with theories. The spacing is irregular or shorter than $\lambda_{\rm max}$ or scattered. This complexity might come from the accretion onto filaments considering the accretion timescale $t_{\rm acc}$ and the fragmentation timescale $t_{\rm frag}$ can be comparable. Clarke et al. (2016) performed numerical simulations and showed that accretion affects the dispersion relation for gravitational fragmentation. Chira et al. (2018) emphasized the importance of turbulence and density enhancements during the formation of filaments.

1.2.4 Properties

Line Mass

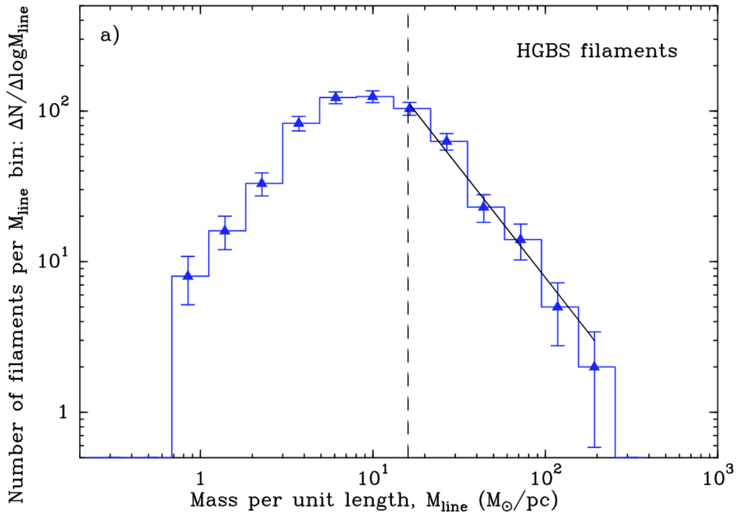

Figure 1.10: Crest-averaged line-mass histogram given by HGBS (André et al., 2019; Arzoumanian et al., 2019). Solid and dotted lines represent a Salpeter-like power law $\Delta N/\Delta \log M_{\rm line} \propto M_{\rm line}^{-1.6\pm0.1}$ and the critical line-mass (Eq. 1.16).

In Figure 1.10, we show line-mass histogram (Filament line-mass function; FLMF) given by *Herschel* Gould Belt Survey (HGBS) data (André et al., 2019; Arzoumanian et al., 2019). Solid and dotted lines represent a Salpeter-like power law $\Delta N/\Delta \log M_{\rm line} \propto M_{\rm line}^{-1.6\pm0.1}$ and the critical line-mass (Eq. 1.16). Figure 1.10 show typical line-mass range of 5–17 $M_\odot$ pc^{-1}. Both super-critical and sub-critical filaments exist, and stars form in at least thermally super-critical ($M_{\rm line}$ $M_{\rm line,cr,th}$) ones. The high line-mass region ($M_{\rm line} \gtrsim 17\ M_\odot$ pc^{-1}) is consistent with a Salpeter-like power, thus also consistent with initial mass function (IMF) and (CMF), in this sense, it is interesting considering the link among FLMF, IMF, and CMF.

However, there have been no explanations. In Chapter 2, we give hints to solve the origin of FLMF.

Infrared Dark Clouds (IRDCs) are the sites for massive mass star formation typically located at distances of a few kpc and have also high line-mass ($\gtrsim$ 100 $M_\odot$ pc^{-1}) filamentary structures (e.g., Peretto et al., 2014; Henshaw et al., 2014). Fukui et al. (2019); Tokuda et al. (2019) show that massive filaments of $\gtrsim$ 100 $M_\odot$ pc^{-1} exist in the Magellanic Clouds using ALMA observations.

Length Scale

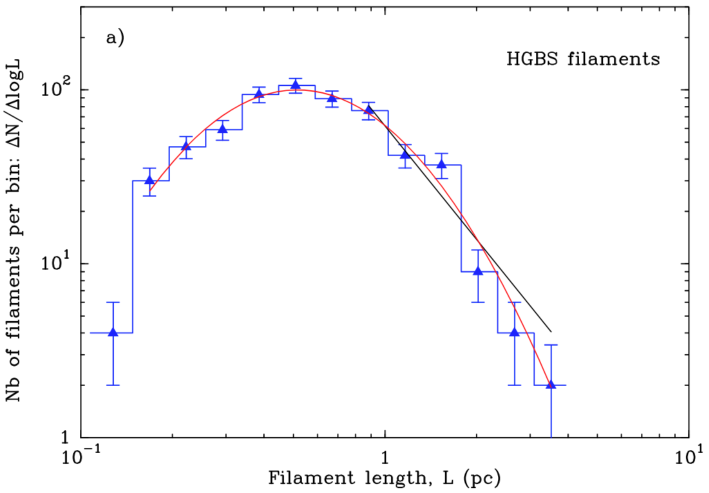

Figure 1.11:

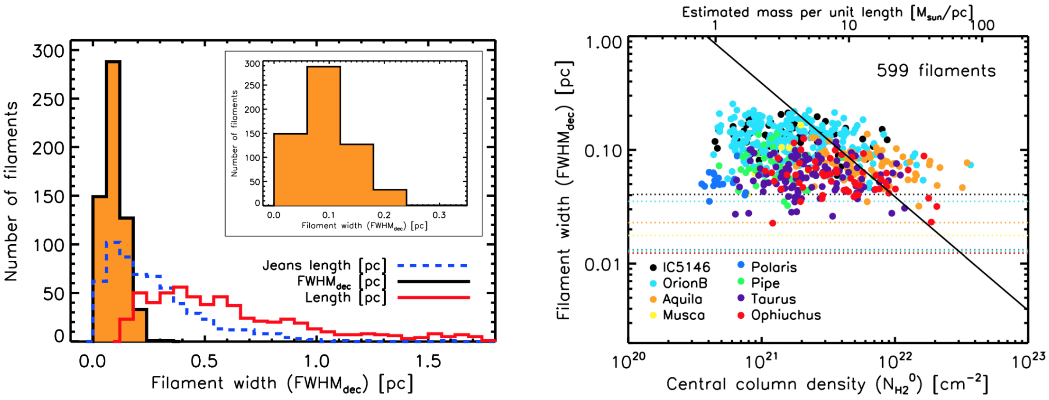

Figure 1.12:

Arzoumanian et al. (2018); André et al. (2019) revealed that *Herschel* Gould Belt filaments have typically 0.5 pc length. In the left panel of Figure 1.12, we show the histogram of 599 filaments' width. The mean value is 0.1 pc with a spread by a factor of 2. Similar results are given by $C^{18}O$ line emission observations (Orkisz et al., 2019; Suri et al., 2019). The widths given by using a denser tracer tend to be smaller than 0.1 pc, but these observations reflect the internal sub-structure in filaments. It is noted that the dynamic range of the dust emission is wider than the line emission, therefore the dust observations provide the real filament's width. In the right panel of Figure 1.12, we show the relation between column density (line-mass) and the widths of filaments in nearby clouds. The remarkable point is that the widths of filaments are 0.1 pc regardless of their line-mass, and are inconsistent with the Jeans length. The width of massive filaments should depend on column density (line-mass) due to the strong self-gravity and should be smaller than 0.1 pc. All theoretical models and simulations could have not explained the observational fact (Fischera & Martin, 2012; Federrath, 2016; Ntormousi & Hennebelle, 2019). Fischera & Martin (2012) considered the external pressure and calculated the dynamical equilibrium of a filament. They concluded that sub-critical filaments have a width of 0.1 pc. However, they did not explain the maintaining mechanism of the width of super-critical filaments. This contradiction between the theories and the observational fact is one of the open questions in the star formation domain remaining about 10 years. In this thesis, we call this problem "0.1 pc problem," and discuss it in Chapter 4.

Radial Profile

The radial profile of filaments provides information about their stability, equation of state, and environments. As mentioned in §1.2, the index of $p = 4$ corresponds to the isothermal case. However, most filaments show $p = 1.5$–2.5 (Arzoumanian et al., 2011; Palmeirim et al., 2013), indicating that the isothermal equilibrium cannot explain the feature of the observed filaments. Tomisaka (2014); Kashiwagi & Tomisaka (2021) calculated the equilibrium solution of a filament laterally threaded by the magnetic field and showed the index $2.48 \lesssim p \lesssim 2.73$. Pressure-confined filaments also have flatter profile $p < 4$ (Fischera & Martin, 2012).

Magnetic Field

Observation of polarized dust emission or stellar polarization indicated that the direction of the magnetic field is perpendicular to the long axis of the high column density filaments (Palmeirim et al., 2013; Planck Collaboration XXXV, 2016; Soler & Hennebelle, 2017). For low column density filaments ($N \lesssim 10^{21-22}$ cm^{-2}), on the other hand, the long axis of filaments tends to orient parallel to the magnetic field. These facts can be interpreted considering the mechanism of filament formation (see §1.2.2).

Davis-Chandrasekhar-Fermi method and the Zeeman observations derive plane-of-sky and line-of-sight magnetic field strength (Davis, 1951; Chandrasekhar & Fermi, 1953; Crutcher, 2012). The typical magnetic field strength is 70 μG for nearby filaments and 45 – 500 μG for IRDC. Note that the observations of the magnetic field strength have limitations or uncertainty.

Turbulence

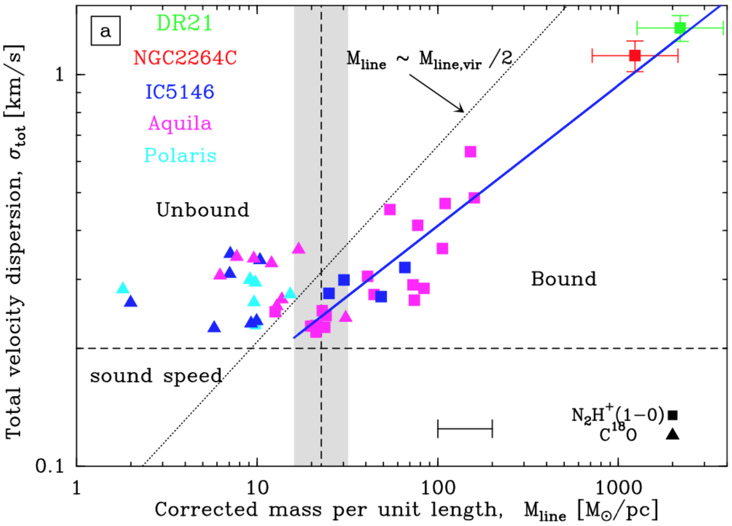

Figure 1.13: Total velocity dispersion v.s. line-mass. Blue points represent IC5146, magenta for Aquila, cyan for Polaris, red for NGC2264C, and green for DR21 filaments. The squares and triangles are velocity dispersion measured from N_2H^+ and $C^{18}O$ spectra, respectively. The grey shade shows the theoretical position of the critical line-mass (Eq. 1.16) for temperatures in the range T = 10–20 K. The dotted is $M_{\rm line} = M_{\rm line,vir}/2 = 2\sigma_{\rm tot}^2/G/2$, which corresponds to the boundary between gravitationally unbound and bound filaments. The blue solid line shows the best power-law fitting line for the gravitationally bound filaments. The best-fit $\sigma_{\rm tot} \equiv \sqrt{c_s^2 + \Delta v^2} \propto M_{\rm line}^{0.36} \pm 0.07$ does not change a lot (0.31 ± 0.08) when the fitting is performed without DR21 and NGC2264C filaments.

The gas velocity dispersions in filaments are measured by line observations. Arzoumanian et al. (2013) shows that the velocity dispersion in filaments close to sound speed and finds the relation between total velocity dispersion and line-mass such as $\sigma_{\rm tot} \propto M_{\rm line}^{0.36} \pm 0.07$, where $\sigma_{\rm tot} \equiv \sqrt{c_s^2 + \Delta v^2}$ (Figure 1.13).

Simulations show that turbulence within a filament is driven by gas accretion from the outside of the filament (Seifried & Walch, 2015; Clarke et al., 2017; Heigl et al., 2018). However, Heigl et al. (2020) indicated that turbulence does not contribute to the stability of filaments because the profile of turbulent ram pressure is flat. Furthermore, it is known that turbulence kinetic energy results in a only few percent of the kinetic energy of the accretion flow (Klessen & Hennebelle, 2010). The resulting velocity dispersion is trans-sonic to supersonic (Seifried & Walch, 2015; Clarke et al., 2017; Heigl et al., 2018, 2020)], which agrees with observations (Arzoumanian et al., 2013). Therefore, the statement in previous works is that gas accretion has nothing to stabilize the radial collapse of filaments.

1.3 Purpose of This Thesis

This study aims to understand the initial conditions of the star formation process. We investigate the formation and evolution of filamentary molecular clouds. Previous theoretical research on filament formation proposed many types of mechanisms as shown in §1.2.2. However, it is still unclear which type is responsible for the creation of star-forming filaments. Most of the proposed mechanisms (type I, O, C, and possibly type G) are triggered by shock compression. Thus, in this study, we perform a series of isothermal MHD simulations of filament formation by shock waves, focusing on the influences of shock strength, turbulence, and self-gravity on the filament formation mechanism. Note here that, since type I is effective only in highly super-Alfvénic turbulence, we hardly observe it in the results of our simulations that are performed under a realistic 10 μG initial magnetic field.

Previous studies have demonstrated that strong MHD shock compression allows for the formation of massive cores (Inoue & Fukui, 2013; Inoue et al., 2018; Sakre et al., 2021). However, these studies implicitly assumed a long duration of a shock wave (corresponding to collisions between large clouds), whereas the realistic duration of a shock wave depends on the situation, e.g., the shock created by cloud collision cannot be kept over a crossing time. On the other hand, simulations of unmagnetized cloud collisions by Takahira et al. (2014) demonstrated that gravitationally bound cores do not form in the case of short duration. Therefore, a systematic study into the effect of shock duration on the resulting filament/core formation is required. Furthermore, Enokiya et al. (2021) demonstrated that the peak column density of a star-forming region correlates with the number of OB stars in the system, and massive star clusters with more than 10 OB-type stars are associated with massive clouds whose peak column density exceeds 10^{23} cm^{-2}. Thus, the physical origin of the threshold peak column density of 10^{23} cm^{-2} must be clarified. In Chapter 3, we show the effect of shock wave duration on star formation.

As shown in §1.2.4, the width of filaments is one of the significant quantities to determine the initial condition for star formation. In linear theory, the self-gravitational fragmentation length scale of the filament depends on the width (Stodólkiewicz, 1963; Inutsuka & Miyama, 1992a). Arzoumanian et al. (2018) revealed that *Herschel* Gould Belt filaments have characteristic width of 0.1 pc. Similar results are given by C^{18}O line emission observations (Orkisz et al., 2019; Suri et al., 2019). Remarkably, the filaments keep their width regardless of their line-mass even beyond 100 $M_{\odot}$ pc^{-1}. If we only consider thermal support against gravity, such a high line-mass structure cannot keep 0.1 pc. Many authors studied the effects of turbulence and/or magnetic field and have shown that sub-critical and mildly super-critical filaments have a width of 0.1 pc (Fischera & Martin, 2012; Auddy et al., 2016; Priestley & Whitworth, 2022; Federrath, 2016; Ntormousi & Hennebelle, 2019), but still, the constant width of filaments particularly for massive filaments remains a mystery. Still, we need to understand the origin of universal width particularly for massive filaments by examining the detailed process of gas accretion flows onto the filament. We expect that the SSI can deposit additional energy to the filament, because the corrugation of the shock front generally leads to turbulent flows behind the shock (e.g., Inoue et al., 2012; Inoue & Inutsuka, 2012b). Eqs. (1.22) and (1.23) show that the most unstable scale is infinitesimally small. This unphysical feature is caused by ideal approximation and results in the discontinuous treatment of the shock. To know the physical scale length of the SSI, we take ambipolar diffusion into account. As the first step to understanding the effect of SSI on filament width, we study the effect of ambipolar diffusion on the SSI and derive the most unstable scale. In realistic situations, filaments are bound by two shocks. Because the separation of these two shocks is narrow and they are threaded by the same magnetic field lines, we can expect that the two shocks dynamically influence each other. As the second step, we study the effect of interacting two shocks and show that the slow shock instability mediates inhomogeneous postshock flows and can provide additional dynamical pressure to the filament. As the third step, we perform a three-dimensional SSI simulation including self-gravity and ambipolar diffusion, and compare the column density profile and filaments width with observations. We challenge to explain the origin of the universality of filament width.

Chapter 2

Classification of Filament Formation Mechanisms

2.1 Short Introduction

Previous theoretical research on filament formation proposed many types of mechanisms as shown in §1.2.2. However, it is still unclear which type is responsible for producing star-forming filaments. Most proposed mechanisms, including types I, O, C, and possibly type G, are triggered by shock compression. In this study, we perform a series of isothermal MHD simulations to investigate filament formation by shock waves, focusing on the impacts of shock strength, turbulence, and self-gravity on the filament formation mechanism Note here that, since type I is effective only in highly super-Alfvénic turbulence, we hardly observe it in our simulations performed under a realistic 10 μG initial magnetic field. In addition, we analyze the line-mass distribution of the simulated filaments. The paper is organized as follows: In §2, we provide the setup of our simulations, and we show and interpret the results including the filament line-mass distribution in §3. In §4, simple models account for the dominant filament formation timescale. Finally, we summarize the results in §5.

2.2 Setup of Simulations

We solve the isothermal MHD equations including self-gravity using the SFUMATO code (Matsumoto, 2007). This code integrates the MHD equations using a Godunov-type scheme and an HLLD Riemann solver (Miyoshi & Kusano, 2005), providing third- and second-order accuracy in space and time, respectively. To maintain the divergence-free condition of the magnetic field ($\nabla \cdot \mathbf{B} = 0$), we employ the divergence cleaning method (Dedner et al., 2002). Poisson's equation is solved using a multi-grid method.

We investigate the mechanism of filament formation induced by shock waves by performing converging flow simulations. A schematic illustration of the initial condition is shown in Figure 2.1. We prepare a cubic numerical domain of side lengths $L_{\rm box} = 6.0$ pc consisting of 512^3 uniform numerical cells, indicating

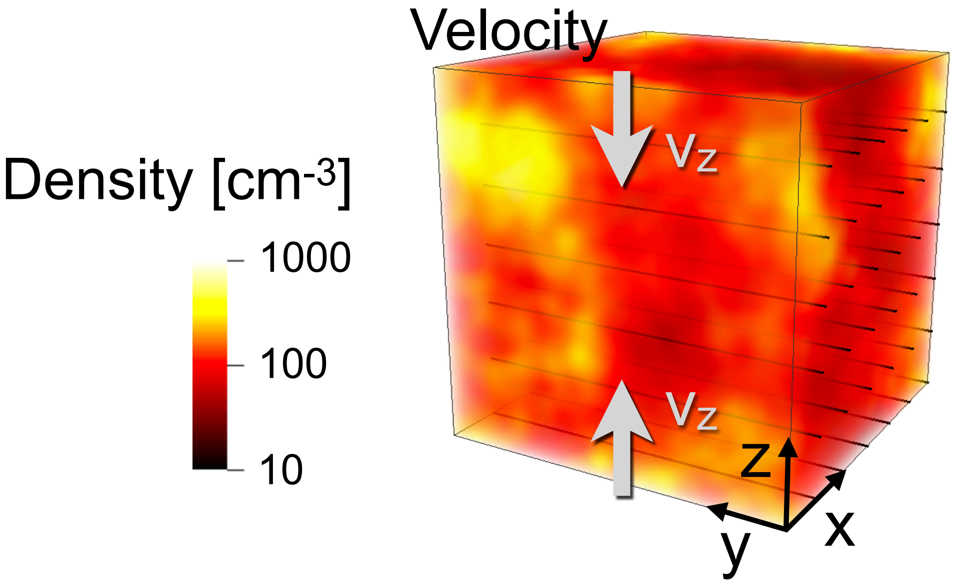

Figure 2.1: Schematic diagram of initial condition. The color bar represents the density magnitude; the black lines are the initial magnetic field lines; and the grey arrows indicate the orientations of the converging flows.

that the physical resolution Δx is approximately 0.012 pc. We initially set the isothermal gas characterized by the isothermal sound speed at $c_s = 0.2$ km s^{-1}. Because molecular clouds are highly inhomogeneous by nature, we initially add isotropic density fluctuations given as a superposition of sinusoidal functions with various wavenumbers from $2\pi/L_{\rm box} \leq |k| \leq 32\pi/L_{\rm box}$ and random phases. The power spectrum of the density fluctuations is given by $(\log\rho)_k^2 \propto k^{-4}$, which can be expected as a consequence of supersonic turbulence (Beresnyak et al., 2005; Elmegreen & Scalo, 2004; Scalo & Elmegreen, 2004; Larson, 1981; Heyer & Brunt, 2004). Thus, the initial density structure of our simulations is parameterized by mean density $\bar{n}_0 = \bar{\rho}_0/m = 100$ cm^{-3} and dispersion $\Delta n/\bar{n}_0 = 0.5$, where $\bar{\rho}_0$ and $m = 2.4\ m_{\rm proton}$ are the mean mass density and the mean mass of the molecular gas particles, respectively. In addition to density fluctuations, we set the initial turbulent velocity field depending on the model summarized in Table 3.1. The initial turbulent velocity fluctuation has a dispersion of 1.0 km s^{-1} with a power spectrum of $v_k^2 \propto k^{-4}$ following Larson's law (Larson, 1981).

In addition to the turbulent component, we set the initial coherent velocity component as $v_z(z) = -(v_{\rm coll}/2)\tanh[z-3]$, i.e., two flows colliding head-on in the x-y plane at $z = 3$ pc with a relative velocity of $v_{\rm coll}$. In the previous studies that reported the type C filament formation, the filaments are created in the shock-compressed layer with a shock velocity of a few km s^{-1}. However, in the studies that found the type O mechanism, high shock velocity cases of ~ 10 km s^{-1} are studied. To systematically study the filament formation mechanism, we perform simulations using various shock velocities. Specifically, we examine cases with $v_{\rm coll} = 3$, $v_{\rm coll} = 6$, $v_{\rm coll} = 8$, $v_{\rm coll} = 10$, and 12 km s^{-1}. Table 3.1 includes a

Table 2.1: Model parameters.

Model Name	Collision Velocity $v_{\rm coll}$ [km s^{-1}]	Shock Velocity $v_{\rm sh}$[km s^{-1}]	Self-Gravity	Turbulence
v12GyTn	12	7.0	Yes	No
v12GnTn	12	7.0	No	No
v12GyTy	12	7.0	Yes	Yes
v12GnTy	12	7.0	No	Yes
v10GyTn	10	6.0	Yes	No
v8GyTn	8.0	5.0	Yes	No
v6GyTn	6.0	4.0	Yes	No
v3GyTn	3.0	2.5	Yes	No
v3GnTn	3.0	2.5	No	No
v3GyTy	3.0	2.5	Yes	Yes
v3GnTy	3.0	2.5	No	Yes

summary of the model parameters. In the model names, the number following "v" represents the value of $v_{\rm coll}$ in units of km s^{-1}, and the characters "y" and "n" following "G" and "T" represent simulation with and without self-gravity and initial turbulence, respectively.

At the x-y boundary planes, the velocity is fixed at $v_{\rm coll}/2$, and the density is given by $n_0(x, y, z = v_{\rm coll}t/2)$ for the $z = 6$ pc plane and $n_0(x, y, z = L_{\rm box} - v_{\rm coll}t/2)$ for the $z = 0$ pc plane, where $n_0(x, y, z)$ is the initial density field including fluctuations. For the z-x and y-z boundary planes, we impose periodic boundary conditions.

We initially set a uniform magnetic field of $\mathbf{B}_0 = (0, 10\ \mu\mathrm{G}, 0)$, which is perpendicular to the direction of the shock propagation. This magnetic field strength is consistent with observed magnitude in molecular clouds (e.g., Crutcher, 2012; Heiles & Crutcher, 2005). Because the magnetic field component perpendicular to the direction of the shock propagation is expected to be strongly amplified by the shock compression, whereas the parallel component is not, the initial z-component of the magnetic field would play a minor role even if it is given.

To investigate its impact on filament formation, we perform simulations both with and without considering self-gravity. In cases where self-gravity is taken into account, we employ the sink particle technique in regions where gravitational collapse is anticipated to occur. The sink particle generation condition is the same as that discussed in previous research (Inoue et al., 2018; Matsumoto et al., 2015). It should be noted that the employment of the sink particle is simply for a continuation of the simulations even after the onset of local gravitational collapse[1]. In this paper, we will not focus on the information of sink particles, because the resulting total mass of the sink particles is much smaller than that of dense filaments (for instance, the final total mass of the sink particles is only 3%

---

[1] The threshold density for the sink formation is 5.6×10^4 cm^{-3}. This value is much lower than that used in our previous studies because we do not employ the adaptive mesh refinement in the present study

to that of dense filaments for model v12GyTy, and 6% for model v3GyTy).

2.3 Results

2.3.1 High Shock Velocity Case

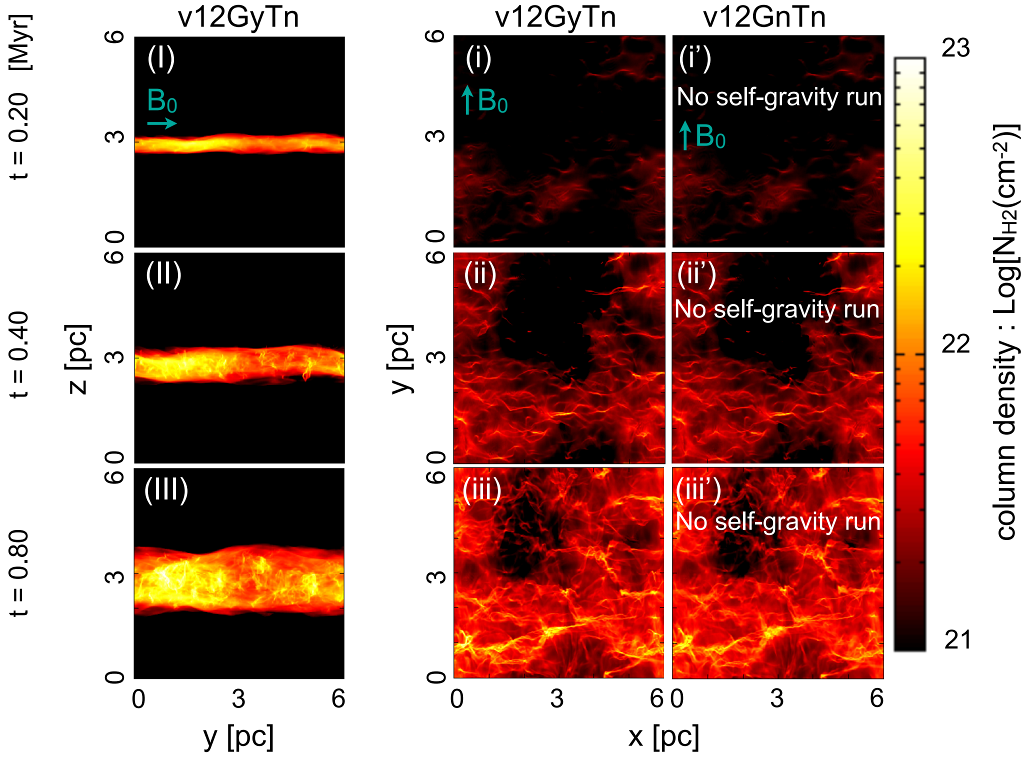

Figure 2.2: Column density maps at time t = 0.2 (*top*), 0.4 (*middle*), and 0.8 (*bottom*) Myr. *Left row* (panels I, II, and III): Column density in the y-z plane of model v12GyTn. *Middle row* (panels i, ii, and iii): Same as panels (I)-(III) but for the x-y plane. *Right row* (panels i', ii', and iii'): Same as panels (i)-(iii) but for model v12GnTn.

In the case of $v_{\rm coll} = 12$ km s^{-1}, the flow collision induces fast isothermal MHD shock waves. According to the shock jump condition (e.g., §4.1 of Fukui et al., 2020), the compression ratio of the isothermal fast shock is given by

$$\rho_1/\rho_0 = v_0/v_1 \simeq \sqrt{2}\mathcal{M}_{\rm A}, \tag{2.1}$$

where $\mathcal{M}_A \equiv v_0/v_{\rm Alf,0}$ is the Alfvénic Mach number, the Alfvén velocity is given by $v_{\rm Alf,0} = B_0/\sqrt{4\pi\rho_0}$ and subscripts 0 and 1 indicate preshock and postshock values respectively. The preshock velocity in the shock rest-frame v_0 is equivalent to the shock velocity in the upstream rest frame $v_{\rm sh}$. Given that the numerical domain is on the postshock rest frame, the shock wave propagates with the velocity of

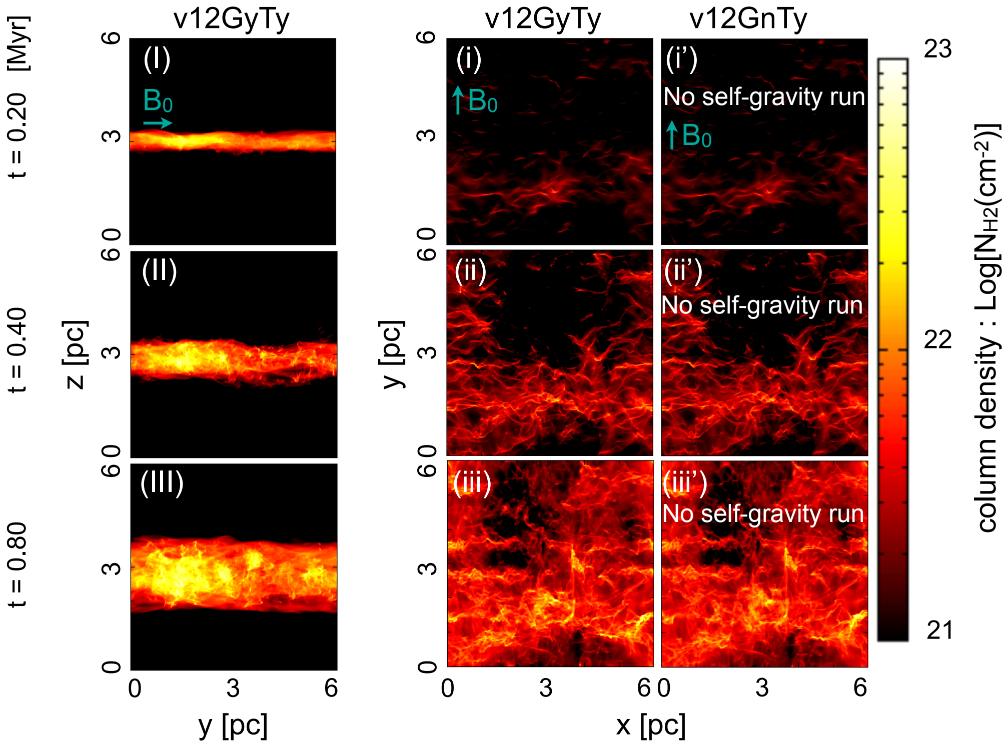

Figure 2.3: Column density maps at time t = 0.2 (*top*), 0.4 (*middle*), and 0.8 (*bottom*) Myr. *Left row* (panels I, II, and III): Column density in the y-z plane of model v12GyTy. *Middle row* (panels i, ii, and iii): Same as panels (I)-(III) but for the x-y plane. *Right row* (panels i', ii', and iii'): Same as panels (i)-(iii) but for model v12GnTy.

$v_1 \simeq v_0/(\sqrt{2}\mathcal{M}_{\rm A})$. The relation between the converging flow velocity $v_{\rm coll}$ and the shock velocity $v_{\rm sh}$ is given by

$$\begin{aligned} v_{\rm sh} &= v_{\rm coll}/2 + v_1 \\ &\simeq v_{\rm coll}/2 + v_{\rm Alf,0}/\sqrt{2} \\ &\simeq 6\left(\frac{v_{\rm coll}}{12~{\rm km~s^{-1}}}\right)~{\rm km~s^{-1}} \\ &\quad +1\left(\frac{B_0}{10~\mu{\rm G}}\right)\left(\frac{n_0}{100~{\rm cm^{-3}}}\right)^{-1/2}~{\rm km~s^{-1}}. \end{aligned} \tag{2.2}$$

In Figure 2.2, we show snapshots of the column density structure of the results of models v12GyTn and v12GnTn at $t = 0.2$ (top), 0.40 (middle), and 0.60 (bottom) Myr. In constructing the column density, we identify the shock fronts and integrate the density only in the shock-compressed region. To identify the shock fronts, we scan the total pressure $\rho(x,y,z)c_{\rm s}^2 + B^2(x,y,z)/8\pi$ along the z-axis from upstream ($z = 0$ and 6) to downstream ($z = 3$) and define the two shock fronts as the largest and smallest locations of $z(x,y)$ where the following condition is satisfied:

$$\rho(x,y,z)c_{\rm s}^2 + B^2(x,y,z)/8\pi \geq f_{\rm jump} \times \bar{\rho}_0 v_{\rm coll}^2. \tag{2.3}$$

Here, we choose $f_{\text{jump}} = 0.2$ for convenience, but we confirmed that the result with f_{jump}=0.4 gives the indistinguishable result to $f_{\text{jump}} = 0.2$ case.

Panels (I)-(III) and (i)-(iii) in Figure 2.2 show column density snapshots of model v12GyTn in the y-z and x-y planes, respectively. Panels (I), (II), and (III) show two shock waves induced by the converging flows propagating toward the positive and negative z-directions. Panels (i)-(iii) and (i')-(iii') show the formation of many filaments regardless of the effect of self-gravity that indicates the filament formation is not driven by self-gravity in the present high shock velocity cases. In §2.3.4, we show that very massive filaments as large as 100 $\mathrm{M}_\odot$ pc^{-1} are formed at $t = 1$ Myr in this series of high shock velocity results.

Because the present models (v12GyTn and v12GnTn) do not include initial turbulence, the type O mechanism definitively accounts for the filament formation.

In Figure 2.3, we show snapshots at $t = 0.20$ (top), 0.40 (middle), and 0.80 (bottom) Myr of models v12GyTy (panels I-III and i-iii) and v12GnTy (panels i'-iii'). In panels (i)-(iii) and (i')-(iii'), more (mostly faint) filaments parallel to the mean magnetic field lines are present compared with that shown in Figure 2.2. This indicates that type C mechanism helps to create (faint) filaments. By comparing these two models, we again find that type G does not account for filament formation. However, see below for Figure 2.8 where we will see that the resulting filaments tend to disperse in the absence of self-gravity.

To clarify the dominant filament formation mechanism, we show the local density cross-sections around the five major filaments as the results of models v12GyTn in Figure 2.4 and v12GyTy in Figure 2.5. The high-density blobs (yellow regions) in the local cross-section maps correspond to those of the major filaments. In the type O mechanism, the post-shock gas flows toward a region behind the concave shock surface, where the filament is formed. Such a characteristic flow is created due to the effect of the oblique MHD shock wave. Further details of the flow structure have been reported by Inoue & Fukui (2013) and Inoue et al. (2018). The curved shock morphology and velocity vectors (black arrows) shown in the cross-section panels in both v12GyTn and v12GyTy models clearly support the type O origin of the (major) filaments.

In principle, the flows in the post-shock region induced by the oblique MHD shock may drive turbulence in the long-term evolution. However, at least in the stage of filament formation, the converging flows along the bending magnetic field are laminar. Thus, it is not appropriate to simply say that type O filament formation is involved in the simulation of supersonic turbulence in general. Type O mechanism is expected to selectively appear in the compression by shock waves with a relatively smooth surface, such as the one caused by an expansion of the super-shell or HII region. It should be noted that we can observationally distinguish type O mechanism from the other types by measuring the structure of magnetic and velocity fields (Arzoumanian et al., 2018; Tahani et al., 2018, 2019; Bonne et al., 2020; Chen et al., 2020; Kandori et al., 2020a,b).

2.3.2 Low Shock Velocity Case

In Figure 2.6, we show snapshots at $t = 0.6$ (top), 1.4 (middle), and 1.8 (bottom) Myr of models v3GyTn (panels I-III and i-iii) and v3GnTn (panels i'-iii'). From Eq. (2.2), the average shock velocity is calculated to be 2.5 km s^{-1} for $v_{\rm coll} = 3$ km s^{-1} simulations presented in this section. Although filamentary structures are created in panel (iii), no obvious dense filaments are shown in panel (iii'). This suggests that the type O mechanism does not work for this low shock velocity case and that self-gravity (type G) accounts for the filament formation in model v3GyTn.

Figure 2.7 shows snapshots at $t = 0.4$ (top), 1.20 (middle), and 2.00 (bottom) Myr of model v3GyTy (panels I-III and i- iii) and the model v3GnTy (panels i'-iii'). The similar filamentary structure formation occurring at $t = 0.4$ and 1.2 Myr in both models suggests that type C filament formation is important for the low shock velocity models[2]. In the later stage of $t = 2.0$ Myr, the results of model v3GyTy show that the filaments are attracted to each other by the self-gravity that eventually induces filament collisions and enhances the filament line mass. More detailed analysis is given in §2.3.4.

2.3.3 Filament Formation Timescale vs. Free-Fall Time

In this section, we use the following procedure to compute the filament formation time. First, we identify the filaments by employing the FilFinder algorithm (Koch & Rosolowsky, 2015) that returns filament skeletons for a given input two-dimensional image. A skeleton is a single-pixel-width object that corresponds to the major axis of a filament. To focus on major filaments, we neglect filaments having column density smaller than $1.5 \times \bar{N}_{\rm sh}$, where $\bar{N}_{\rm sh}$ is the mean column density of the shocked region. We confirmed that the result does not change even if we change the factor 1.5 to 2.0. We stress that because of this minimum column density requirement for the filament identification, our analysis is given below always omits faint filaments with column densities smaller than $1.5 \times \bar{N}_{\rm sh}$.

Then, we calculate the filament mass fraction $F_{\rm fil}$ defined by

$$F_{\rm fil} \equiv M_{\rm fil,tot}/M_{\rm sh}, \tag{2.4}$$

where $M_{\rm fil,tot}$ and $M_{\rm sh}$ are the total mass of the filaments in the snapshot and the shocked region mass, respectively. $M_{\rm fil,tot}$ is computed by integrating the gas column density over the region around 0.1 pc of the filament skeleton (Arzoumanian et al., 2011; Koch & Rosolowsky, 2015). Using the $F_{\rm fil}$, we define the filament formation time $t_{\rm fil}$ as the time at which the filaments are produced most actively. Specifically, The time at which $\Delta F_{\rm fil}/\Delta t$ reaches its maximum value is defined as the $t_{\rm fil}$. Where Δt and $\Delta F_{\rm fil}$ are the one-tenth of free-fall time $t_{\rm ff}$ in the shocked layer and the increment of $F_{\rm fil}$ in the time interval Δt, respectively.

The free-fall time in the post-shock layer, which gives the timescale of the

---

[2] Even in the low shock velocity models, some major filaments appear to be formed by type O mechanism.

self-gravitating sheet fragmentation (Nagai et al., 1998), can be estimated as

$$\begin{aligned} t_{\rm ff} &= \sqrt{\frac{1}{2\pi G \bar{\rho}_1}} \\ &= \sqrt{\frac{\bar{v}_{\rm Alf}}{2\sqrt{2}\pi G \bar{\rho}_0 \bar{v}_{\rm sh}}} \\ &= \sqrt{\frac{B_0}{4\sqrt{2}\pi^{3/2} G \bar{\rho}_0^{3/2} \left(v_{\rm coll}/2 + B_0/\sqrt{8\pi\bar{\rho}_0} \right)}} \\ &\simeq 1.0 \ {\rm Myr} \left(\frac{B_0}{10 \ \mu{\rm G}} \right)^{1/2} \left(\frac{\bar{n}_0}{100 \ {\rm cm}^{-3}} \right)^{-3/4} \\ &\times \left[\left(\frac{v_{\rm coll}}{12 \ {\rm km/s}} \right) + 0.17 \left(\frac{B_0}{10 \ \mu{\rm G}} \right) \left(\frac{\bar{n}_0}{100 \ {\rm cm}^{-3}} \right)^{-1/2} \right]^{-1/2}, \end{aligned} \tag{2.5}$$

where $\bar{\rho}_1 \simeq \sqrt{2}\mathcal{M}_{\rm A}\bar{\rho}_0$ and $\bar{v}_{\rm Alf} = B_0/\sqrt{4\pi\bar{\rho}_0}$ are the mean density of the shocked layer and the mean Alfvén velocity, respectively (from eq. [2.1]), and $\bar{v}_{\rm sh} = v_{\rm coll}/2 + v_1 \simeq v_{\rm coll}/2 + B_0/\sqrt{8\pi\bar{\rho}_0}$ represents the mean shock velocity (eq. [2.2]).

Figure 2.8 represents the evolution of the filament mass fraction for the high shock velocity models, in which the time is normalized by the free-fall time $t_{\rm ff}$. As we have shown in § 2.3.1, major filaments in these models are created by the type O mechanism. Figure 2.8 confirms that the formation timescale of the filaments by type O mechanism is much faster than the timescale of self-gravity.

Figure 2.9 shows the evolution of the filament mass fraction for the low shock velocity models. In the results of model v3GyTn (panel c), the filament formation time $t_{\rm fil}$ coincides with the free-fall time $t_{\rm ff} \simeq 1.6$ Myr. This supports our discussion in § 2.3.2 such that the filaments are created by type G mechanism. In panels (d) and (d'), type C occurs earlier than the free-fall time.

Figure 2.10 shows the evolution of the filament mass fraction (solid lines) and the filament formation time (dashed lines) for the several shock velocity models without turbulent velocity fluctuation such as v12GyTn (cyan), v10GyTn (blue), v8GyTn (purple), v6GyTn (red), and v3GyTn (orange). We can confirm that the filament formation time increases with a decrease in shock velocity, indicating that the dominant filament formation mechanism gradually changes with a decrease of shock velocity from the type O to type G mechanism. Figure 2.10 suggests threshold collision velocity for type O mechanism is approximately $v_{\rm coll} \sim 4.5$ km s^{-1}, corresponding to $v_{\rm sh} \sim 3.3$ km s^{-1}.

2.3.4 Filament Line Mass Function

To calculate the line-mass histogram, we utilize the filament skeletons identified in the previous section. To do so, we first determine the direction perpendicular to the filament at each grid on the filament skeleton in the projection plane. Then, we compute the line mass of the filament at each skeleton grid by integrating the gas column density along the normal directions within 0.1 pc of the skeleton grid. As a result, the line mass evaluated in our histogram represents the local apparent line mass at each skeleton grid in the 2D projection plane, rather than the average line mass of each filament.

In the top panels of Figure 2.11, we plot the line-mass functions of model v12GyTn at $t \simeq t_{\rm fil}$ (top-left) and a later stage of $t = 1.3$ Myr (top-right). The bottom panels are the same as the top panels but for model v12GyTy. The horizontal and vertical axes are the local line mass of the filament at a skeleton pixel (or a point on the filament axis) $M_{\rm line}$ and the number of pixels on filament axes (skeletons), respectively. The pixel size equals to 6/512 pc $\simeq$ 0.012 pc. The black line represents the power-law function with the Salpeter index, and the green and the black dashed lines show the critical line mass with and without magnetic field support, respectively, i.e., $M_{\rm line,cr} = 2c_{\rm s}^2/G \sim 17$ M$_\odot$ pc^{-1} (Stodólkiewicz, 1963; Ostriker, 1964) and

$$\begin{aligned} M_{\rm line,cr,B} &= 2.24\frac{B_1 w}{G^{1/2}} + 15.4\frac{c_s^2}{G} \\ &\simeq 13.5\left(\frac{w}{0.1\ {\rm pc}}\right)\left(\frac{\bar{n}_0}{100\ {\rm cm}^{-3}}\right)^{1/2} \\ &\quad \times\left[\left(\frac{v_{\rm coll}}{12\ {\rm km\ s}^{-1}}\right)\right. \\ &\quad \left. +0.17\left(\frac{B_0}{10\ \mu{\rm G}}\right)\left(\frac{\bar{n}_0}{100\ {\rm cm}^{-3}}\right)^{-1/2}\right] M_\odot{\rm pc}^{-1} \\ &\quad +15.4\left(\frac{c_s}{0.2{\rm km\ s}^{-1}}\right)^2 M_\odot{\rm pc}^{-1}, \end{aligned} \tag{2.6}$$

derived by Tomisaka (2014), where $B_1 = \sqrt{2}\mathcal{M}_{\rm A}B_0$ and w are the mean magnetic field in the shocked region and the width of filaments, respectively. Note that eq. (2.6) is estimated by using the mean magnetic field strength in the shocked layer, which does not give the exact magnetic field strength threading the filaments. In models v12GyTn and v12GyTy, most of the line-masses are sub-critical at $t \simeq t_{\rm fil}$ (panels [e] and [g] in Figure 2.11), but they quickly evolve into super-critical ones by continuous accretion flows induced by the oblique shock in roughly 1 Myr (panels [f] and [h] in Figure 2.11).

In panels (f) and (h) of Figure 2.11, we can see that the filament line-mass functions have a Salpeter-like slope $\propto M_{\rm line}^{-1.35}$ at large line-masses. This slope is similar to the line-mass function found in André et al. (2019). Interestingly, this slope is the same as the high mass part of the core mass function of Inutsuka (2001). To understand the physical reason for this agreement between specific models and the Salpeter-like slope, we have to do more simulations by varying the parameters in our models. This will be done in our next work.

Recent observations suggest that high line-mass filaments greater than 100 M$_\odot$ pc^{-1} are strong candidates for massive star progenitors (Fukui et al., 2019; Shimajiri et al., 2019; Tokuda et al., 2019). We stress that such high line-mass filaments are naturally created in high shock velocity models in a short time.

In Figure 2.12, we show the filament line-mass function for the low shock velocity cases at $t \simeq t_{\rm fil}$ (left panels) and at the time when the maximum line-mass exceeds 100 $\mathrm{M}_\odot$ pc^{-1} (right panels). In the results of model v3GyTn, the filaments have almost critical line mass at $t = t_{\mathrm{fil}}$ (panel i), which is consistent with our finding that the filaments are formed by type G mechanism in this model. Panels (k) and (l) for model v3GyTy show that type C mode can create super-critical filaments. However, the formation of massive filaments around 100 $\mathrm{M}_\odot$ pc^{-1} requires a relatively long time, i.e., more than 2 Myr after $t = t_{\mathrm{fil}}$.

To compare the histograms in models without self-gravity to the ones with self-gravity, in Figure 2.13, we show line-mass functions for models v12GnTn, v12GnTy, v3GnTn, and v3GnTy. The line-mass functions in panels (m) to (p) are comparable to those in panels (e) to (h), respectively. This suggests that star-forming filaments can be formed regardless of self-gravity. In panel (t), we observe that low line-mass filaments vanish and a significant portion of the filament mass function is truncated compared to panel (l). This indicates that low line-mass filaments created by type C are transitory, and self-gravity is necessary for the formation of massive filaments. It should be noted that we impose a column density threshold of $1.5 \times \bar{N}_{\mathrm{sh}}$ for filament identification. The threshold column density for the filament identification in model v3GnTy at $t = 2.3$ Myr is set at 6.5×10^{21} cm^{-2}. The corresponding minimum line mass of the identified filament is 13 $\mathrm{M}_\odot$ pc^{-1} when the filament width is 0.1 pc.

2.3.5 Role of Shear: Angle between Filaments and Magnetic Field

In the type S mechanism, shear motions in turbulence create faint filaments parallel to the magnetic field (Soler et al., 2013; Soler & Hennebelle, 2017; Körtgen & Soler, 2020; Inoue & Inutsuka, 2016). To further investigate the role of the shear flow, we compute probability distribution histograms based on the angles between the filaments and the mass-weighted average magnetic field in the projection plane. As we have already determined the filament skeletons, it is straightforward to calculate the angle.

We show angle histograms of model v12GyTy at $t = 0.2$ (panels a and b), 0.4 (panels c and d), and 0.8 (panels e and f) Myr in Figure 2.14. The top and bottom panels are results when $t \simeq t_{\mathrm{fil}}$ (see §2.3.3 and Figure 2.8 panel b) and $t \simeq t_{\mathrm{ff}}$ (eq. [2.5]), respectively. Left panels (a), (c), and (e) are the angle histograms for the filaments in the column density range of 0.5 $\bar{N}_{\mathrm{sh}}$ to 1.5 $\bar{N}_{\mathrm{sh}}$. Right panels (b), (d), and (f) are the histograms for the filaments with $N > 1.5$ $\bar{N}_{\mathrm{sh}}$. We observe that the majority of filaments, particularly dense filaments, in the right panels are oriented perpendicular to the magnetic field. In later times, the less prominent filaments shown in the left panels alter their angle from being perpendicular to parallel with the local magnetic field. The influence of turbulent shear (type S mode) can explain this evolution naturally.

In Figure 2.15, we show angle histograms of model v3GyTy at $t = 0.4$ (panels g and h), 1.15 (panels i and j), and 2.0 (panels k and l) Myr. Top and bottom panels are results at $t \sim t_{\mathrm{fil}}$ and $t \sim t_{\mathrm{ff}}$, respectively. As Figure 2.14, the left panels are for filaments having the column density in the range of 0.5 $\bar{N}_{\mathrm{sh}}$ to 1.5 $\bar{N}_{\mathrm{sh}}$, and the right panels are for filaments with 1.5 $\bar{N}_{\rm sh}$. The trend is basically the same as the result of larger shock velocity simulation (v12GyTy; Figure 2.14), but the angle distributions are more dispersed especially for fainter filaments (left panels). This is because model v3GyTy has a slower evolution timescale than model v12GyTy and has more time for the fainter filaments to be stretched by the turbulent shear flows.

These results confirm that, except in regions of high column density, the turbulent shear flow elongates the gas structure over time to create a low-density filamentary structure. However, in this case, the filaments are aligned with the magnetic field lines and their line masses remain lower than the critical line mass (Soler et al., 2013; Soler & Hennebelle, 2017; Körtgen & Soler, 2020; Inoue & Inutsuka, 2016).

2.4 Discussion

2.4.1 PV diagram in Type O mechanism

To make it possible to compare the actual observations, we show the synthetic position-velocity (P-V) diagrams across the three major filaments in the results of the models v12GyTn (Figure 2.16) and v12GyTy (Figure 2.17). The color in the P-V diagram represents,

$$F(y,v) = \int \rho(x_0,y,z) \exp\left[-\frac{(v-v_z(x_0,y,z))^2}{c_{\rm s}^2}\right] dz. \tag{2.7}$$

The red regions in the PV diagrams correspond to filaments. In the Type O mechanism, it is shown that the gas flow behind curbed shock makes a V-shape like structure in P-V diagram (Inoue et al., 2018; Arzoumanian et al., 2018, in particular §4.2 and Figure 12), while the turbulent mechanism does not (Chen et al., 2020). The V-shaped structure in major filaments of both v12GyTn and v12GyTy clearly indicates that major filaments are created as a consequence of the oblique MHD shock compression mechanism when the gas collision velocity is high.

2.4.2 Estimation of formation time-scales

In this section, we aim to estimate the growth timescale of filaments formed by the type O (oblique shock effect) and type C (compressive flows involved in initially given turbulence) mechanisms. The goal is to understand why the dominant filament formation mechanism changes with shock velocity. We highlight that the type O and C mechanisms are distinct and have different characteristic timescales. First, we estimate the filament formation timescale for the type O mechanism. As shown schematically in panel (A) of Figure 2.18, the oblique MHD shock model predicts that the mass flux of the post-shock gas flow to the filament is given by $\rho_1 v_0 \sin\theta$, where θ is the oblique shock angle, and we have used the fact that the velocity component perpendicular to the shock normal is almost conserved across the shock[3]. If we assume constant width w of the filament, the line-mass of the filament after time t can be written as

$$M_{\rm line} = 2\rho_1 v_0 w t \sin\theta. \tag{2.8}$$

By substituting the isothermal strong MHD shock jump condition $\rho_1 \simeq \sqrt{2}\mathcal{M}_{\rm A}\rho_0$ (eq. [2.1]), the timescale $t_{\rm O}$, in which type O mechanism creates filament of the line-mass $M_{\rm line}$, is estimated in the following equation.

$$\begin{aligned} t_{\rm O} &= \frac{M_{\rm line}}{2\rho_1 v_0 \sin\theta w} \\ &= \frac{M_{\rm line} B_0}{4\sqrt{2\pi}\rho_0^{3/2} v_0^2 w \sin\theta} \\ &= 0.3 \text{ Myr } (\sin\theta)^{-1} \left(\frac{v_{\rm sh}}{7 \text{ km s}^{-1}}\right)^{-2} \\ &\times \left(\frac{M_{\rm line}}{M_{\rm line,cr}}\right) \left(\frac{n_0}{100 \text{ cm}^{-3}}\right)^{-3/2} \left(\frac{B_0}{10\ \mu\text{G}}\right) \left(\frac{w}{0.1 \text{ pc}}\right)^{-1}, \end{aligned} \tag{2.9}$$

where we have used the fact that $v_0 = v_{\rm sh}$.

Next, we consider the timescale of type C filament formation. As shown in panel (B) in Figure 2.18, the filament is formed when a turbulent flow converges in the shock-compressed slab. In the following equation, we write the velocity of the converging flows in turbulence as Δv, their scale as l, and the width of the flow as h. Because the origin of the converging flow is turbulence, we can use Larson's law $\Delta v \sim V_{08}\left(l/L_1\right)^{0.5}$, where $V_{08} = 0.8$ km s^{-1}, and $L_1 = 1$ pc (Larson, 1981). Then, the mass accumulation timescale is given by

$$t_{\rm C} = l/\Delta v \sim l^{1/2} L_1^{1/2} / V_{08}. \tag{2.10}$$

By using l and w, we can estimate the line mass of the filament as

$$M_{\rm line} = \rho_1 l w. \tag{2.11}$$

By combining, eqs (2.10)-(2.11), the timescale $t_{\rm C}$, in which the turbulent flow creates filament of the line-mass $M_{\rm line}$, can be estimated as

$$\begin{aligned} t_{\rm C} &= \frac{M_{\rm line}}{\rho_1 w \Delta v} \\ &= \left(\frac{M_{\rm line} L_1 B_0}{2\sqrt{2\pi} w V_{08}^2 \rho_0^{3/2} v_{\rm sh}}\right)^{1/2} \\ &= 0.78 \text{ Myr } \left(\frac{v_{\rm sh}}{7 \text{ km s}^{-1}}\right)^{-1/2} \left(\frac{M_{\rm line}}{M_{\rm line,cr}}\right)^{1/2} \\ &\times \left(\frac{w}{0.1 \text{ pc}}\right)^{-1/2} \left(\frac{\bar{n}_0}{100 \text{ cm}^{-3}}\right)^{-3/4} \left(\frac{B_0}{10\ \mu\text{G}}\right)^{1/2}. \end{aligned} \tag{2.12}$$

---

[3] The conservation of the parallel velocity component is exact only for the limit of no magnetic field. In the case of fast shock, the parallel velocity conservation is a highly accurate approximation.

In the top panel of Figure 2.19, we plot the two timescales $t_{\rm O}$ and $t_{\rm C}$ for the critical line-mass filament ($M_{\rm line} = M_{\rm line,cr}$) as a function of the shock velocity. We also plot the timescales for the filament with half the critical line mass ($M_{\rm line} = M_{\rm line,cr}/2$) in the bottom panel. The blue lines represent $t_{\rm O}$ with $\theta = 30°$; the red lines are $t_{\rm C}$; and dashed lines are the free-fall time in the post-shock layer (eq. [2.5]). When the shock velocity is high ($v_{\rm sh} \gtrsim 5$ km s^{-1}, i.e., $v_{\rm coll} \gtrsim 8$ km s^{-1}), we obtain the relationship of $t_{\rm O} < t_{\rm C} < t_{\rm ff}$, and for the lower shock velocity cases ($v_{\rm sh} \lesssim 5$ km s^{-1}, i.e., $v_{\rm coll} \lesssim 8$ km s^{-1}), we get $t_{\rm C} < t_{\rm ff} < t_{\rm O}$. These results are fairly consistent with the results of the simulations. That is, the type O mechanism is important for the high shock velocity case, whereas type C is more effective for the low shock velocity case.

2.5 Summary

We have performed isothermal MHD simulations of the filament formation triggered by shock compression of a molecular cloud. We found that when the shock is fast ($v_{\rm sh} \simeq 7$ km s^{-1}), the oblique MHD shock induced flows (type O) works as the major mechanism for the formation of star-forming filaments irrespective of the presence of initial turbulence and self-gravity. When the shock is slow ($v_{\rm sh} \simeq 2.5$ km s^{-1}), compressive flows involved in supersonic turbulence induce transient filament formation (type C), but the resulting filaments disperse unless the line-masses are comparable or larger than the thermal critical line-mass. If we initially input strong turbulence with velocity dispersion larger than ~ 5 km s^{-1} in the simulation, shock waves locally occur in the simulation. Thus, in principle, the type O process can occur in these simulations. However, it cannot be called ”turbulent” filamentation. On the other hand, type O can be induced almost always by a single compression of a molecular cloud by interaction with relatively fast large-scale shock waves, such as from an expanding HII region, a supernova remnant, or a super-shell. It should be noted that type O and type C can be distinguished observationally through a characteristic structure in the position-velocity map and/or curved magnetic fields as noted in studies by (see, Arzoumanian et al., 2018; Tahani et al., 2018, 2019; Chen et al., 2020; Kandori et al., 2020a,b). When the shock velocity is low and no turbulence is set initially, filaments are created (type G) through the fragmentation of the shock-compressed sheet by self-gravity over the gravitational fragmentation timescale of the dense sheet. The formation of filaments through turbulent sheet-sheet collision (type I) was not clearly observed in our simulations, as this mode seems to only be activated when a weakly magnetized, uniform-density molecular cloud is initially set.

By developing simple analytical models, we have shown that for $v_{\rm sh} \gtrsim 5$ km s^{-1}, type O is responsible for creating major filaments, while type C is more effective for $v_{\rm sh} \lesssim 5$ km s^{-1}. We conclude that the dominant filament formation mode changes with the strength of the incident shock wave. Moreover, we analyzed the line-mass distribution of the filaments and showed that strong shock waves can naturally create high-line-mass filaments such as those observed in the massive star-forming regions ($M_{\rm line} \gtrsim 100$ M$_\odot$ pc^{-1}) in a short time. We stress that such high line-mass filaments are naturally created in high shock velocity models in a timescale of the creation of the dense compressed sheet-like regions.

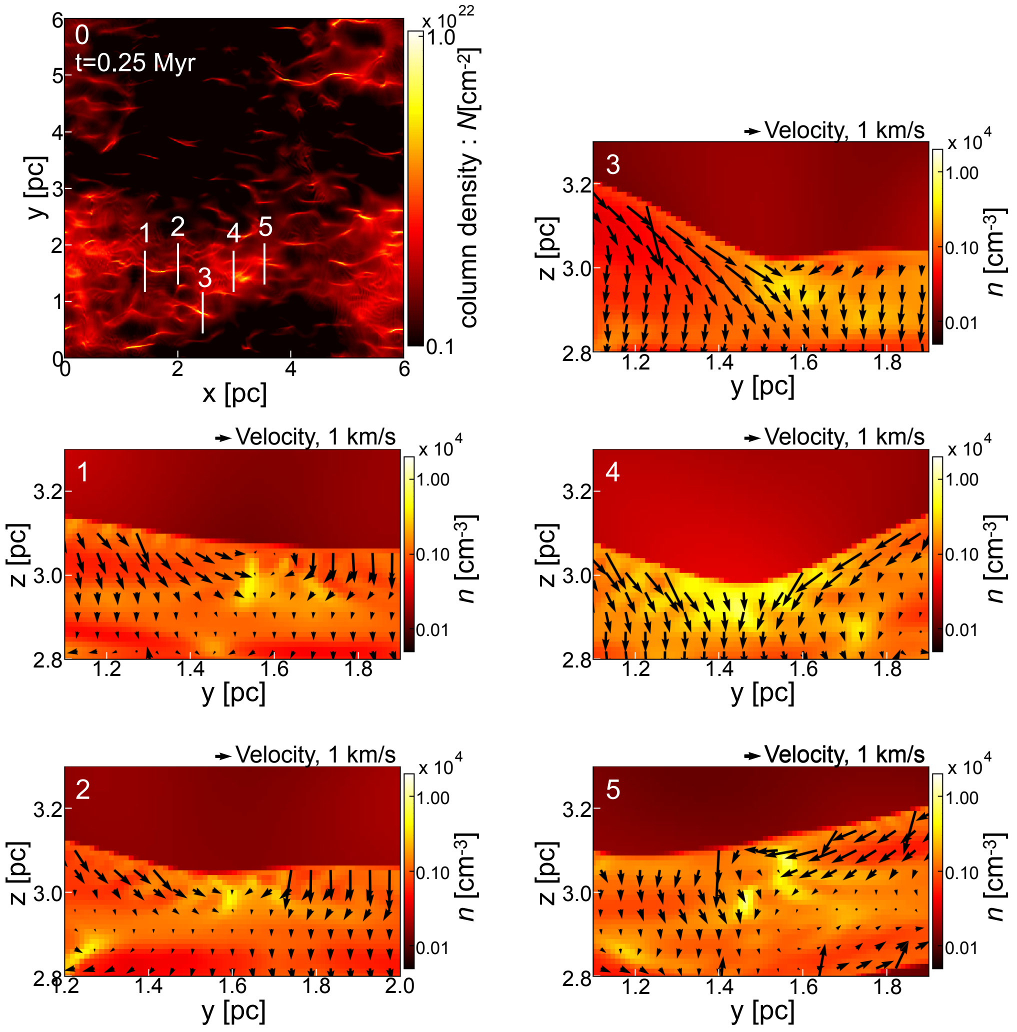

Figure 2.4: Panel (0): Early stage (t = 0.25 Myr) column density map in the x-y plane of result of model v12GyTn. The five white lines mark the planes in which the cross-section maps in panels (1)-(5) are drawn. Panels (1)-(5): Cross-section maps of the number density in the y-z plane. The yellow blobs located roughly at the center of each panel correspond to cross-sections of the filaments formed by the type O mechanism.

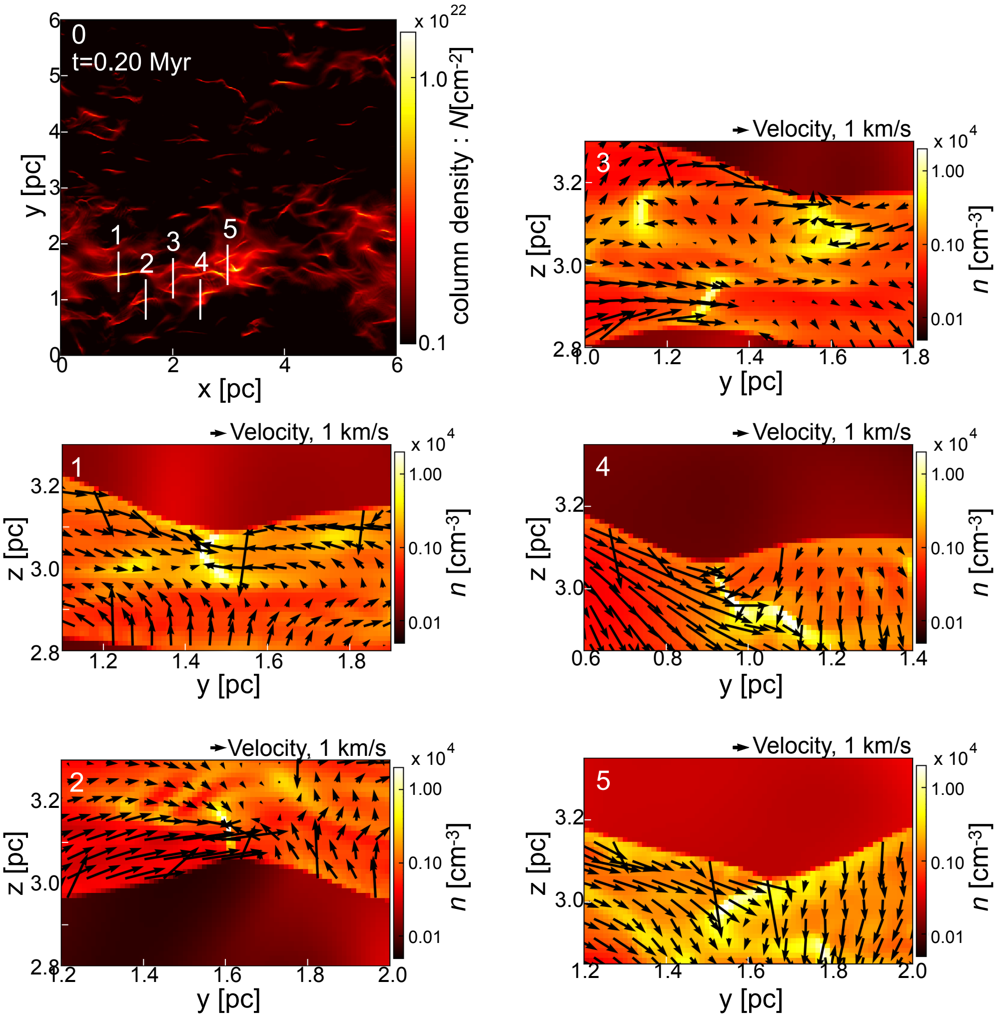

Figure 2.5: Same as Figure 2.4 but for model v12GyTy. We can confirm that the type O mechanism takes a major role in filament formation even in the case of initial turbulence.

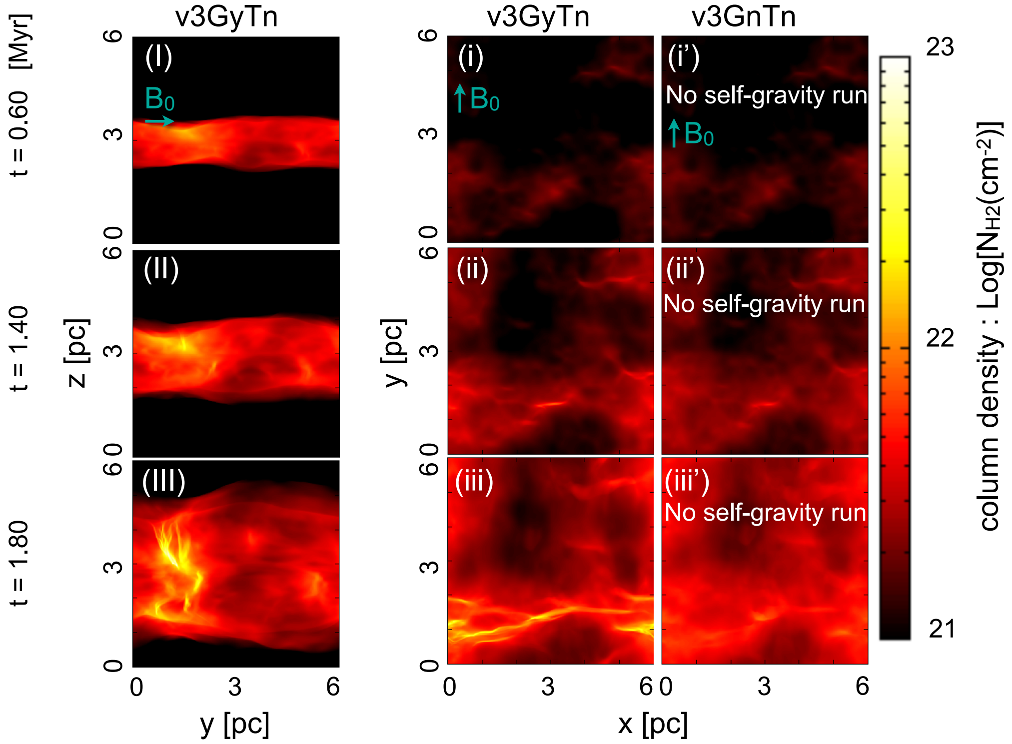

Figure 2.6: Column density maps at time t = 0.6 (*top*), 1.4 (*middle*), and 1.8 (*bottom*) Myr. *Left row* (panels I, II, and III): Column density in the y-z plane of model v3GyTn. *Middle row* (panels i, ii, and iii): Same as the panels (I)-(III) but for the x-y plane. *Right row* (panels i', ii' , and iii'): Same as the panels (i)-(iii) but for model v3GnTn.

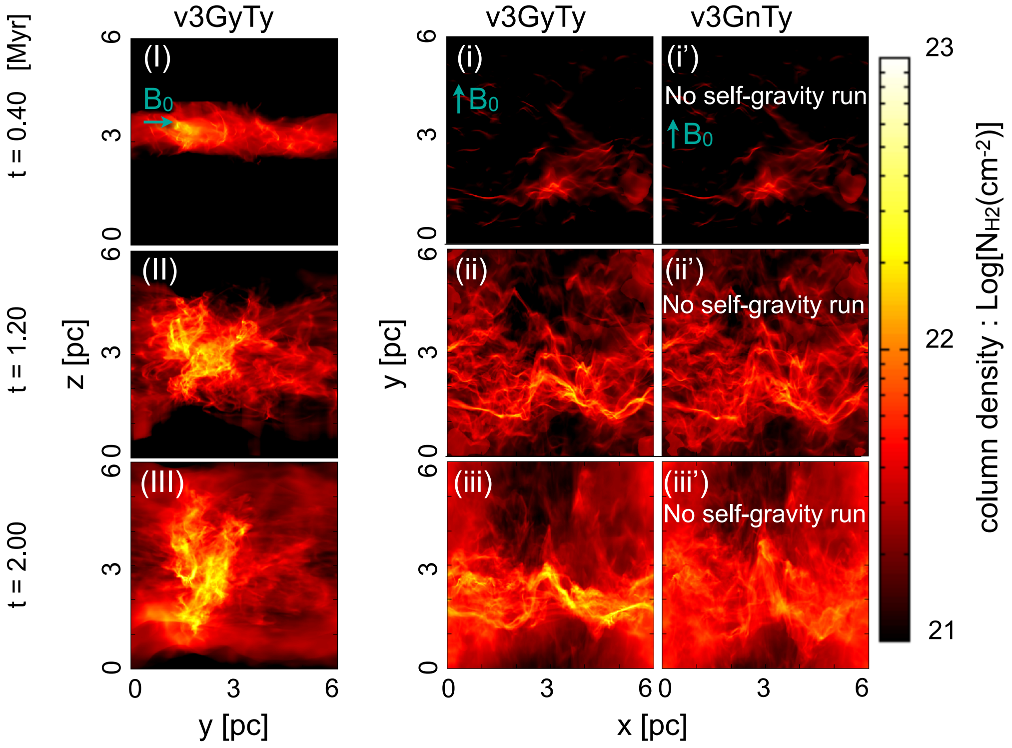

Figure 2.7: Column density maps at time t = 0.4 (*top*), 1.2 (*middle*), and 2.0 (*bottom*) Myr. *Left row* (panels I, II, and III): Column density in the y-z plane of model v3GyTy. *Middle row* (panels i, ii, and iii): Same as panels (I)-(III) but for the x-y plane. *Right row* (panels i', ii', and iii'): Same as panels (i)-(iii) but for model v3GnTy.

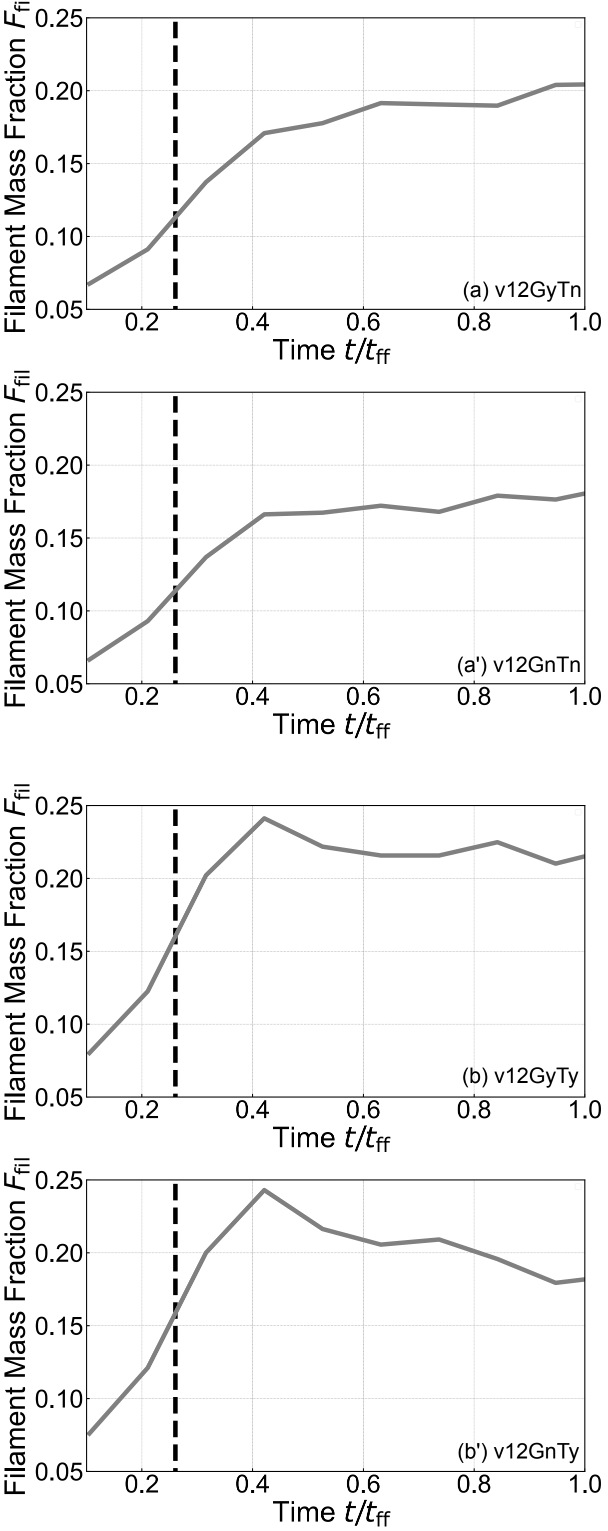

Figure 2.8: Temporal evolution of the filament mass fraction $F_{\rm fil}$ (solid line) and the filament formation time $t_{\rm fil}$ (dashed line). Panel (a), (a'), (b), and (b') are the results of models v12GyTn, v12GnTn, v12GyTy, and v12GnTy, respectively.

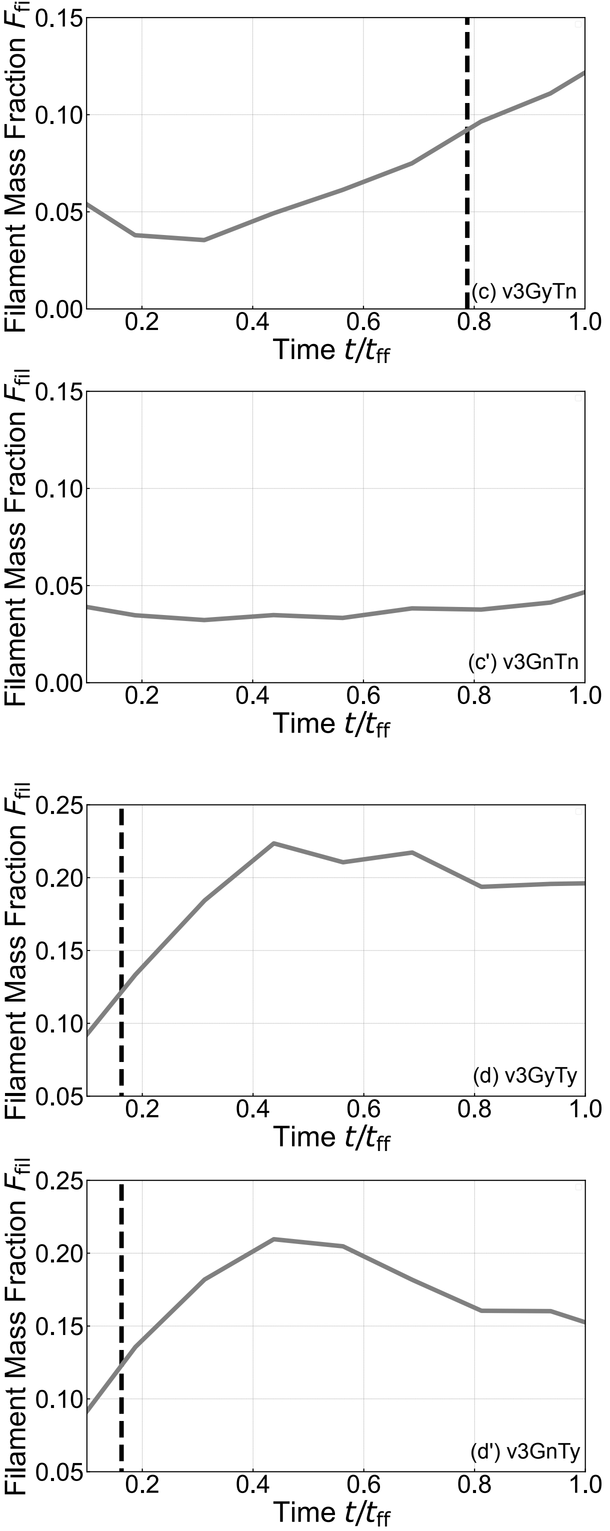

Figure 2.9: Temporal evolution of the filament mass fraction $F_{\rm fil}$ (solid line) and the filament formation time $t_{\rm fil}$ (dashed line). Panels (c), (c'), (d), and (d') are the results of models v3GyTn, v3GnTn, v3GyTy, and v3GnTy, respectively.

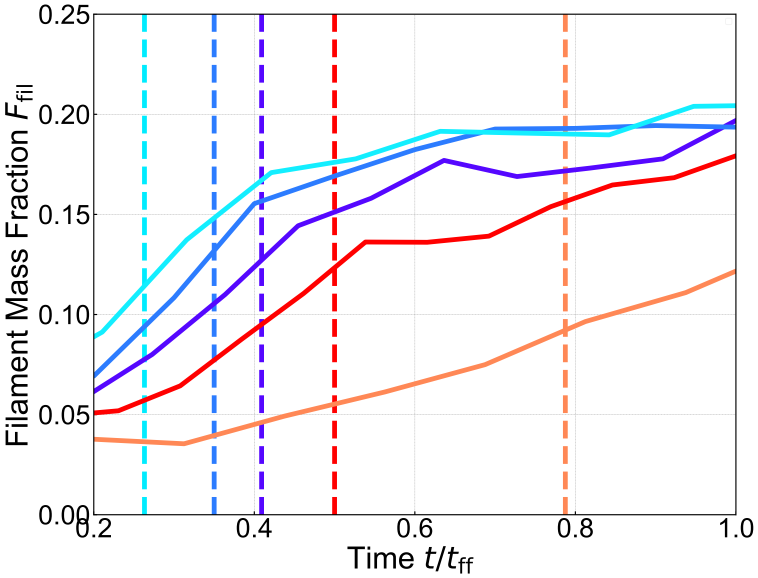

Figure 2.10: Temporal evolution of the filament mass fraction F_{fil} (solid lines) and the filament formation time t_{fil} (dashed lines) in models with self-gravity and various shock velocities but without turbulent velocity fluctuation. The colors show the results for models v12GyTn (cyan), v10GyTn (blue), v8GyTn (purple), v6GyTn (red), and v3GyTn (orange).

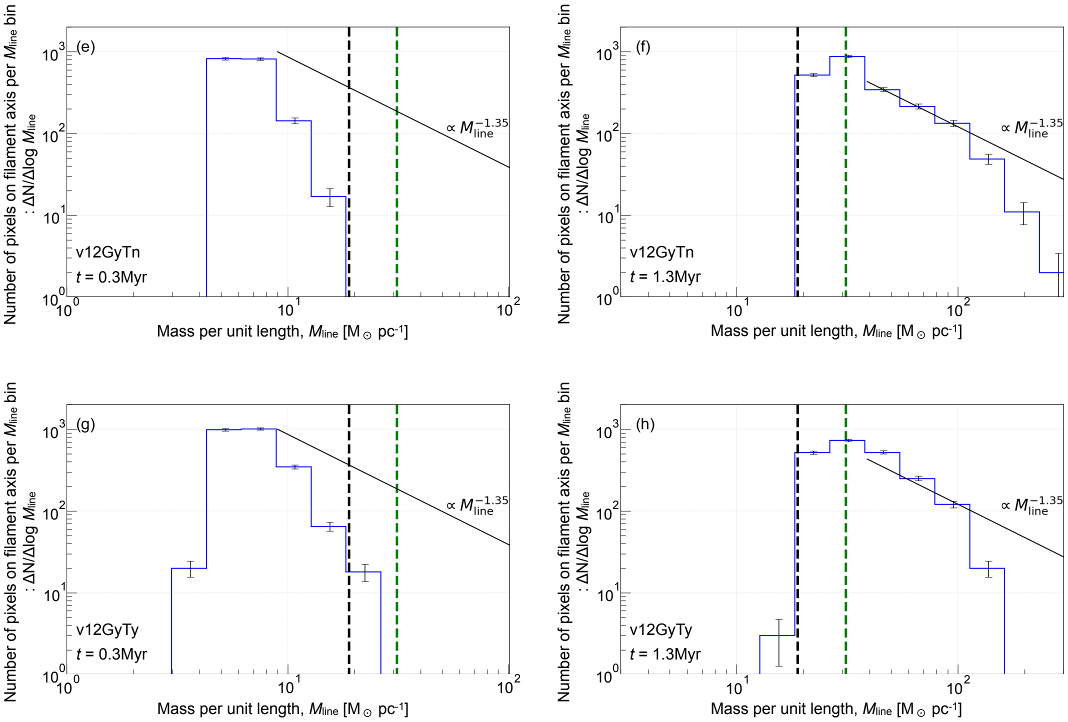

Figure 2.11: Filament mass functions for model v12GyTn (*top panels* (e) and (f)) and v12GyTy (*bottom panels* (g) and (h)). *Left panels* (e) and (g): Filaments mass functions at time $t = t_{\rm fil}$. *Right panels* (f) and (h): Results at time $t >$ 1 Myr. The black solid line represents the power-law function of the Salpeter initial mass function; the black dashed line shows the critical line-mass (Stodólkiewicz, 1963; Ostriker, 1964); and the green dashed line is the critical line-mass considering the magnetic field (Tomisaka, 2014).

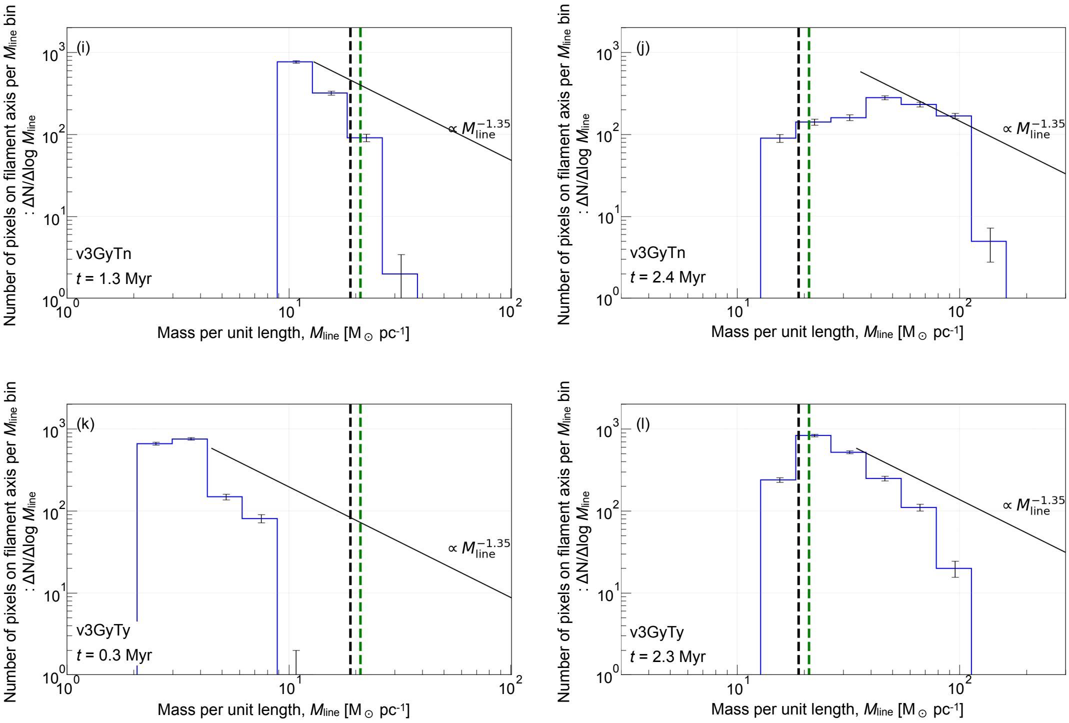

Figure 2.12: Filament mass functions for model v3GyTn (*top panels* (i) and (j)) and v3GyTy (*bottom panels* (k) and (l)). *Left panels* (i) and (k): Filament mass functions at time $t = t_{\rm fil}$. *Right panels* (j) and (l): Results at time $t >$ 2 Myr. The lines' colors are the same as those defined in Figure 2.11.

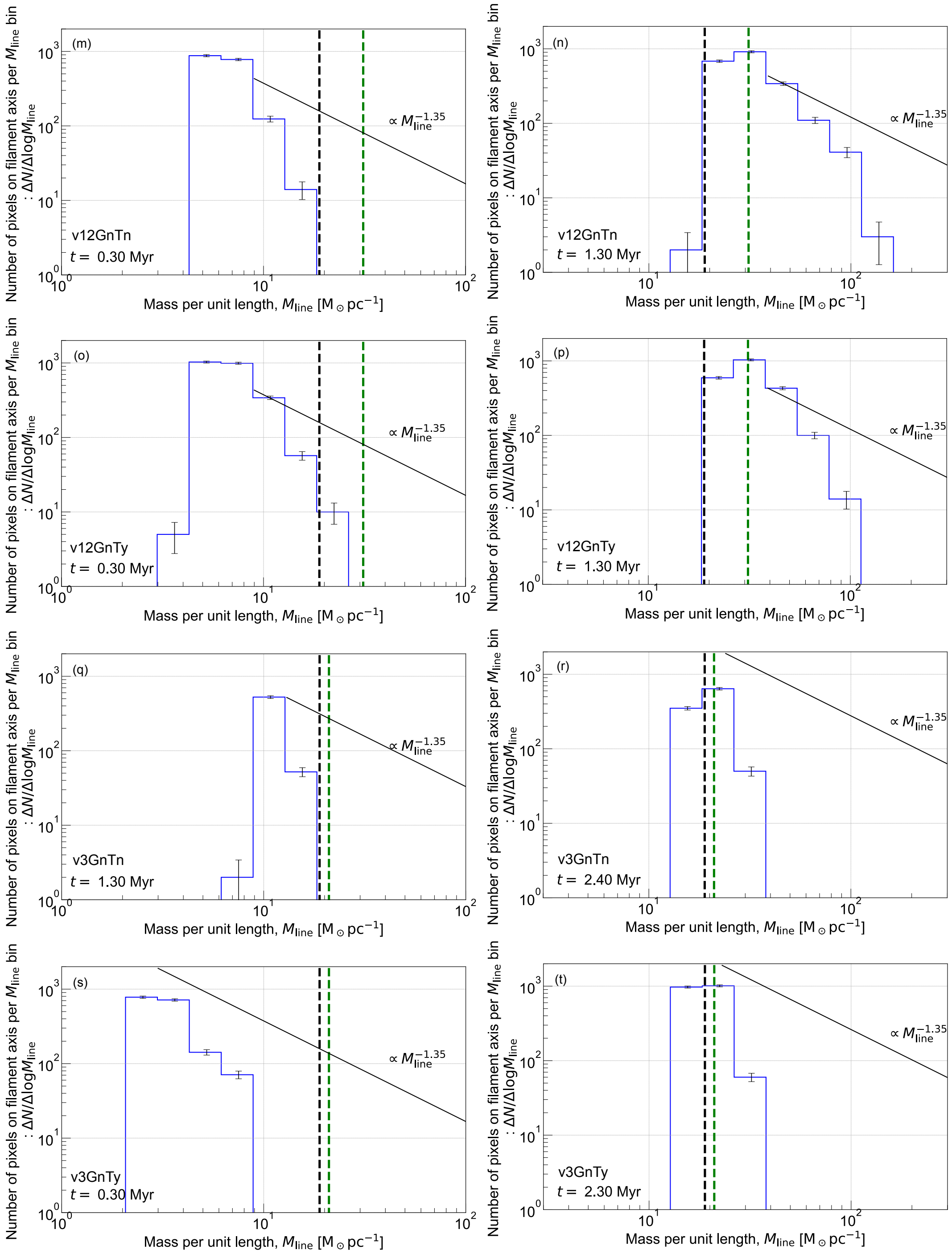

Figure 2.13: Filament mass functions for no-self-gravitating models v12GnTn (panels m and n), v12GnTy (panels o and p), v12GnTn (panels q and r), and v12GnTy (panels s and t). To compare the histograms in the models with and without self-gravity, we show the histograms that are taken at the same times in Figure 2.11 and 2.12. The lines' colors are the same as those defined in Figure 2.11.

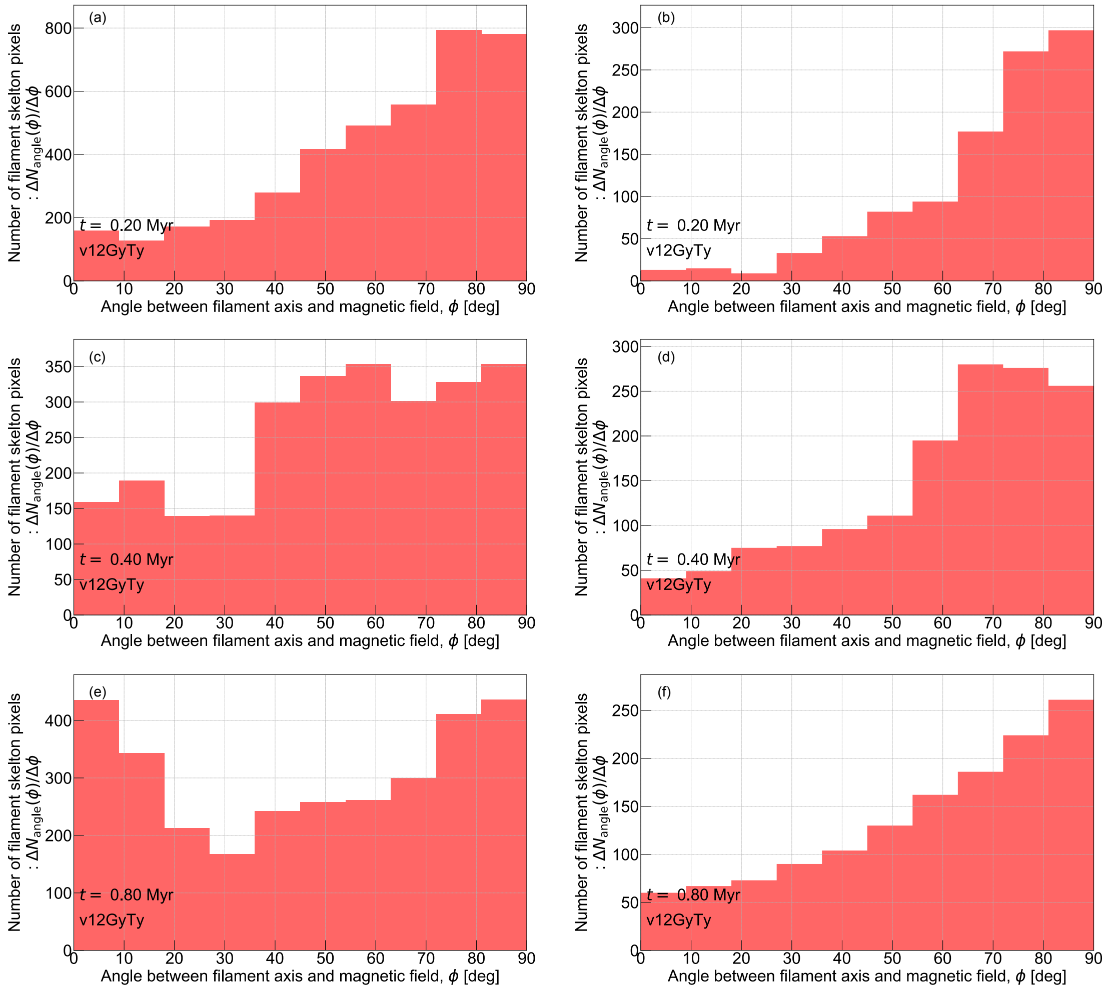

Figure 2.14: Histogram of angles between filaments and magnetic field for model v12GyTy. From top to bottom, results at time $t=$ 0.2, 0.4 and 0.8 Myr, respectively. *Top panels* (1) and (2) are results at filament formation time (see §2.3.3 and Figure 2.8). *Bottom panels* (5) and (6) are results at close to free-fall time (Eq. 2.5). *Left panels* (1), (3), and (5): Results when we identify filaments in the column density range of $0.5\bar{N}_{\rm sh}$ to $1.5\bar{N}_{\rm sh}$. *Right panels* (2), (4), and (6): Results when the filament identification threshold column density is chosen to be $1.5\bar{N}_{\rm sh}$.

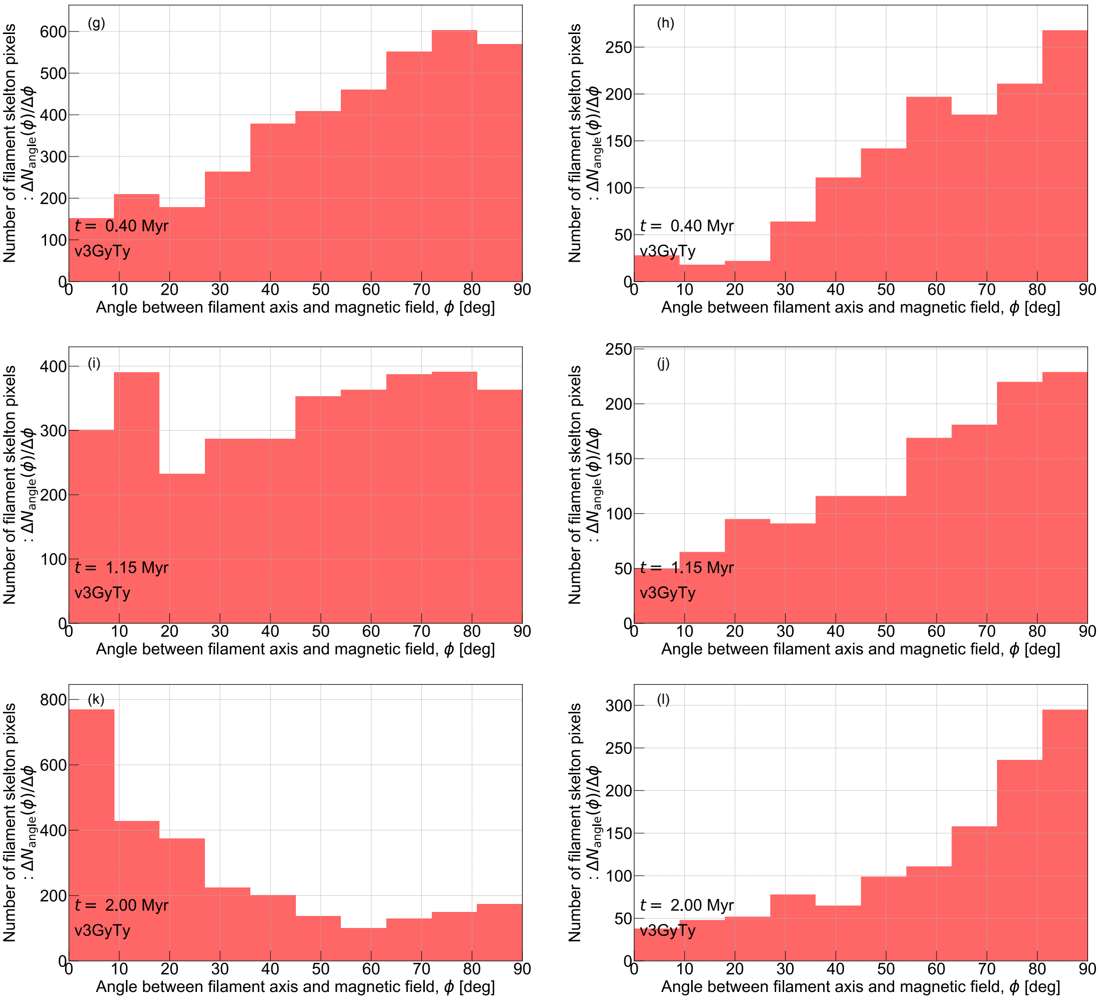

Figure 2.15: Histogram of angles between filaments and magnetic field for model v3GyTy. From top to bottom, results at time $t=$ 0.4, 1.15, and 2.0 Myr, respectively. *Top panels* (7) and (8) are results at filament formation time (see §2.3.3 and Figure 2.9). *Bottom panels* (11) and (12) are results that exceed free-fall time (Eq. 2.5). *Left panels* (7), (9), and (11): Results when we identify filaments in the column density range of $0.5\bar{N}_{\rm sh}$ to $1.5\bar{N}_{\rm sh}$. *Right panels* (8), (10), and (12): Results when the filament identification threshold column density is chosen to be $1.5\bar{N}_{\rm sh}$.

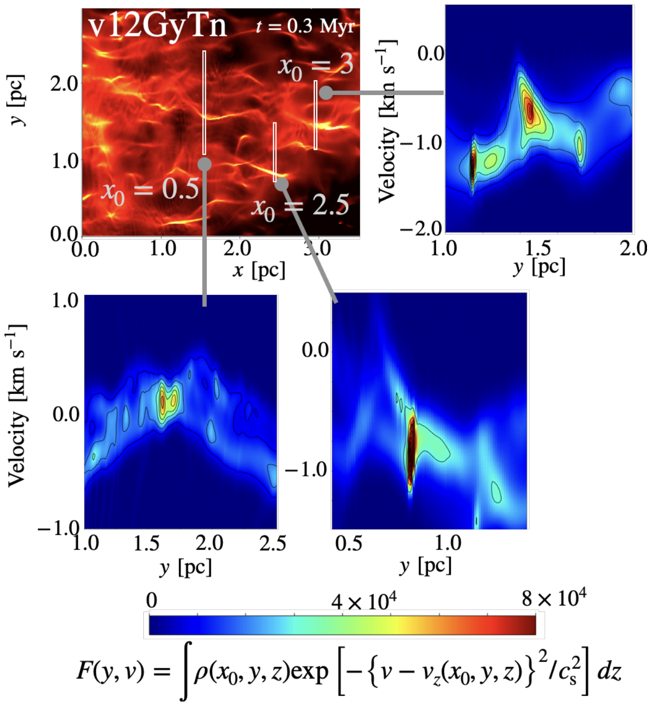

Figure 2.16: Column density map and position-velocity (PV) diagrams of the result of the model v12GyTy at time $t = 0.3$ Myr. When we make PV diagrams, we specify x-position $x_0 = 0.5,\ 2.5$, and 3.0 pc. The black line is the contour of $F(v, y)$ (see equation 2.7). The right bottom illustration is the schematic view of the filament formation process in the oblique MHD shock compression mechanism. The red regions in PV diagrams correspond to a filament. We can confirm the V-shape structure which is the supportive evidence for the oblique MHD shock compression mechanism (Arzoumanian et al., 2018).

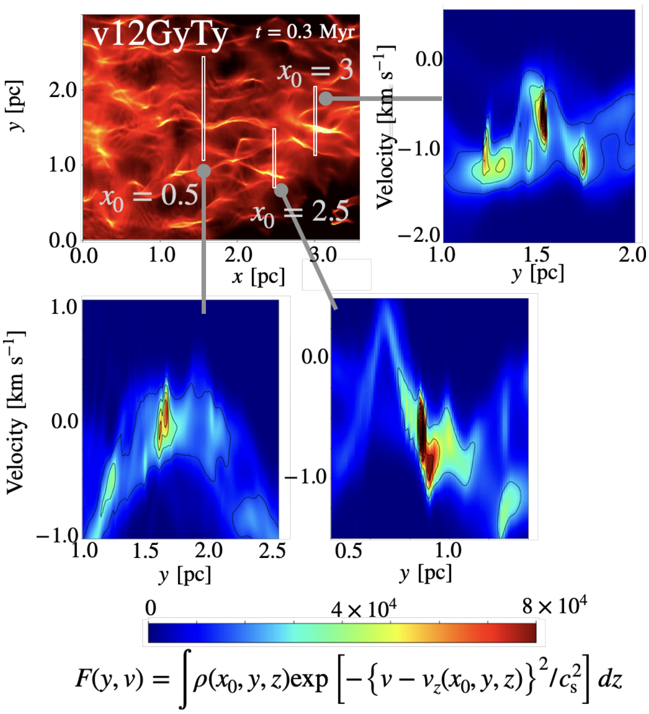

$$F(y, v) = \int \rho(x_0, y, z) \exp\left[-\left\{v - v_z(x_0, y, z)\right\}^2 / c_s^2\right] dz$$

Figure 2.17: Column density map and position-velocity (PV) diagrams of the result of the model v12GyTy at time $t = 0.3$ Myr. The dense V-shaped structures also appear in this model, indicating that the oblique MHD shock compression mechanism occurs regardless of the initial turbulence.

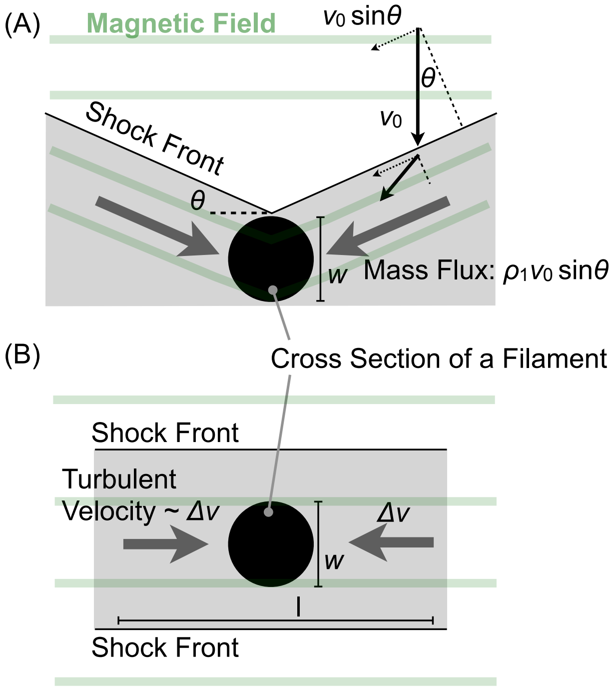

Figure 2.18: Illustrations of the models used to estimate the filament formation timescale. The gray and black regions represent the post-shock layer and filament, respectively. (A): Schematic of the oblique MHD shock compression mechanism (type O), where w is the filament width, and θ is the oblique shock angle. The angle depends on the detail of the interaction between the shock and the gas clump that evolves into the filament and is roughly $\theta \sim 30^\circ$ as indicated in Figures 2.4 and 2.5. (B): Schematic of type C (compressive flows involved in initially given turbulence) mechanism, where l is the scale of the turbulent compressive flow related to the velocity of the flow Δv via Larson's law. Here we assume the width of the compressive flows as $w = 0.1$ pc.

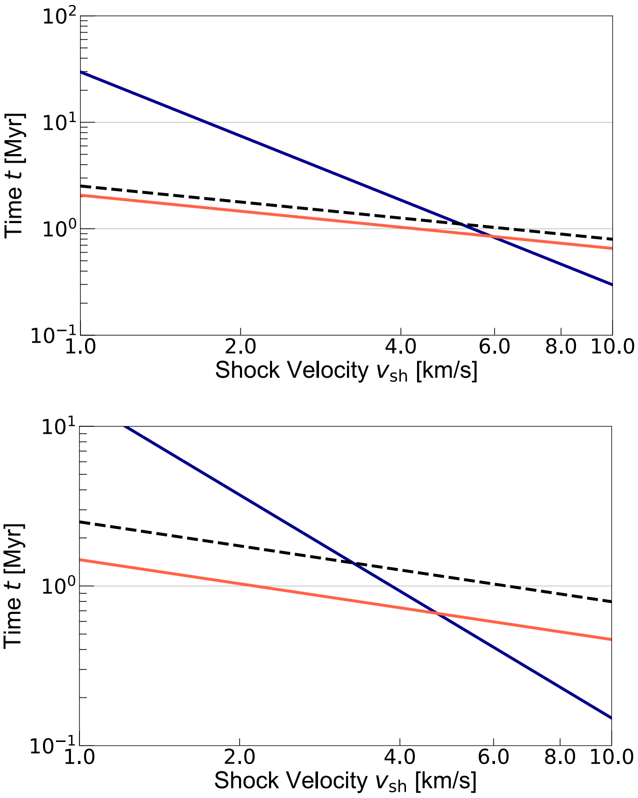

Figure 2.19: Filament formation timescales as functions of shock velocity. The blue line shows the timescale for the type O mechanism given by eq. (2.9), and the red line shows the type C timescale estimated by eq. (2.12). The dashed line represents the free-fall time in the shocked region $t_{\rm ff}$ (eq. [2.5]). *Top panel*: Timescales required to reach the thermal critical line mass (e.g., Stodółkiewicz, 1963; Ostriker, 1964), i.e., $M_{\rm line}(t) = M_{\rm line,cr}$. *Bottom panel*: Timescales required to reach half the thermal critical line mass, i.e., $M_{\rm line}(t) = M_{\rm line,cr}/2$.

Chapter 3

The Effect of Shock Wave Duration on Star Formation and the Initial Condition of Massive Cluster Formation

3.1 Short Introduction

Revealing the mechanism behind the formation of massive stars and clusters is crucial, as they significantly impact the evolution and dynamics of galaxies. Observations have shown that stars form in dense molecular filaments, regardless of their mass. The formation of these filaments has been extensively studied, with recent findings suggesting that the dominant mechanism changes with the shock velocity that triggers filament formation (Abe et al., 2021). One of the main mechanisms is "Type O," which requires a high Mach number shock to form massive filaments in the shock-compressed layer (Abe et al., 2021).

Numerical simulations of shock compression in molecular clouds through cloud collision have been compared to observations, with some studies showing that strong MHD shock compression leads to the formation of massive cores (Inoue & Fukui, 2013; Inoue et al., 2018; Sakre et al., 2021). However, these studies assumed a long-lasting shock wave (corresponding to collisions between large clouds), while the duration of a shock wave in reality depends on the situation. In contrast, simulations of unmagnetized cloud collisions showed that gravitationally bound cores do not form in the case of a short-duration shock wave (Takahira et al., 2014). Thus, a systematic study into the impact of shock duration on filament/core formation is necessary.

Enokiya et al. (2021) demonstrated that the peak column density of a star-forming region correlates with the number of OB stars in the system, and massive star clusters with more than 10 OB-type stars are associated with massive clouds whose peak column density exceeds 10^{23} cm^{-2}. Thus, the physical origin of the threshold peak column density of 10^{23} cm^{-2} must be clarified. It should be noted that the mean column density $\bar{N}_{\mathrm{H}_2}$ is related to the shock duration t_{dur}, because

$\bar{N}_{\mathrm{H}_2} = nL$ and $t_{\mathrm{dur}} = L/v_{\mathrm{sh}}$ lead to $\bar{N}_{\mathrm{H}_2} \propto t_{\mathrm{dur}}$, where $\bar{n}, L, v_{\mathrm{sh}}$ is the mean number density of a cloud, cloud size, and, shock velocity, respectively. Therefore, we can suppose that shock duration is one of the important parameters in determining peak column density. Previous simulations with a high column density core/clump as an initial condition successfully demonstrated massive star/cluster formation (Bonnell et al., 2004; Krumholz & McKee, 2008; Krumholz et al., 2009, 2012), indicating that the high column density initial core/clump leads to the massive star/cluster formation. In Krumholz et al. (2009), their initial condition, a dense core of 100 $M_{\odot}$ within 0.1 pc, was justified based on observed values of a protostellar object IRAS 05358+3543. This is an extremely dense core and is not usually found. A recent molecular study of IRAS 05358+3543 by Yamada et al. (2022) found evidence for two colliding molecular clouds at several pc scales, which formed a dense filament including the IRAS 05358+3543 core. The study of IRAS 05358+3543 supports the idea that the formation of high-mass stars requires strong compression by an external trigger, such as the collision of molecular clouds. The duration of the collision must be longer than the free-fall time, calculated based on the mean density in the shock-compressed layer, in order to create the high column density necessary for star formation. This highlights the importance of external triggers and the duration of the trigger in the formation of high-mass stars.

In this chapter, we study the correlation between the shock duration and resulting star formation by controlling the amount of gas that flows into the numerical domain to examine the effect of shock duration and the origin of threshold peak column density of massive cluster formation. In previous related studies, there have been discrepancies in conclusions. Inoue et al. (2018) and Abe et al. (2021) demonstrated that fast MHD shock compression allows for the formation of massive cores/stars by numerically setting long-lasting shock compression. These studies assumed a long/infinite duration of a shock wave. On the other hand, Takahira et al. (2014) and Sakre et al. (2022), considered collisions of relatively small clouds and concluded that the fast shock compression prevents the formation of gravitationally bound cores. To clarify this contradictory situation, we examine the effect of shock duration on the resulting massive core/star formation. This paper is organized as follows: In §2, we provide the setup of our simulations, and we demonstrated and interpreted the results in §3. In §4, we discussed the peak column density in the shock-compressed layer by developing a simple theoretical model. Finally, we summarize the results in §5.

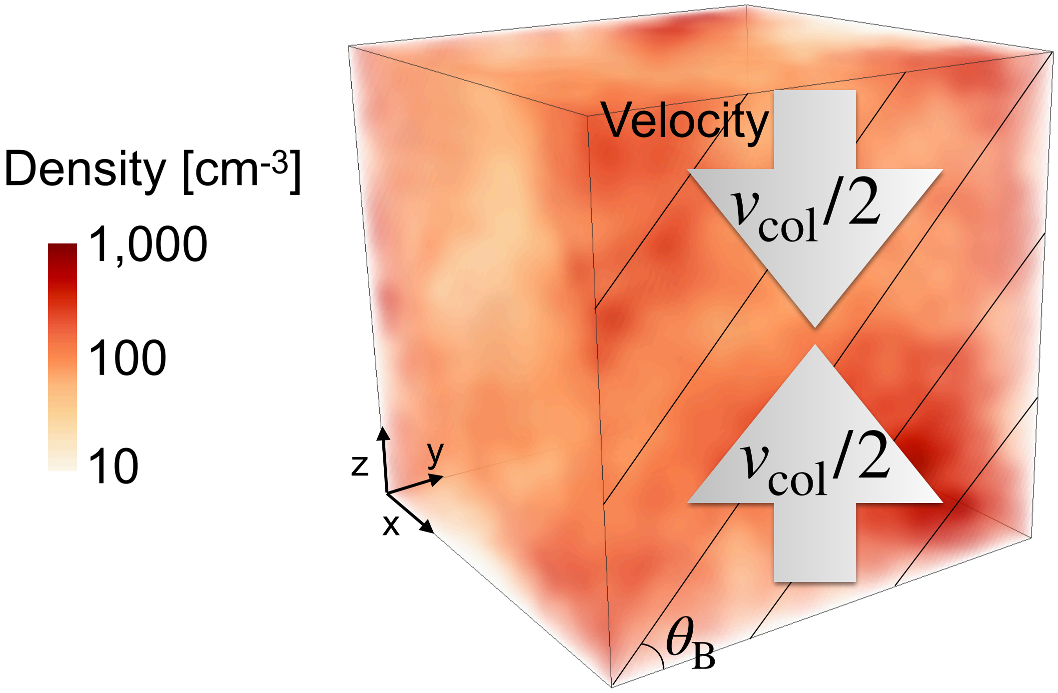

Figure 3.1: Schematic of the initial condition. The color bar represents the density magnitude, the black lines represent the initial magnetic field lines, the $\theta_{\rm B}$ represents the angle between the y-axis and the initial magnetic field lines, and the gray arrows represent the orientations of the converging flows.

3.2 Setup for simulations

We perform three-dimensional (3D) isothermal[1] MHD simulations including self-gravity using SFUMATO code (Matsumoto, 2007). The initial condition is the same as that of Abe et al. (2021) except that we additionally introduce a finite duration of shock compression. In this section, the numerical setup is briefly stated. We use a cubic numerical domain with a box size of $L_{\rm box} = 6$ pc, which is filled with a nonuniform gas, a mean density n_0, and fluctuations with a power spectrum of $(\log\rho)^2_{\rm k} \propto k^{-4}$ due to supersonic turbulence (Larson, 1981; Beresnyak et al., 2005; Elmegreen & Scalo, 2004; Scalo & Elmegreen, 2004; Heyer & Brunt, 2004). We set the gas temperature to 10 K (corresponding sound speed $c_{\rm s} \sim 0.2$ km/s). We divide the numerical domain into uniform 512^3 cells, resulting in a spatial resolution of $\Delta x = 6$ pc/512 $= 1.2 \times 10^{-2}$ pc. The initial velocity field is set to, $\mathbf{v}(x, y, z) = \mathbf{v}_{\rm turb}(x, y, z) - (v_{\rm col}/2)\tanh[(z - L_{\rm box}/2)/0.1]\hat{\mathbf{z}}$, where $\mathbf{v}_{\rm turb}$ is

---

[1] Isothermal treatment is a good approximation for describing compression. However, it might not be a good approximation for the expansion regions, which are created after $t_{\rm dur}$. The minimum density in the expansion region can be as small as 1 cm^{-3}. In such regions, the low-density gas would become atomic and warm. One of the non-isothermal effects imposed on the cold gas surrounded by the warm gas is an evaporation flow due to gas heating and thermal conduction, and the flow speed is known to be subsonic (Inoue et al., 2006). Thus, the non-isothermal effect would not be substantial because the expansion goes on at sonic speed owing to pressure reduction.

the turbulent velocity, having a dispersion of 1.0 km s^{-1} with a power spectrum of $v_{\rm k}^2 \propto k^{-4}$, following Larson's law (Larson, 1981). This initial velocity leads to a gas collision at $z = L_{\rm box}/2$ plane. We select an initial magnetic field strength $B_0 = 10$ μG (Heiles & Crutcher, 2005; Crutcher, 2012) and an angle $\theta_{\rm B}$ to the y-z plane 45°, or 60°.

The velocity fields at z-boundaries are given by

$$\mathbf{v}^{\pm}_{\rm boundary}(x, y) = [\pm v_{\rm col}/2\hat{\mathbf{z}} + \mathbf{v}_{\rm turb}(x, y, z)] \exp[-(t - t_{\rm stop})/0.1{\rm Myr}], \tag{3.1}$$

where "$\mathbf{v}^{+}_{\rm boundary}$" and "$\mathbf{v}^{-}_{\rm boundary}$" are the velocity field at $z = 0$, and 6 pc, respectively, and "$v_{\rm col}$" is the relative velocity of two flows colliding at $z = 3$ pc. These boundary conditions realize the cessation of gas inflows around $t = t_{\rm stop}$, and their implementation differs significantly from that of Abe et al. (2021). The density/turbulence field to be inflow from the boundary is the same density/turbulence spatial distribution as the initial condition. We impose free boundary conditions on the magnetic field at $z = 0, L_{\rm box}$ boundaries. We use periodic boundary conditions for all physical variables for $x = 0$, $L_{\rm box}$ and $y = 0$, and $L_{\rm box}$ boundary planes.

We simulate 18 different models. Each model has a unique name, starting with "v" (for "velocity of collision"), followed by the collision velocity ("3," "5," "14," and "18", "24" [km s^{-1}]) and, the shock duration ("t"), followed by the time scale ("0.23–1.9" [Myr]). Models with a different initial magnetic field angle and initial mean density are additionally denoted as "ang60" and "d300" corresponding to $\theta_{\rm B} = 60°$ and $\bar{n}_0 = 300$ cm^{-3}, respectively. The set of parameters used in our simulations is listed in Table 3.1.

In the regions where gravitational collapse occurs, we introduce the sink particle (Matsumoto et al., 2015; Inoue et al., 2018). The conditions for generating the sink particles depend on the resolution. The threshold density of sink particle generation in the current simulations with 512^3 cells is 5.6×10^4cm^{-3}, which is lower than that in previous studies. Thus, we perform an AMR simulation to demonstrate whether the results depend on the resolution and threshold density of the sink creation. The Jeans criterion is used for the refinement (Truelove et al., 1997): $\Delta x \leq \lambda_{\rm J}/8$ (where $\lambda_{\rm J} = \pi^{1/2} c_{\rm s}/\sqrt{G\rho}$ is the Jeans length), and the minimum cell size for the AMR run is $\Delta x = 6$ pc/1024=5.9 $\times10^{-3}$ pc. The threshold density of sink particles is 2.2×10^5cm^{-3}. The results are almost the same as those in the non-AMR run, as shown in §3.

3.3 Results

3.3.1 Column Density Maps

Short Duration Case

Figure 3.2 shows snapshots of the column density map of model v24t0.23 at t = 0.10, 0.20, 0.30, and 0.60 Myr. Panels (a)–(d) and (a')–(d') show snapshots in the y-z and x-y plane slices, respectively. The formation of dense filaments

Table 3.1: Model parameters.

Model Name	$v_{\rm coll}$ [km s^{-1}]	$v_{\rm sh}$ [km s^{-1}]	$t_{\rm stop}$ [Myr]	$t_{\rm dur}$ [Myr]	$\theta_{\rm B}$	$\bar{n}_0$ [cm^{-3}]	Δx [pc]
v3t1.4	3	2.2	0.0	1.4	45°	100	1.2×10^{-2}
v5t0.94	5	3.2	0.0	0.94	45°	100	1.2×10^{-2}
v5t1.5	5	3.2	0.7	1.5	45°	100	1.2×10^{-2}
v14t0.39	14	7.7	0.0	0.39	45°	100	1.2×10^{-2}
v14t0.40ang60	14	7.5	0.0	0.40	60°	100	1.2×10^{-2}
v14t0.66	14	7.7	0.3	0.66	45°	100	1.2×10^{-2}
v14t0.84	14	7.7	0.5	0.84	45°	100	1.2×10^{-2}
v14t1.0	14	7.7	0.7	1.0	45°	100	1.2×10^{-2}
v14t1.1d300	14	7.4	0.7	1.1	45°	300	1.2×10^{-2}
v14t1.5	14	7.7	1.2	1.5	45°	100	1.2×10^{-2}
v14t1.7ang60	14	7.5	1.4	1.7	60°	100	1.2×10^{-2}
v14t1.9	14	7.7	1.7	1.9	45°	100	1.2×10^{-2}
v18t0.68	18	9.7	0.4	0.68	45°	100	1.2×10^{-2}
v24t0.23	24	13	0.0	0.23	45°	100	1.2×10^{-2}
v24t0.43	24	13	0.2	0.43	45°	100	1.2×10^{-2}
v24t0.61	24	13	0.4	0.61	45°	100	1.2×10^{-2}
v24t1.6	24	13	1.4	1.6	45°	100	1.2×10^{-2}
v24t1.6AMR	24	13	1.4	1.6	45°	100	5.9×10^{-3}
v24t1.8	24	13	1.7	1.8	45°	100	1.2×10^{-2}

is shown in panels (a')–(d'). Recently, Abe et al. (2021) classified the filament formation mechanisms into several categories. According to their classification, the type of filament formation seen in the results of model v24t0.23 is type O (the oblique MHD shock compression mechanism). Note that type O filamentation works behind a strong shock of $v_{\rm sh} \gtrsim 5$ km s^{-1}, and the shock waves created in this model have $v_{\rm sh}$ of approximately 13 km s^{-1}. The evolution of the mass of the dense gas in the numerical domain is shown in panel (a) of Figure 3.3. The blue, red, and green points represent the gas masses of the regions with densities greater than 10^3, 10^4, and 10^5 cm^{-3}, respectively. Panels (b')–(d') in Figure 3.2 and panel (a) in Figure 3.3 show that the mass of the dense gas decreases 0.2–0.3 Myr. This evolution is due to the expansion of the shock-compressed layer and the resulting pressure reduction (see Figure 3.2d), which deconfines dense filaments. The time at which the compression layer starts to expand $t_{\rm dur}$ can be written using $t_{\rm stop}$ as

$$t_{\rm dur} \simeq t_{\rm stop} + \frac{L_{\rm box}/2 - v_1 t_{\rm dur}}{v_{\rm col}/2} \tag{3.2}$$

$$\simeq \frac{t_{\rm stop} + L_{\rm box}/v_{\rm col}}{1+\sqrt{2}v_{\rm alf,0}/v_{\rm col}}. \tag{3.3}$$

where $v_1 \simeq \bar{v}_{\rm Alf,\perp}/\sqrt{2}$ is the shock velocity at the rest frame of the compression layer, and $\bar{v}_{\rm Alf,\perp} = B_{0,\perp}/\sqrt{4\pi\bar{\rho}_0}$ is the mean Alfvén velocity. $B_{0,\perp} = B_0\cos(\theta_{\rm B})$ is the initial magnetic field strength perpendicular to the shock normal. The second term on the right-hand side of Eq. (3.2) represents a retarded time for the gas to reach the compression layer after t_{stop}. In the case of model v24t0.23, $t_{\mathrm{dur}} \simeq 0.23$ Myr corresponds to the time when the dense gas mass in Figure 3.3 reaches its peak.

The free-fall time in the postshock layer, which gives the timescale for self-gravitating sheet fragmentation (Nagai et al., 1998), can be estimated as

$$\begin{aligned} t_{\mathrm{ff}} &= \sqrt{\frac{1}{2\pi G\bar{\rho}_1}} \\ &= \sqrt{\frac{\bar{v}_{\mathrm{Alf},\perp}}{2\sqrt{2}\pi G\bar{\rho}_0\bar{v}_{\mathrm{sh}}}} \\ &= \sqrt{\frac{B_{0,\perp}}{4\sqrt{2}\pi^{3/2}G\bar{\rho}_0^{3/2}\left(v_{\mathrm{coll}}/2 + B_0/\sqrt{8\pi\bar{\rho}_0}\right)}} \\ &\simeq 1.0\ \mathrm{Myr}\left(\frac{B_{0,\perp}}{10\ \mu\mathrm{G}}\right)^{1/2}\left(\frac{\bar{n}_0}{100\ \mathrm{cm}^{-3}}\right)^{-3/4} \\ &\times \left[\left(\frac{v_{\mathrm{coll}}}{12\ \mathrm{km/s}}\right) + 0.17\left(\frac{B_{0,\perp}}{10\ \mu\mathrm{G}}\right)\left(\frac{\bar{n}_0}{100\ \mathrm{cm}^{-3}}\right)^{-1/2}\right]^{-1/2}, \end{aligned} \tag{3.4}$$

where $\bar{\rho}_1 \simeq \sqrt{2}\mathcal{M}_{\mathrm{A}}\bar{\rho}_0$ is the mean density of the shocked layer (e.g., Inoue & Fukui, 2013), and $\bar{v}_{\mathrm{sh}} = v_{\mathrm{coll}}/2 + v_1 \simeq v_{\mathrm{coll}}/2 + B_0/\sqrt{8\pi\bar{\rho}_0}$ represents the mean shock velocity. Because $t_{\mathrm{dur}} < t_{\mathrm{ff}} \simeq 0.68$ Myr in model v24t0.23, the shock compression layer expands before gravitational fragmentation and no sink particles are created.

Long Duration Case

Similar to Figure 3.2, Figure 3.4 shows snapshots of the column density map of model v24t1.6 at t = 0.30, 0.80, 1.60, and 1.80 Myr. Because the shock velocity is the same as in the previous model (v24t0.23), dense filamentary structures are created via the type O mechanism. The "+" symbols in Figure 3.4 indicate the positions of the sink particles. The evolution of the dense gas mass in the numerical domain is shown in panel (b) of Figure 3.3. The blue, red, and green points represent the masses of the regions with densities greater than 10^3, 10^4, and 10^5 cm^{-3}, respectively, as in panel (a). It should be noted that the range of the vertical axis is different from that of the panel (a). In this model also, the shock-compressed layer expands after $t = t_{\mathrm{dur}} \simeq 1.6$ Myr, as in model v24t0.23. However, the duration of the compression is longer than the free-fall-time calculated using the mean density in the layer $t_{\mathrm{ff}} \simeq 0.58$ Myr (Eq. 2.5), allowing the filaments to coalesce because of the gravitational contraction of the compression layer. Therefore, in contrast to model v24t0.23, the dense gas mass continues to increase even after t_{dur} (panel a in Figure 3.3).

3.3.2 Peak Column Density vs. Dense Gas Mass

Observations show that the peak column density of a star-forming cloud correlates with the number of OB stars in the system (Enokiya et al., 2021). Here, we compare the results of our simulations with the observed results. We consider the following two types of mass in the numerical domain, as a proxy of star formation: the total mass of sink particle, $M_{\rm sink,tot}(t)$, and total gas mass in the region with $A_V > 8$ mag. ($N_{\rm H_2} \simeq 7.8\times10^{21}$ cm^{-2}), $M_{\rm Av8}(t)$ (Lada et al., 2010). The sum of these masses $M_{\rm dense}(t) \equiv M_{\rm sink,tot}(t) + M_{\rm Av8}(t)$, is proportional to the total mass of stars in the system. Figure 3.5 shows the evolution of $M_{\rm dense}(t)$. Panels (a) and (b) show the results for models v24t0.23 and v24t1.6, respectively. In our simulation, the $M_{\rm dense}(t)$ saturates in late time, and we can define a mass associated with star formation. By fitting the $M_{\rm dense}(t)$ using a trial function $\alpha \tanh[2\pi(t-t_0)/t_{\rm w}] + \beta$, as shown in the red lines in Figure 3.5, we obtain the time $t_{\rm sat} \equiv t_0 + t_{\rm w}/4$ (dashed lines in Figure 3.5) at which we measure total dense gas mass representing the star formation activity in the system, where $\alpha, t_0, t_{\rm w}, \beta$ are fitting parameters. Note that $t_{\rm sat}$ corresponds to the time when the fitting curve reaches approximately $\alpha \tanh[2\pi(t_{\rm sat} - t_0)/t_{\rm w}] + \beta = \tanh(\pi/2) + \beta \simeq 0.92\alpha + \beta$, i.e., this value means mass corresponding to $(0.92{+}1.0)\times\ 100/2 = 96$ [%] of the increment in the trial function.

Generally, a peak column density highly depends on a spatial grid (or in other words, spatial resolution) used for the derivation. Thus, the observed peak column densities of cloud-cloud collision (CCC) candidates in the plots of Figure 9 in Enokiya et al. (2021) have potentially independent spatial resolutions. Nevertheless, the correlation between the peak column density and the number of O- and B-type stars is apparent in the plots. This suggests that the spatial resolutions are similar among the observed CCC candidates. We have checked the spatial resolution among the CCC candidates and found it roughly $\sim$ the size of the smaller cloud/10. Assuming 5 pc for the size of the smaller cloud (see Figure 9 in Fukui et al., 2021), we estimate the typical spatial resolution of the observed CCC candidates to be 0.5 pc. Thus, before computing the peak column density of the system, we take a smoothing of the column density structure using the Gaussian kernel function of a width of 0.5 pc. In panel (a) of Figure 3.6, we demonstrated the scatter plot of the peak column density vs. the dense gas mass $M_{\rm dense}(t_{\rm sat})$ for all runs listed in Table 2.1. The color of the points indicates $t_{\rm dur}/t_{\rm ff}$, which represents the influence of self-gravity. We employ the following procedures to estimate the number of OB stars formed in the numerical system: We multiply $M_{\rm dense}(t_{\rm sat})$ by the star formation efficiency $\mathrm{SFE_{dense}} \sim 0.1$ to obtain the total mass of stars (Fukui et al., 2021). The fraction of OB-type stars in the total stellar mass $f_{\rm OB} = \left(\int_{10M_\odot}^{150M_\odot} dM\ MF_{\rm Kroupa}\right) / \left(\int_{0.01M_\odot}^{150M_\odot} dM\ MF_{\rm Kroupa}\right) = 0.19$ is then multiplied to obtain the total mass of OB stars expected in the system. Note that we consider stars heavier than the early-B type, i.e., larger than approximately 10 $M_\odot$. Here, $F_{\rm Kroupa} \equiv dN/dM$ is an IMF proposed by Kroupa (2001). Therefore, the estimation of the number of OB stars is

$$N_{\rm OB} \simeq M_{\rm dense}(t_{\rm sat}) \times \mathrm{SFE_{dense}} \times f_{\rm OB} \times \left(\frac{\int_{10M_\odot}^{150M_\odot} dM\ MF_{\rm Kroupa}}{\int_{10M_\odot}^{150M_\odot} dM\ F_{\rm Kroupa}} \right)^{-1}, \quad (3.5)$$

where $\int_{10M_\odot}^{150M_\odot} dM\ MF_{\rm Kroupa} / \int_{10M_\odot}^{150M_\odot} dM\ F_{\rm Kroupa}$ on the right-hand side is the typical mass of OB stars. Panel (b) in Figure 3.6 is compiled from panel (a) using Eq. (3.5). The result shows a correlation similar to that of Enokiya et al. (2021), although our simulations cover only a limited range of peak column density than the observations. The power-law index obtained by fitting data in panel (b) is 0.75, which agrees well with that of observations 0.73±0.11 (Enokiya et al., 2021). The black line is the fitting line in Figure 9 (b) of Enokiya et al. (2021). It has been known observationally that massive star cluster formation occurs in the clouds with a peak column density greater than $N_{\mathrm{peak}} \geq 10^{23}$ cm^{-2} (Fukui et al., 2016). Our simulations agree with this threshold peak column density (see the region with $N_{\mathrm{peak}} \sim 10^{23}$cm^{-2} in panel (b) of Figure 3.6). The stability parameter, the ratio of the shock duration and the free-fall time of the compressed layer $t_{\mathrm{dur}}/t_{\mathrm{ff}}$, indicates that massive stars are expected to be formed where the dense shock-compressed layer is kept over the free-fall time. We find that when the N_{peak} exceeds 10^{23} cm^{-2} the stability parameter $\gtrsim 2$. Coincidentally, the threshold peak column density takes a similar value to the threshold column density for fragmentation suppression 1 g cm^{-2} proposed by Krumholz & McKee (2008).

3.3.3 Sink Mass Histogram

Figure 3.7 shows the sink mass histograms at $t = t_{\mathrm{sat}}$ for the models v14t0.38, v14t0.84, and v14t1.9. In our simulations, the sink particles correspond to gravitationally collapsing cores. Note that Figure 3.7 is not a core mass function because low-mass cores are not well resolved in our simulations. a massive sink particle of 355 $M_{\odot}$, and OB-type stars can be formed in the model v14t1.9, which has a long flow duration of $t_{\mathrm{dur}}/t_{\mathrm{ff}} \simeq 2.6$. The mass/number of sink particles increases with t_{dur}, as expected, but only the long duration model v14t1.9 has $t_{\mathrm{dur}}/t_{\mathrm{ff}} \gtrsim 2$ and exhibits active massive star formation.

Figure 3.8 shows a sink mass histogram at $t = t_{\mathrm{sat}}$ in the models v24t1.6 and v24t1.6AMR, comparing the results with and without AMR. The number of sink particles with masses $\sim$ 1 $M_{\odot}$ increased because AMR calculation can capture self-gravitational fragmentation of short-wavelength modes in dense filaments. However, the total masses of massive sink particles ($> 10 M_{\odot}$) are almost the same between v24t1.6 ($M_{\mathrm{sink}} = 1803$ $M_{\odot}$) and v24t1.6AMR ($M_{\mathrm{sink}} = 2048$ $M_{\odot}$), indicating that the results exhibited in §3.2 do not change significantly, even if the spatial resolution is improved.

3.4 Discussion

3.4.1 Estimation of Peak Column Density

In §3.3.2, we stated that self-gravitational collapse must achieve a peak column density of 10^{23} cm^{-2}. Given that the column density map obtained from observations is approximately $\sim 500 \times 500$ pixels, the peak column density approximately corresponds to 5σ away from the mean of the PDF obtained from observations. Here, we estimate the peak column density using a theory of the gas density PDF in a turbulent medium, which shows that gravitational collapse in shock-compressed layers is required to achieve a peak column density of 10^{23} cm^{-2}. The PDF of the gas density in a turbulent medium shows log-normal PDF of the form (Passot & Vázquez-Semadeni, 2003; Padoan et al., 2014)

$$p_{\rm s}(s) = \frac{1}{\sqrt{2\pi\sigma_s^2}} \exp\left(-\frac{(s-s_1)^2}{2\sigma_{\rm s}^2}\right). \tag{3.6}$$

where $s \equiv \ln(\rho/\rho_1)$, ρ_1 and s_1 represent the mean density and mean logarithmic density in the shocked layer, respectively. The latter is related to the standard deviation $\sigma_{\rm s}$ as $s_1 = -\sigma_{\rm s}^2/2$. Molina et al. (2012) find that the standard deviation $\sigma_{\rm s}$ is determined using the turbulence Mach number $\mathcal{M}$, plasma beta β, and the ratio of solenoidal mode to compressive mode b (pure solenoidal forcing gives b=1/3 and pure compressive forcing gives b=1) as

$$\sigma_{\rm s}^2 = \ln\left(1 + b^2\mathcal{M}^2\frac{\beta}{\beta+1}\right). \tag{3.7}$$

Here, we estimate the maximum possible column density of a cloud formed by the gas collision. The density PDF can have maximum width if we substitute the collision velocity for the turbulence velocity dispersion

$$\mathcal{M}_{\rm max} \equiv v_{\rm col}/(2c_{\rm s}). \tag{3.8}$$

The beta of the shock-compressed layer is given by the shock jump condition of the isothermal MHD as

$$\beta_{\rm sh} = \frac{8\pi\rho_1 c_s^2}{B_1^2} \simeq \frac{8\pi\rho_0 c_s^2}{\sqrt{2}\mathcal{M}_{\rm A,max}B_0^2}, \tag{3.9}$$

where $\rho_1 \simeq \sqrt{2}\mathcal{M}_{\rm A,max}\rho_0$, $B_1 \simeq \sqrt{2}\mathcal{M}_{\rm A,max}B_0$, and $\mathcal{M}_{\rm A,max} = v_{\rm col}/(2v_{\rm alf,0})$ are the density, magnetic field in the compression layer, and the Alfvén Mach number of the shock. If we use the parameter b=0.4, which is expected in the shock-compressed layer (Kobayashi et al., 2022), then we can determine $\sigma_{\rm s,max}$ and density PDF.

Numerical experiments of supersonic isothermal turbulence and observations (Goodman et al., 2009) show that the PDF of column density is also close to log-normal (Federrath et al., 2010)

$$p_\eta(\eta) = \frac{1}{\sqrt{2\pi\sigma_\eta^2}} \exp\left(-\frac{(\eta-\eta_1)^2}{2\sigma_\eta^2}\right), \tag{3.10}$$

where $\eta \equiv \ln(N/N_1)$. N and N_1 are column density and the mean column density, respectively. By comparing s_1 and η_1 in numerical simulations by Federrath et al. (2010), η_1 is approximately expressed as $\eta_1 \sim 0.5s_1$. The standard deviation is also approximated by $\sigma_\eta \sim 0.5\sigma_{\rm s}$. These relationships can be used to convert density PDF to column-density PDF.

The peak column density is defined as 5σ away from the mean

$$N_{5\sigma} \equiv \exp(\eta_1 + 5\sigma_{\eta,\mathrm{max}})N_1, \tag{3.11}$$

where $\sigma_{\eta,\mathrm{max}} \equiv 0.5\sigma_{\mathrm{max}}$. Substituting the strong collision case parameters (v_{col} = 10 km s^{-1}, $\bar{n}0 = 100\ \mathrm{cm}^{-3}$, and $B_0 = 10\ \mu\mathrm{G}$), yields a peak column density of $N5\sigma$ = $8.7\times10^{22}\ \mathrm{cm}^{-2}$, which is less than $10^{23}\ \mathrm{cm}^{-2}$. Therefore, even if the velocity dispersion of the turbulence in the shock-compressed layer is overestimated, the peak column density of the structure created solely by turbulence is not expected to exceed $10^{23}\ \mathrm{cm}^{-2}$, indicating that gravitational collapse of the shock layer is necessary to reach this value. In other words, the shock-compressed layer must be sustained until gravitational collapse is triggered, resulting in the formation of a massive star cluster that can increase the peak column density.

3.4.2 Which is advantageous for massive star formation, fast or slow collisions?

According to the recent study by Sakre et al. (2022), there is a maximum collision speed for triggering star formation by a cloud collision for a given initial cloud. This is consistent with the findings of other studies, as high collision speed can lead to a short shock duration. However, it doesn't necessarily mean that a high shock velocity is negative for induced star formation. As we discuss below, the high shock velocity is generally positive for star formation: The duration of the shock is estimated by $t_{\mathrm{dur}} = L/v_{\mathrm{sh}}$, where L is the spatial scale and v_{sh} is the typical velocity of the flows. If we suppose supersonic turbulent gas flow collision as an origin of the shock, Larson's law gives $v_{\mathrm{sh}} \propto L^{0.5}$ or $L \propto v_{\mathrm{sh}}^2$, and then, $t_{\mathrm{dur}} = L/v_{\mathrm{sh}} \propto v_{\mathrm{sh}}$. Since the average free-fall time of the shocked layer is $t_{\mathrm{ff}} \propto v_{\mathrm{sh}}^{-1/2}$ from Eq. (2.5), the ratio of the shock duration and the postshock free-fall time is written as $t_{\mathrm{dur}}/t_{\mathrm{ff}} \propto v_{\mathrm{sh}}^{3/2}$. This indicates that faster shock leads to a longer duration in units of the free-fall time, i.e., larger clouds naturally lead to more active star formation. In contrast, if we fix the scale of the flow L and use a different scaling $t_{\mathrm{dur}} = L/v_{\mathrm{sh}} \propto v_{\mathrm{sh}}^{-1}$, we obtain an opposite result $t_{\mathrm{dur}}/t_{\mathrm{ff}} \propto v_{\mathrm{sh}}^{-1/2}$. Thus, under the fixed cloud scale, faster shock leads to a negative effect on star formation, but we should bear in mind that this is due to artificially fixed L and not a general trend.

3.5 Summary

We performed simulations of the shock compression of molecular clouds using the SFUMATO, a 3D isothermal magnetohydrodynamic code that includes self-gravity. The impact of the shock-compressed layer's duration on filament and star formation was studied by making the shock duration a controlled variable. We analyzed the correlation between the peak column density and the estimated number of OB-type stars to gain insight into the initial conditions for the formation of massive stars and compared our findings with the observations reported by Enokiya et al. (2021). Our main conclusions are as follows.

1. The formation of filaments behind the shock in the short-duration model is followed by expansion/evaporation after the shock duration timescale, while the long-duration model results in the formation of massive filaments leading to star formation.

2. If the observed peak column density exceeds 10^{23} cm^{-2}, then the number of OB stars expected to be formed in the shock-compressed layer can reach the order of ten, which is indicative of massive cluster formation. This is consistent with the findings of Enokiya et al. (2021), as shown in the region with $N_{\rm peak} \sim 10^{23}{\rm cm}^{-2}$ in panel (b) of Figure 3.6. A simple theoretical model indicates that achieving such a high peak column density is possible only when the shock-compressed layer undergoes gravitational collapse.

3. The duration of shock compression must be at least two free-fall times in the compressed layer ($t_{\rm dur}/t_{\rm ff} \gtrsim 2$) for massive star formation to be activated, and this conclusion is not significantly influenced by spatial resolution.

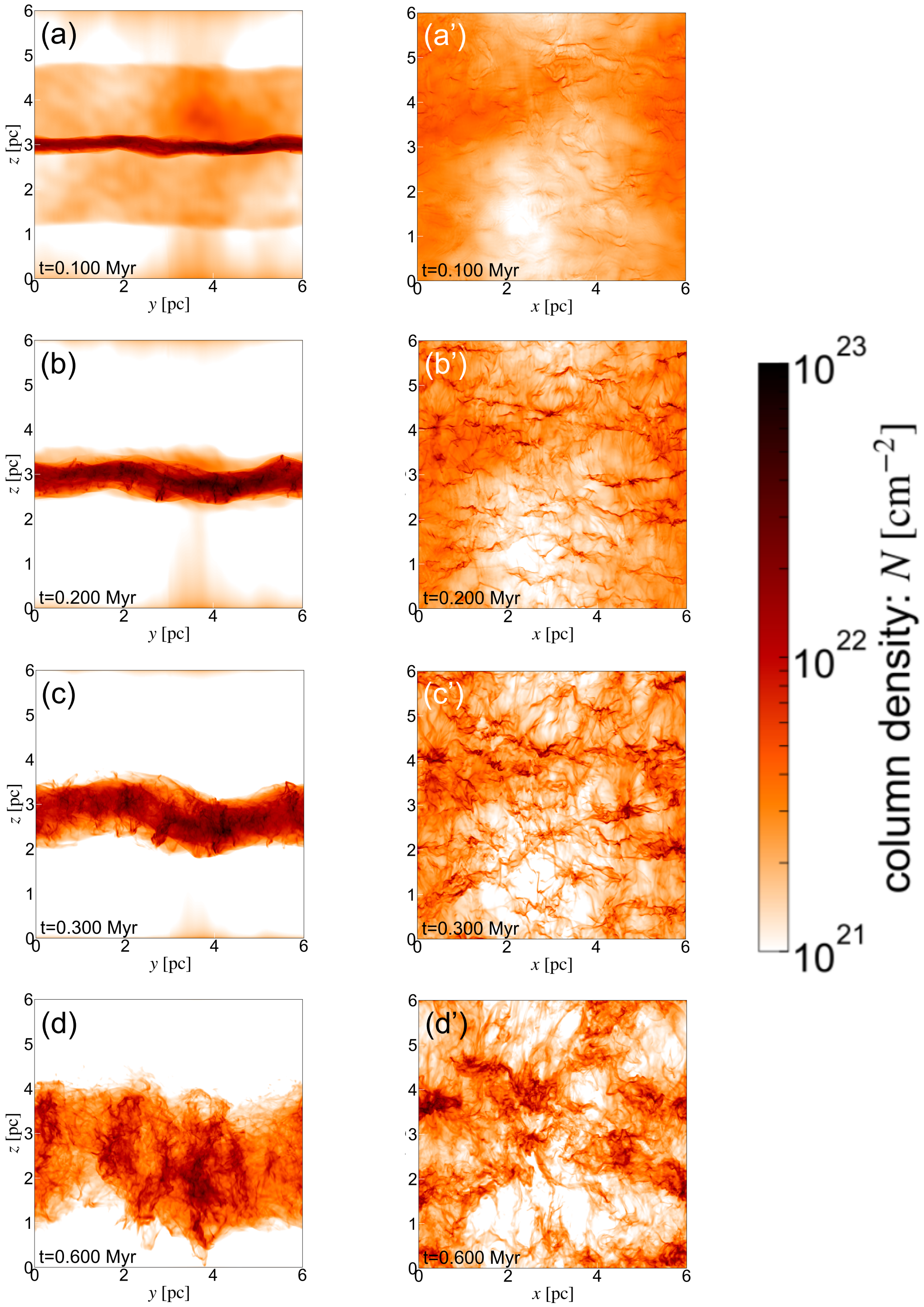

Figure 3.2: Column density maps of the result of model v24t0.23 at time $t = 0.3$, 0.8, 1.6, and 1.8 Myr (from top to bottom). *Left row* (panels a, b, c, and d): y-z plane column densities. *Right row* (panels a', b', c', and d'): x-y plane column densities.

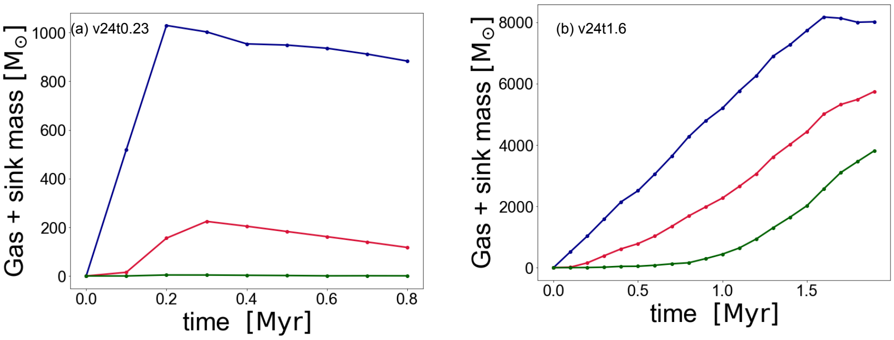

Figure 3.3: Panel a: the evolution of the total dense gas mass in the model v24t0.23. The blue, red, and green points represent the total masses with densities above 10^3, 10^4, and 10^5 cm^{-3}, respectively. Panel b: the same as panel (a), but for model v24t1.6.

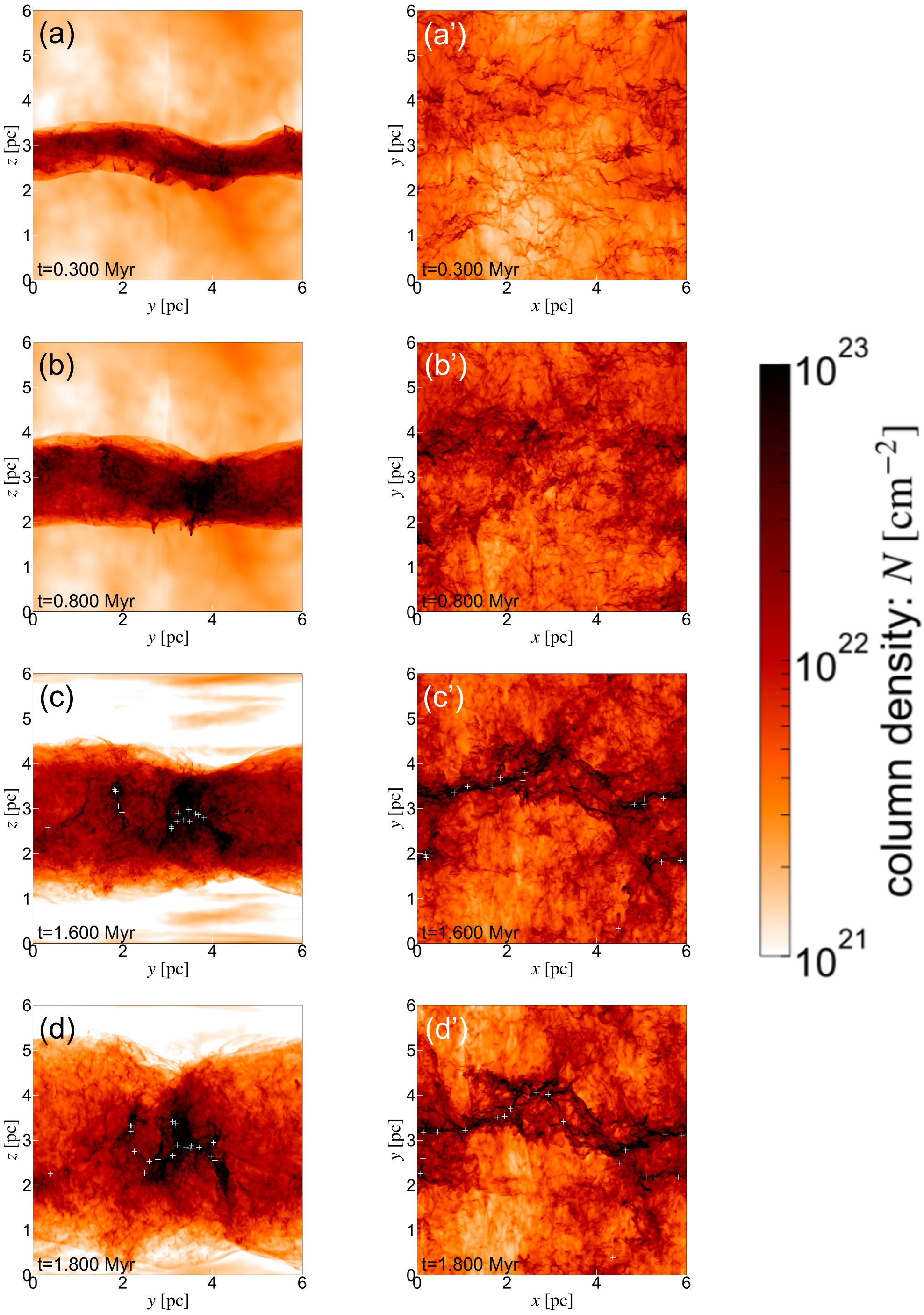

Figure 3.4: Column density maps in the result of model v24t1.6 at time t = 0.3, 0.8, 1.6, and 1.8 Myr (from top to bottom). *Left row* (panels a, b, c, and d): y-z plane column densities. *Right row* (panels a', b', c', and d'): x-y plane column densities.

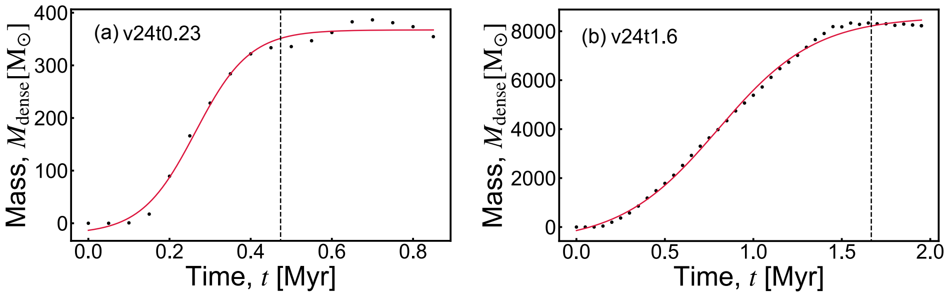

Figure 3.5: Evolution of $M_{\mathrm{dense}}(t)$, which is the sum of the total mass of sink particles ($M_{\mathrm{sink,tot}}(t)$) and the mass of gas with column density larger than 7.8×10^{21} cm^{-2} ($M_{\mathrm{Av8}}(t)$) for the simulation results of models v24t0.23 (left) and v24t1.6 (right). A red line represents the fitting curve obtained using a trial function $\alpha \tanh[2\pi(t - t_0)/t_{\mathrm{w}}] + \beta$, where $\alpha, t_0, t_{\mathrm{w}}, \beta$ are fitting parameters. The dashed line denotes the time t_{sat}, which is defined as the time at which the total gas mass associated with star formation is measured.

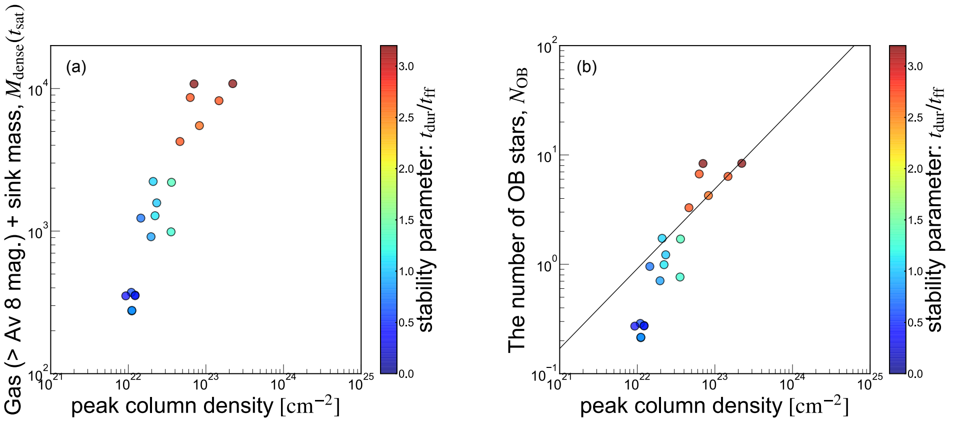

Figure 3.6: Panel a: Scatter plot of the peak column density vs. the dense gas mass $M_{\mathrm{dense}}(t_{\mathrm{sat}})$ for all runs summarized in Table 2.1. Before computing the peak column density of the system, we take a smoothing of the column density using the Gaussian kernel function of a width of 0.5 pc, corresponding to the typical beam width for massive star-forming regions. The color of the points represents $t_{\mathrm{dur}}/t_{\mathrm{ff}}$ indicating the influence of self-gravity. Panel b: Scatter plot of the peak column density vs. the estimated number of OB-type stars N_{OB}. N_{OB} is estimated using Eq. (3.5). The black line is the fitting line in Figure 9 (b) of Enokiya et al. (2021).

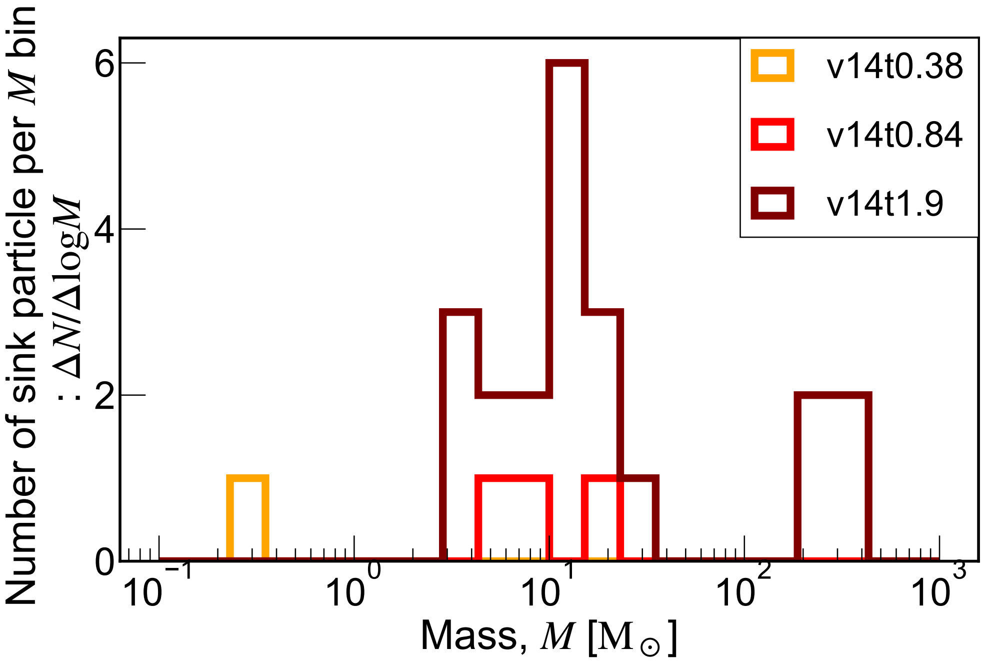

Figure 3.7: Sink mass histogram at $t = t_{\rm sat}$ in the results of models v14t0.38 (orange), v14t0.84 (red), and v141.9 (brown).

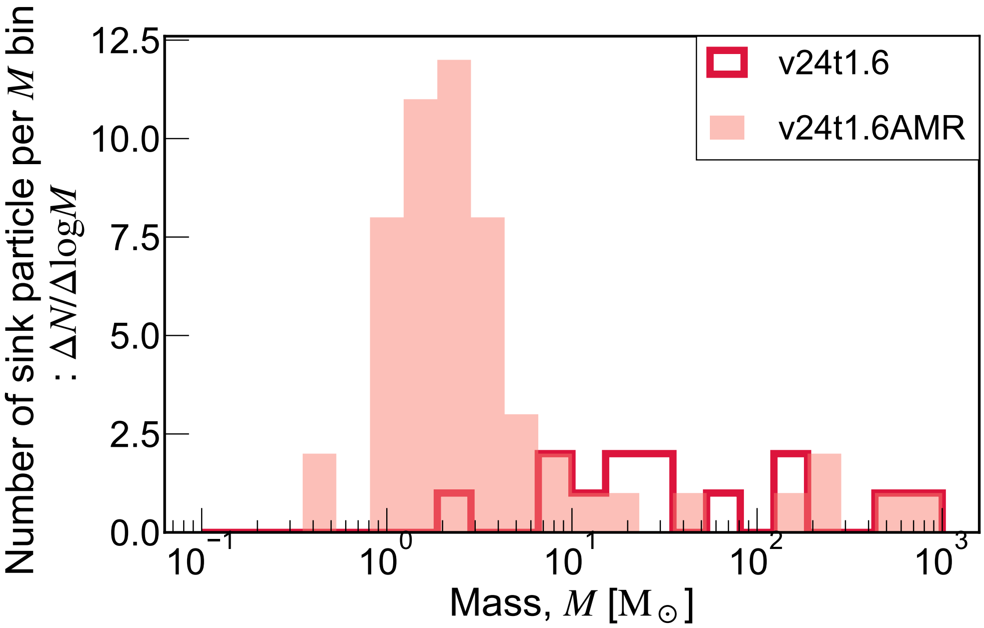

Figure 3.8: Sink mass histogram at $t = t_{\rm sat}$ in the models v24t1.6 (red) and v24t1.6AMR. (filled-in region)

Chapter 4

Filament Evolution Process

4.1 Short Introduction

Type G, C, and O are the fundamental formation mechanisms of supercritical filaments, which are essential for star formation. The common feature of these mechanisms is that filaments are formed by gas flow along the local magnetic-field line in a shocked-compressed sheet. Molecular emission-line observations provide evidence of the perpendicular accretion onto filaments (Palmeirim et al., 2013; Shimajiri et al., 2019; Chen et al., 2020). In particular, Shimajiri et al. (2019) reported the occurrence of accretion onto filaments in a shocked sheet. The accretion rate $\dot{M}_{\rm line}$ is estimated in the range from a few 10 to a few 100 $M_\odot$ Myr^{-1} pc^{-1} (Palmeirim et al., 2013; Bonne et al., 2020). The accretion timescale $t_{\rm acc} \equiv M_{\rm line}/\dot{M}_{\rm line}$ is comparable to self-gravitational fragmentation time-scale in filaments, implying that accretion is essential for the evolution of filaments.

The filament width is one of the significant quantities to determine the initial condition for star formation. The critical line mass considering magnetic support depends on the width of a filament (Tomisaka, 2014). According to linear theory, the self-gravitational fragmentation length scale of the filament depends on the filament width (Stodólkiewicz, 1963; Inutsuka & Miyama, 1992a). Arzoumanian et al. (2018) revealed that the characteristic width of *Herschel* Gould Belt filaments is 0.1 pc (see also Koch & Rosolowsky, 2015), and similar results have been reported by C^{18}O line-emission observations (Orkisz et al., 2019; Suri et al., 2019). Remarkably, the filaments maintain their width, regardless of their line-mass exceeding 100 $M_\odot$ pc^{-1}. If we consider only thermal support against gravity, such a high-line-mass structure cannot maintain a length scale of 0.1 pc. Several authors studied the effects of turbulence and/or magnetic field and have shown that sub-critical and mildly super-critical filaments have a width of 0.1 pc (Fischera & Martin, 2012; Auddy et al., 2016; Priestley & Whitworth, 2022; Federrath, 2016; Ntormousi & Hennebelle, 2019), however, the reason for the constant width of filaments, especially for massive filaments, remains as a mystery. We need to understand the origin of the universal width, especially for massive filaments, by examining the detailed process of gas accretion flows onto the filament.

Given that massive filaments are formed in the post-shock layer threaded by the strong magnetic field, the filament surface is naturally bound by the slow shocks. This unphysical feature stems from the ideal approximation and the resulting discontinuous treatment of the shock. To know the physical scale length of the SSI, we consider a non-ideal effect. Since the corrugation of the shock front generally produces turbulent flows behind the shock (e.g., Inoue et al., 2012; Inoue & Inutsuka, 2012b), we can expect that the SSI will deposit additional energy to the filament.

In molecular clouds, ambipolar diffusion is effective and potentially modifies the SSI dynamics. The Reynolds number of the ambipolar diffusion is given as

$$\mathcal{R}_{\rm AD} = \frac{4\pi\gamma\rho_{\rm n}\rho_{\rm i}v\ell}{B^2}, \tag{4.1}$$

where, $\gamma_{\rm in} \equiv \langle\sigma_{\rm in}v_{\rm in}\rangle/(m+m_{\rm i}) = 3.5\times10^{13}\ {\rm cm^3\ g^{-1}\ s^{-1}}$ and $\rho_{\rm i}$ denotes the ion mass density. $\sigma_{\rm in}$, $v_{\rm in}$, m, and $m_{\rm i}$ represent the Langevin cross-section, the relative velocity between a neutral molecule and ion, mean molecule mass, and mean ion mass, respectively. Assuming a balance between the ionization by cosmic rays and the recombination, $\rho_{\rm i}$ can be expressed as $C\rho^{1/2}$. The characteristic length scale below which the effect of ambipolar diffusion becomes non-negligible can be obtained by solving $\mathcal{R}_{\rm AD} = 1$ that yields

$$\ell_{\rm AD} = 0.09\ {\rm pc}\ \left(\frac{B}{30\ \mu{\rm G}}\right)^2 \left(\frac{n}{10^3\ {\rm cm^{-3}}}\right)^{-3/2} \left(\frac{v}{1\ {\rm km/s}}\right)^{-1}, \tag{4.2}$$

which is comparable to the filament width and suggests that the scale obtained using the ambipolar diffusion affects the filament dynamics. In the context of the solar chromosphere, Snow & Hillier (2021) performed two-dimensional two-fluid simulations of SSI for partially ionized gas. They demonstrated that the neutral fluid stabilizes the SSI on a small scale and found new features such as gas accumulation at valleys. However, the situation in their simulations is different from the one in molecular clouds (e.g., ionization degree, ion-neutral collision cross-section, etc.), and they did not study the dispersion relation and the dependence on density and magnetic field. The linear analysis of SSI including ambipolar diffusion is challenging. Our strategy is to directly simulate the SSI including the ambipolar diffusion and the measurement of the growth rate.

As the first step to understanding the effect of SSI on filament width, we study the effect of ambipolar diffusion on the SSI and derive the most unstable scale. In realistic situations, filaments are bound by two shocks. Because the separation of these two shocks is narrow and they are threaded by the same magnetic field lines, we can expect that the two shocks dynamically influence each other. As the second step, we study the effect of interacting two shocks and show that the slow shock instability mediates inhomogeneous postshock flows and can provide additional dynamical pressure to the filament. As the third step, we perform a three-dimensional SSI simulation including self-gravity and ambipolar diffusion, and compare the column density profile and filaments width with observations. We try to explain the origin of the universality of filament width.

4.2 Setup for simulations

We perform two-dimensional ideal/non-ideal MHD simulations using Athena++ code (Stone et al., 2020). We use the second-order accurate van Leer predictor-corrector scheme and piecewise linear method applied to primitive variables to integrating the equations. The constrained transport method (Stone & Gardiner, 2009) ensures the divergence-free condition, $\nabla \cdot \boldsymbol{B} = 0$. In this paper, we do not solve the Poisson equation for self-gravity because we concentrate ourselves on the physics of SSI under the influence of ambipolar diffusion as a first step of this sort of study. The effect of self-gravity will be taken into account in our future studies. We solve the following equations:

$$\frac{\partial \rho}{\partial t} + \nabla \cdot (\rho \boldsymbol{v}) = 0 \tag{4.3}$$

$$\frac{\partial \rho \boldsymbol{v}}{\partial t} + \nabla \cdot \left(\rho \boldsymbol{v}\boldsymbol{v} - \frac{\boldsymbol{B}\boldsymbol{B}}{4\pi} + P^{*}\boldsymbol{I} + \boldsymbol{\Pi} \right) = 0 \tag{4.4}$$

$$\frac{\partial E}{\partial t} + \nabla \cdot \left[(E + P^{*})\,\boldsymbol{v} - \boldsymbol{B}(\boldsymbol{B}\cdot\boldsymbol{v}) + \boldsymbol{\Pi}\cdot\boldsymbol{v} + \frac{\eta_{\rm AD}}{|\boldsymbol{B}|^2}\{\boldsymbol{B}\times(\boldsymbol{J}\times\boldsymbol{B})\}\times\boldsymbol{B} \right] = 0 \tag{4.5}$$

$$\frac{\partial \boldsymbol{B}}{\partial t} - \boldsymbol{\nabla} \times \left[(\boldsymbol{v}\times\boldsymbol{B}) - \frac{\eta_{\rm AD}}{|\boldsymbol{B}|^2}\boldsymbol{B}\times(\boldsymbol{J}\times\boldsymbol{B}) \right] = 0, \tag{4.6}$$

where, $P^{*} = p + B^2/(8\pi)$ and $E = e + \rho v^2/2 + B^2/(8\pi)$ are the total pressure and the total energy density; $\rho, p, \boldsymbol{v}$, and $\boldsymbol{B}$ are the density, pressure, velocity, and magnetic field; and $\boldsymbol{J} = \nabla \times B$ is the current. We introduce the viscous stress tensor

$$\Pi_{ij} = \rho\nu \left(\frac{\partial v_i}{\partial x_j} + \frac{\partial v_j}{\partial x_j} - \frac{2}{3}\delta_{ij}\nabla\cdot v \right) \tag{4.7}$$

to prevent the carbuncle phenomenon (Quirk, 1994; Liou, 2000; Kim et al., 2003) and the growth of a grid scale SSI seeded by the carbuncle instability. ν is the coefficient of physical kinematic viscosity. We adjust ν to stabilize a grid scale (eight meshes) fluctuation. The box size $L_{\rm box}$ and ν are chosen so that the stabilizing scale by ambipolar diffusion is sufficiently smaller than this grid scale. $\eta_{\rm AD}$ is the ambipolar diffusion coefficient, which is given by

$$\eta_{\rm AD} = \frac{B^2}{4\pi\gamma_{\rm in}\rho_{\rm n}\rho_{\rm i}}, \tag{4.8}$$

where, $\gamma_{\rm in} \equiv \langle\sigma_{\rm in}v_{\rm in}\rangle/(m + m_{\rm i}) = 3.5 \times 10^{13}$ cm^3 g^{-1} s^{-1}, $\rho_{\rm n} \simeq \rho$ and $\rho_{\rm i}$ are neutral gas mass density and ion mass density. $\sigma_{\rm in}$, $v_{\rm in}$, m, and $m_{\rm i}$ are Langevin cross-section, the relative velocity between the neutral molecule and ion, mean molecule mass and mean ion mass, respectively. We can write the $\rho_{\rm i}$ as $C\rho^{1/2}$ when ionization by cosmic rays balances recombination. In this study we apply $C = 3 \times 10^{-16}$ cm$^{-3/2}$ g$^{1/2}$ (Shu, 1992).

4.2.1 Initial Condition for One-Shock Cases

We numerically solve Eqs. (4.3)–(4.6) on a two-dimensional domain of the size [-4$L_{\rm box}$, 4$L_{\rm box}$] × [0 pc, $L_{\rm box}$] in the shock rest frame. We choose $L_{\rm box} = 1$ pc for the $\gamma = 5/3$ case, and $L_{\rm box} = 0.2$, 0.25, or 0.5 pc for the $\gamma = 1.01$ case. The initial density, velocity, and pressure field are set to be

$$\rho(x,y) = \rho_0 \left[1 + \frac{r-1}{2}(1 - \tanh[x/0.003L_{\rm box}])\right] + \rho_{\rm p}(x,y), \tag{4.9}$$

$$v_x(x,y) = -v_{x0} \left[1 + \frac{r-1}{2}(1 - \tanh[x/0.003L_{\rm box}])\right]^{-1}, \tag{4.10}$$

and

$$p(x,y) = p_0 \left[1 + \frac{r_{\rm pres}-1}{2}(1 - \tanh(x/0.003L_{\rm box}))\right] \tag{4.11}$$

respectively, where, ρ_0, v_{x0}, and p_0 are the initial density, x-component of velocity, and pressure in the pre-shock region, respectively. We perform simulations for dozens of sets of ρ_0 and v_{x0}. As a seed of the instability, we set the upstream gas sound speed $c_{\rm s}$ as 0.2 km s^{-1} so that the p_0 is given by $p_0 = \rho_0 c_{\rm s}^2/\gamma$. The compression ratio r and the pressure jump $r_{\rm pres}$ are

$$r \equiv \frac{(\gamma+1)\mathcal{M}_{\rm s}^2}{(\gamma-1)\mathcal{M}_{\rm s}^2 + 2}, \tag{4.12}$$

and

$$r_{\rm pres} \equiv \frac{2\gamma\mathcal{M}_{\rm s}^2 - (\gamma-1)}{\gamma+1}. \tag{4.13}$$

As a seed of instability, we introduce density perturbation as follows.

$$\rho_{\rm p} = 10^{-4} \times \rho_0 \cos\left(\frac{2\pi y}{\lambda_{\rm p}}\right) \sin\left(\pi \frac{x - 0.02L_{\rm box}}{0.01L_{\rm box}}\right), \text{ if } 0.005L_{\rm box} \le x \le 0.015L_{\rm box} \tag{4.14}$$

where, $\lambda_{\rm p}$ is the wavelength of the perturbation. These initial conditions lead to a perturbed stationary shock at $x = 0$. Since the star-forming filaments are perpendicular to the magnetic field, we set the initial uniform magnetic field along the x-axis $B_0\hat{x}$. The numerical domain is a 2D box with a uniform grid of 4096 × 512 cells, which leads to a spatial resolution of $\Delta x = L_{\rm box}$ / 512. We impose free boundary conditions at $x = -4L_{\rm box}, 4L_{\rm box}$ boundaries. For the $y = 0, L_{\rm box}$ boundaries, we use periodic boundary conditions.

We simulate 22 different models. Each model has a unique name, starting with "n" (for "upstream density n_0"), followed by the number density ("800," "1000," "1300," and "1600" [cm^{-3}]), the magnetic field ("b"), followed by the field strength ("24," "30," "35," and "40" [μG]), and the velocity ("v"), followed by the upstream velocity ("0.8," "0.9," "1," and "1.3" [km s^{-1}]), followed by the Reynolds number of the physical shear viscosity ("9.8," "16.3," "19.5," and "∞"). Models with a different MHD solver are additionally denoted as "E," "D," and "LD" corresponding to HLLE, HLLD, and LHLLD, respectively. Models with

Table 4.1: Model parameters.

Model Name	n_0 [cm^{-3}]	B_0 [μG]	v_{x0} [km s^{-1}]	γ	$\mathcal{R}_{\rm shear}$ $\equiv v_{x0}\Delta x/\nu$	ambipolar diffusion	Solver
n1000b30v1$\mathcal{R}\infty$	1000	30	1.0	5/3	∞	No	Roe
n1000b30v1$\mathcal{R}$16.3	1000	30	1.0	5/3	16.3	No	Roe
n1000b30v1$\mathcal{R}$9.8	1000	30	1.0	5/3	9.8	No	Roe
n1000b30v1$\mathcal{R}\infty$E	1000	30	1.0	5/3	∞	No	HLLE
n1000b30v1$\mathcal{R}\infty$D	1000	30	1.0	5/3	∞	No	HLLD
n1000b30v1$\mathcal{R}$16.3D	1000	30	1.0	5/3	16.3	No	HLLD
n1000b30v1$\mathcal{R}$9.8D	1000	30	1.0	5/3	9.8	No	HLLD
n1000b30v1$\mathcal{R}\infty$LD	1000	30	1.0	5/3	∞	No	LHLLD
n1000b30v1$\mathcal{R}$16.3LD	1000	30	1.0	5/3	16.3	No	LHLLD
n1000b30v1$\mathcal{R}$9.8LD	1000	30	1.0	5/3	9.8	No	LHLLD
n1000b30v1.3a$\mathcal{R}\infty$D	1000	30	1.3	5/3	∞	No	HLLD
n1000b30v1.3a$\mathcal{R}\infty$LD	1000	30	1.3	5/3	∞	No	LHLLD
n1000b30v1	1000	30	1.0	1.01	19.5	No	Roe
n1000b30v1AD	1000	30	1.0	1.01	19.5	Yes	Roe
n800b30v1AD	800	30	1.0	1.01	19.5	Yes	Roe
n1300b30v1AD	1300	30	1.0	1.01	19.5	Yes	Roe
n1600b30v1AD	1600	30	1.0	1.01	19.5	Yes	Roe
n1000b24v1AD	1000	24	1.0	1.01	19.5	Yes	Roe
n1000b35v1AD	1000	35	1.0	1.01	19.5	Yes	Roe
n1000b40v1AD	1000	40	1.0	1.01	19.5	Yes	Roe
n1000b30v0.8AD	1000	30	0.8	1.01	19.5	Yes	Roe
n1000b30v0.9AD	1000	30	0.9	1.01	19.5	Yes	Roe

Table 4.2: Model parameters for the nonlinear evolution of one-shock SSI.

Model Name	$\lambda_{\rm p}$	ambipolar difusion
NL1Shock	0.1	No
NL1ShockAD	0.1	Yes
NL1Shock$\lambda_{\rm p}$0.01AD	0.01	Yes

ambipolar diffusion are additionally denoted as "AD." The set of parameters used in our simulations is listed in Table 4.1.

We also perform simulations for the case with initially perturbed shock position fluctuation, which is convenient for the investigation of nonlinear evolution. The initial density, velocity, and pressure field are set to be

$$\rho(x,y) = \rho_0 \left[1 + \frac{r-1}{2}\left(1 - \tanh\left[\frac{x - \xi \sin(2\pi y/\lambda_{\rm p})}{0.003L_{\rm box}}\right]\right)\right], \tag{4.15}$$

$$v_x(x,y) = -v_{x0} \left[1 + \frac{r-1}{2}\left(1 - \tanh\left[\frac{x - \xi \sin(2\pi y/\lambda_{\rm p})}{0.003L_{\rm box}}\right]\right)\right]^{-1}, \tag{4.16}$$

and

$$p(x,y) = p_0 \left[1 + \frac{r_{\rm pres}-1}{2}\left(1 - \tanh\left[\frac{x - \xi \sin(2\pi y/\lambda_{\rm p})}{0.003L_{\rm box}}\right]\right)\right], \tag{4.17}$$

where ξ is the initial amplitude of shock position fluctuation. We choose $n_0 = 1000\ {\rm cm}^{-3}$, $v_{x0} = 1\ {\rm km\ s}^{-1}$, $p_0 = \gamma\rho_0 c_{\rm s}^2$, $\mathcal{R}_{\rm shear} = 9.8$, and $\xi = 0.02$ pc. The initial uniform magnetic field is set to be along the x-axis and the strength of $B_0 = 30$ μG. The set of parameters used in our simulations of the nonlinear evolution of one-shock SSI is listed in Table 4.2.

4.2.2 Initial Condition for Two-Shocks Cases

Considering the realistic formation process of filaments, a filament is sandwiched by colliding flow. Thus, we also perform converging flow simulations. To understand SSI for the two-shocks case, we study the linear evolution for odd and even mode perturbation. In Figure 4.1, we show the schematic illustration of the initial density field. The initial density can be written as

$$\rho(x,y) = \rho_0 + \rho_{\rm p,right}(x,y) + \rho_{\rm p,left}(x,y). \tag{4.18}$$

The density perturbations $\rho_{\rm p,right}(x,y)$ and $\rho_{\rm p,left}(x,y)$ are set to be

$$\rho_{\rm p,right} = 10^{-4} \times \rho_0 \cos\left(\frac{2\pi y}{\lambda_{\rm p}}\right)\cos\left(\frac{\pi x}{0.01L_{\rm box}}\right),\ \text{if}\ 0.005L_{\rm box} \le x \le 0.015L_{\rm box} \tag{4.19}$$

and

$$\rho_{\rm p,left} = \pm 10^{-4} \times \rho_0 \cos\left(\frac{2\pi y}{\lambda_{\rm p}}\right)\cos\left(\frac{\pi x}{0.01L_{\rm box}}\right),\ \text{if}\ -0.015L_{\rm box} \le x \le -0.005L_{\rm box} \tag{4.20}$$

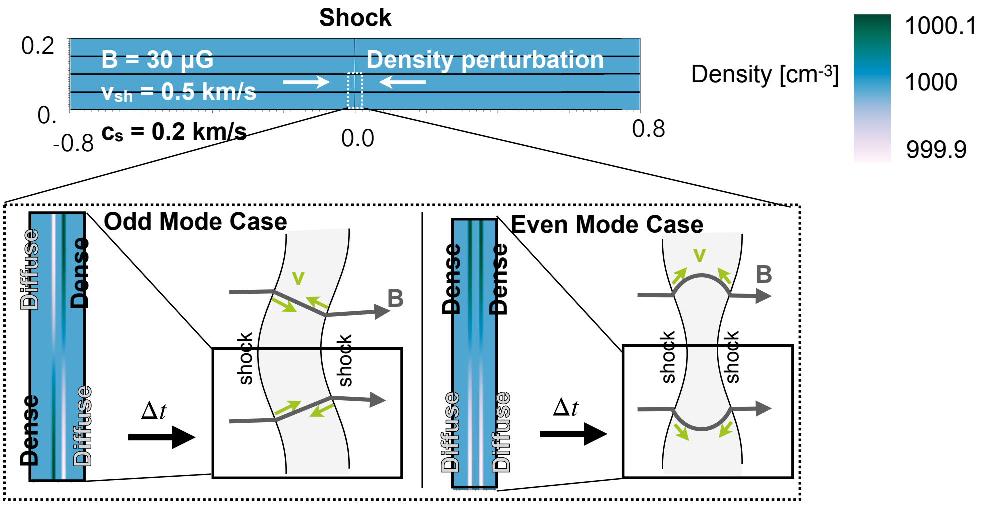

Figure 4.1: Schematic illustration of the initial density field to study the stability of odd and even mode SSI. (models 2S-odd, 2S-even, and 2S-evenB24)

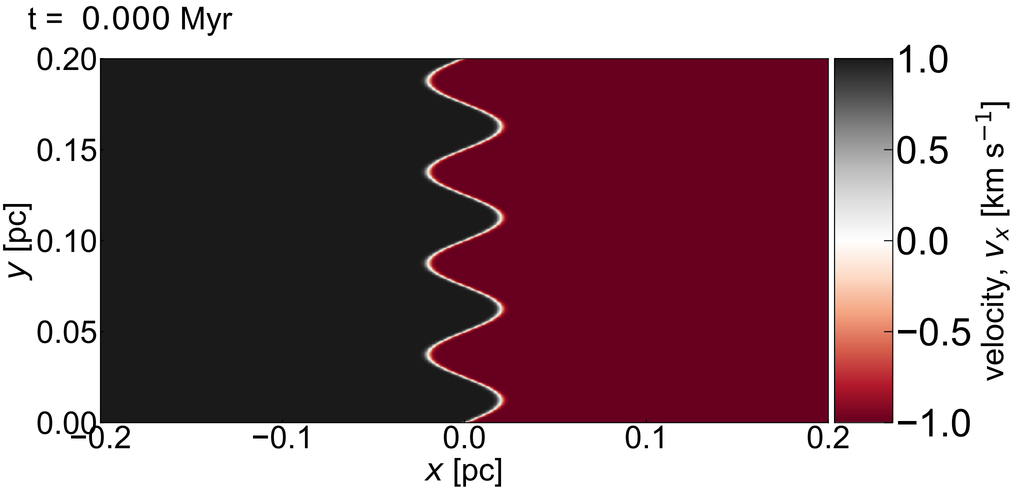

Figure 4.2: The initial velocity field for model NL2Shockλ0.05. The initial condition with shock position fluctuation is convenient for the investigation of nonlinear evolution.

Table 4.3: Model parameters to study the stability of two-shocks SSI in the liner evolution.

Model Name	One-shock or Two-shocks	B_0 [μG]	$v_{\rm x0}$ [km s^{-1}]	density perturbation
2S-odd	Two	30	0.5	Odd
2S-even	Two	30	0.5	Even
2S-evenB24	Two	24	0.5	Even
1S-odd	One	30	0.56	Odd

Table 4.4: Model parameters to study the nonlinear evolution.

Model Name	$\lambda_{\rm p}$	ξ	$\mathcal{R}_{\rm shear}$	Ambipolar Diffusion
NL2Shockλ0.05	0.05	0.02	9.8	No
NL2ShockRand	-	0.0005	9.8	No
NL2Shockλ0.05AD	0.05	0.02	9.8	Yes
NL2Shockλ0.05ADξ0.005	0.05	0.005	9.8	Yes
NL2Shockλ0.01AD	0.01	0.02	∞	Yes
NL2ShockRandAD	-	0.0005	∞	Yes

where the plus/minus sign indicates even/odd mode, respectively. We set the x component of the velocity field as

$$v_x(x, y) = -v_{x0} \tanh[x/0.003L_{\rm box}]. \tag{4.21}$$

The velocity field of y and z component are $v_y(x, y) = 0$ [km s^{-1}] and $v_z(x, y) = 0$ [km s^{-1}], respectively. The initial pressure field is $p(x, y) = \gamma\rho(x, y)c_{\rm s}^2$. The set of parameters used in our simulations of the linear evolution of two-shock SSI is listed in Table 4.3.

We also perform simulations for the case with initially perturbed shock position fluctuation. As will be shown in §4.3, only the odd mode perturbation is unstable, thus the only odd mode case is studied. Initial density and pressure are set to be uniform, $\rho(x, y) = \rho_0$ and $p(x, y) = p_0$. We change the x component of the velocity field as

$$v_x(x, y) = -v_{x0} \tanh\left[\frac{x - \xi \sin(2\pi y/\lambda_{\rm p})}{0.003L_{\rm box}}\right]. \tag{4.22}$$

In Figure 4.2, an example of the x component of the initial velocity field is shown. We also study the case with random fluctuation. In this case, the x component of the velocity field is

$$v_x(x, y) = -v_{x0} \tanh\left[\frac{x - \xi \sum_{k_{\rm box}=1}^{n_{\rm mode}} \sin(2\pi y/\lambda_{\rm p}))}{0.003L_{\rm box}}\right], \tag{4.23}$$

where, $k_{\rm box} \equiv L_{\rm box}/\lambda_{\rm p}$ is the wave number normalized by box scale. The set of parameters used in our simulations of the nonlinear evolution of two-shock SSI is listed in Table 4.4.

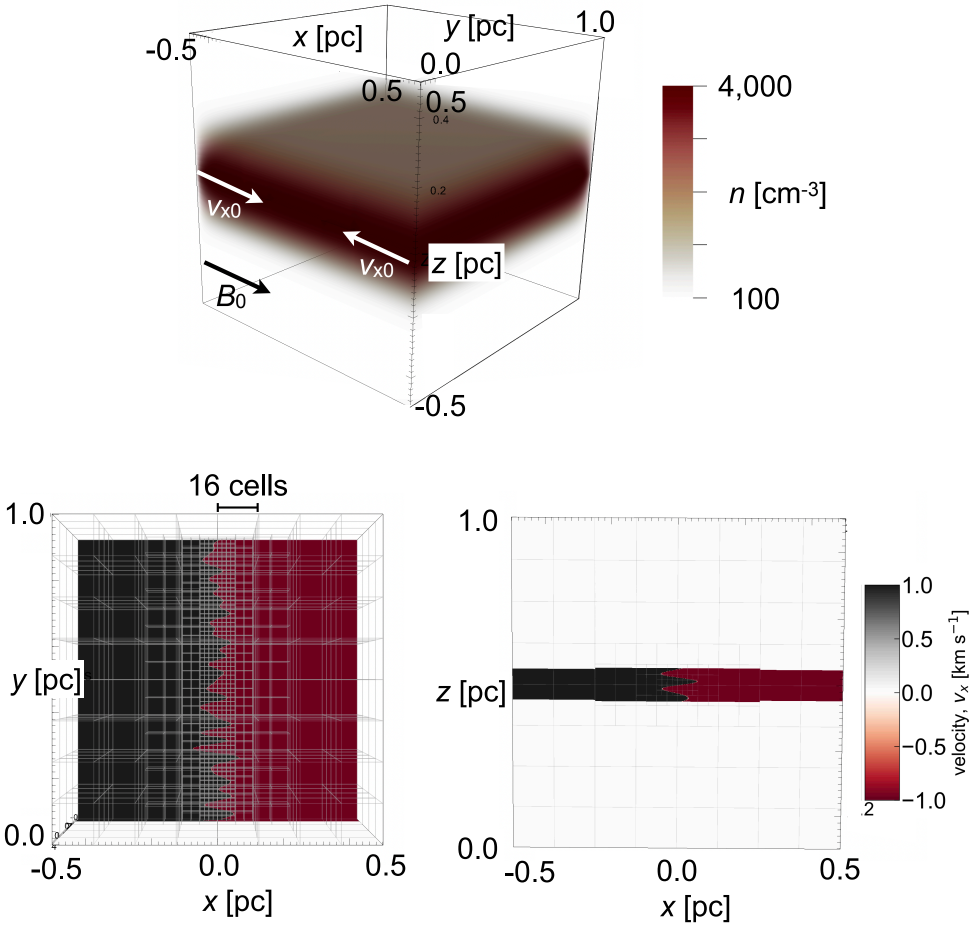

Figure 4.3: Schematic of the grid structure and the initial condition. *Top panel*: The color bar represents the density magnitude, the black arrows represent the orientations of the initial magnetic field, and the white arrows represent the orientations of the converging flows. *Bottom left panel*: Grid structure (grey lines) and the initial velocity field at z = 0 pc plane. *Bottom right panel*: Same as bottom left panel but for the y = 0 pc plane.

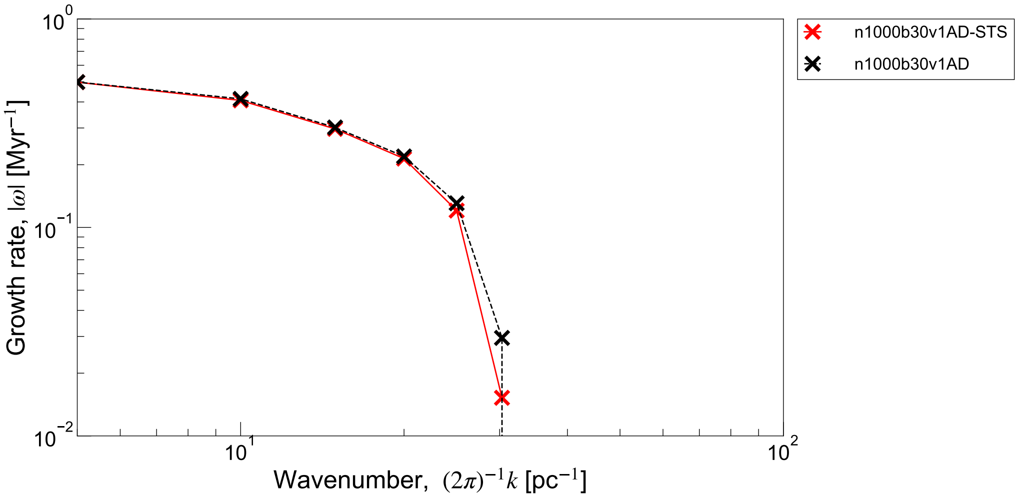

Figure 4.4: Dispersion relations for the model n1000b30v1 (grey) and n1000b30v1AD-STS (red).

4.2.3 Initial Condition for Three-dimensional Simulation

We perform a three-dimensional simulation including self-gravity to investigate the nonlinear evolution of massive filament. Considering the realistic situation of filament formation, we set a dense sheet as the initial condition. The initial density can be written as

$$n(x,y,z) = (n_{\rm sheet} - n_{\rm ext}) \exp\left(-\frac{z^2}{2H^2}\right) + n_{\rm ext}, \tag{4.24}$$

where, $n_{\rm sheet} = 4000$ cm^{-3}, $n_{\rm ext} = 100$ cm^{-3}, and $H = 0.1$ pc are number density of the dense sheet and ambient gas, the thickness of the sheet. We set the x component of the velocity field as

$$v_x(x,y,z) = -v_{x0} \tanh\left[\frac{x - \xi \sum_{k_{\rm box}=1}^{n_{\rm mode,y}} \sin(2\pi y/\lambda_{\rm p}) \sin(2\pi z/\lambda_{\rm p}))}{0.003 L_{\rm box}}\right], \text{ if } -H/2 \le z \le H/2. \tag{4.25}$$

The velocity field of y and z component are $v_y(x,y,z) = 0$ [km s^{-1}] and $v_z(x,y,z) = 0$ [km s^{-1}], respectively. The initial pressure field is $p(x,y) = \gamma\rho(x,y,z)c_{\rm s}^2$. We set the initial uniform magnetic field along the x-axis $B_0 = 50$ μG. In Figure 4.3, we show the schematic illustrations of the initial condition.

Static mesh refinement technique is used to resolve a filament and reduce the calculation costs (see Figure 4.3). The finest resolution is $\Delta x = 1/1024$ pc $\simeq 0.00098$ pc. This leads to a bottleneck to solve ambipolar diffusion because the time step Δt is proportional to Δx^2 when the diffusion equation is solved numerically. Thus, we use the super time stepping method (Meyer et al., 2014). The time stepping under the CFL condition is based on the condition that the solution is stable at the next time step i.e., no unphysical behavior or oscillations. The super time stepping method relaxes this restriction and requires the solution to be stable after larger time steps than the one which is determined by the CFL condition. A parameter of the super time stepping method is the maximum time step ratio max$(dt/dt_{\mathrm{parabolic}})$ which is the limit time step if the ratio of overall time step dt calculated by fluid equations to time step $dt_{\mathrm{parabolic}}$ calculated by a diffusion equation exceeds this value. It is necessary to test that the time integration using the super time stepping method is not significantly different from the time integration without it. We test the super time stepping method with the same initial condition as model n1000b30v1AD and $\lambda_{\mathrm{p}} = 0.05$ pc, and we perform a simulation with max$(dt/dt_{\mathrm{parabolic}}) = 1000$ as model n1000b30v1AD-STS. Figure 4.4 shows the dispersion relations for model n1000b30v1AD (black) and n1000b30v1AD-STS (red). In nonlinear evolution, we measure the maximum value of $\|(\rho_{\mathrm{STS}}(x,y,z) - \rho(x,y,z))/\rho(x,y,z)\| \simeq 0.2$ at $t = 0.5$ Myr in only about 10 cells, where, $\rho_{\mathrm{STS}}(x,y,z)$ is the density for model n1000b30v1AD-STS. We can confirm that the results do not change a lot even max$(dt/dt_{\mathrm{parabolic}}) = 1000$.

4.3 Results

4.3.1 Linear Evolution for One-shock SSI

Selection of Numerical Scheme and Physical Viscosity

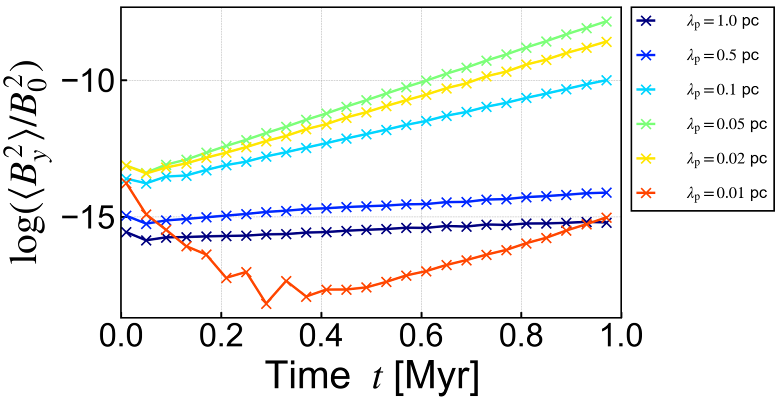

Figure 4.5: Evolution of the mean value of the perturbed magnetic field for the case with adiabatic ideal MHD including physical shear viscosity (model n1000b30v1$\mathcal{R}$9.8).

We perform simulations for the case of $\gamma = 5/3$ and compare the results with dispersion relation (Eq. [1.23]), by which we can check whether the selected numerical scheme appropriately reproduces the regime of linear instability. The method to measure the growth rate of SSI is the same as the method developed by Stone & Edelman (1995). It is convenient to use compression weighted averages because we need to evaluate physical quantities in the vicinity of a shock wave. We can write compression-weighted transverse magnetic energy as follows.

$$\left\langle B_y^2 \right\rangle = \frac{\int B_y^2 C dV}{\int C dV} \tag{4.26}$$

where,

$$C = \min\left(\partial v_x / \partial x, 0\right). \tag{4.27}$$

In Figure 4.5, we show the evolution of $\left\langle B_y^2 \right\rangle$ in model n1000b30v1a. The slope of each line in Figure 4.5 reflects the growth rate. The growth rate can be measured from the slope of $\left\langle B_y^2 \right\rangle$ as

$$\omega_{\rm num} = \left(2\log_{10} e\right)^{-1} \frac{d}{dt} \log_{10} \frac{\left\langle B_y^2 \right\rangle}{B_0^2} \simeq \left(2\log_{10} e\right)^{-1} \frac{\Delta \log_{10} \left\langle B_y^2 \right\rangle / B_0^2}{\Delta t}. \tag{4.28}$$

where, $\frac{\Delta \log_{10} \left\langle B_y^2 \right\rangle / B_0^2}{\Delta t}$ is the gradient in the t–$\log_{10} \left\langle B_y^2 \right\rangle / B_0^2$ plane. We can confirm linear growth. For $\lambda_{\rm p} = 0.01$ pc, $\left\langle B_y^2 \right\rangle / B_0^2$ decreases until ~ 0.3 Myr, a larger scale noise start to grow after $t \sim 0.3$ Myr, which is different from the growth of $\lambda_{\rm p} = 0.01$ pc mode. Since the initial perturbation is not given as the eigenstate of the SSI, the SSI does not start to grow $t = 0$. Thus we define the measuring range as $[t_0 = t_{\rm start} + f t_{\rm growth}, t_0 + t_{\rm range}]$ to observe the linear growth of SSI. where, $t_{\rm growth} \equiv 1/\omega_{\rm ana}$ is a growth timescale We choose $t_{\rm ini} = 0.05$ Myr, $t_{\rm range} = 0.2$ Myr and $f = 0.4$.

The HLLD and LHLLD Riemann solvers is a robust and high-resolution MHD solver, but it does not take into account the slow mode characteristics in the Riemann problem, and it is necessary to test the optimal solver for solving SSI. We perform simulations using HLLD, LHLLD, HLLE, and Roe solvers to decide which solver is the best for solving SSI. If physical shear viscosity is not included, the measurement of the growth rate fails due to the carbuncle phenomenon. We can prevent the carbuncle phenomenon by introducing physical shear viscosity. Grid noise, which is numerically induced noise whose scale is different from a given $\lambda_{\rm p}$, potentially becomes the seed of SSI. The growth of SSI seeded by the grid noise may arise after a long time integration (e.g., see the red line in Figure [4.5]), thus we avoid measuring the growth of grid noise by adjusting the $t_{\rm range}$.

The top panel of Figure 4.6 shows the dispersion relation for adiabatic cases calculated using HLLE or Roe solvers (models n1000b30v1a$\mathcal{R}\infty$E, n1000b30v1a$\mathcal{R}\infty$, n1000b30v1a$\mathcal{R}$16.3, and n1000b30v1a$\mathcal{R}$9.8). The dashed line represents Eq. (1.23). The vertical dotted line represents the scale of $\lambda = 8\Delta x$. We can see that the grid scale structure created by the carbuncle phenomenon is suppressed by introducing physical shear viscosity. For simulations employing the HLLE solver, we do not introduce the physical shear viscosity, since the carbuncle phenomenon does not occur, however very diffusive nature of the HLLE solver makes SSI attenuate at $0.02 \leq \lambda_{\rm p} < 0.05$ pc (see, filled triangles). In the results with the Roe solver without the physical shear viscosity (bold cross marks), we cannot measure growth rates at long wavelength regimes, due to the contamination by the carbuncle phenomenon. For model n1000b30v1$\mathcal{R}$16.3 (blue crosses), the carbuncle phenomenon still appears at $\lambda_{\rm p} = 0.02$ pc (see the right edge of the blue curve). Using the Roe

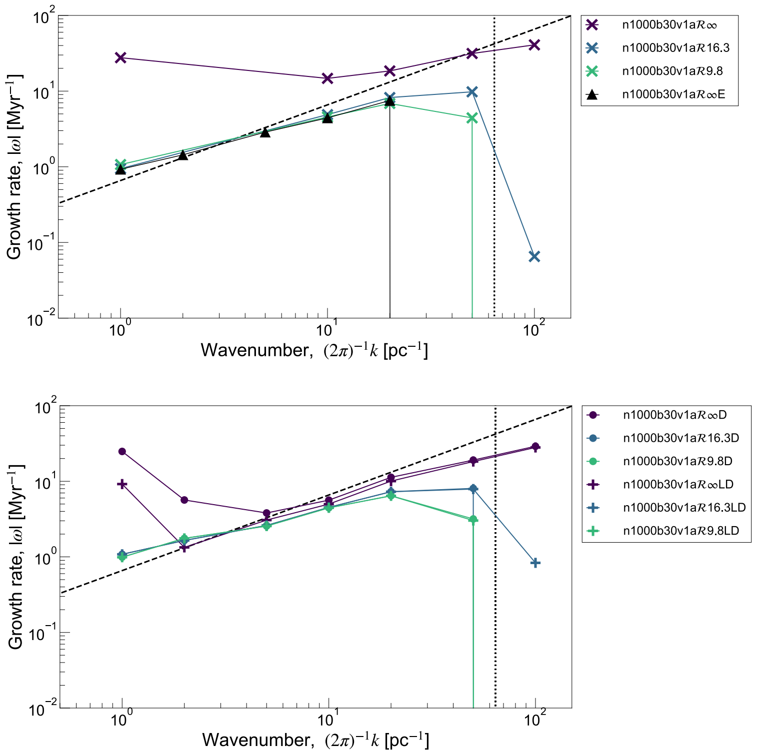

Figure 4.6: Dispersion relation for adiabatic cases. *Top panel*: Dispersion relations for the case with Roe (cross marker, models n1000b30v1a$\mathcal{R}\infty$, n1000b30v1a$\mathcal{R}$16.3, and n1000b30v1a$\mathcal{R}$9.8) and HLLE (triangle marker, model n1000b30v1a$\mathcal{R}\infty$E) solvers. Black and purple lines show the non-viscous results. Blue and green lines show the result with $\mathcal{R}_{\rm shear} = 16.3$ and $\mathcal{R}_{\rm shear} = 9.8$. *Bottom panel*: the same as top panel, but for the case with HLLD (circle marker, models n1000b30v1a$\mathcal{R}\infty$D, n1000b30v1a$\mathcal{R}$16.3D, and n1000b30v1a$\mathcal{R}$9.8D) and LHLLD (plus marker, models n1000b30v1a$\mathcal{R}\infty$LD, n1000b30v1a$\mathcal{R}$16.3LD, and n1000b30v1a$\mathcal{R}$9.8LD) solvers.

method with $\mathcal{R}_{\rm shear} = 9.8$ (see green crosses), the SSI growth rate can be measured with high resolution (down to ~ 0.02 pc) as well as preventing carbuncle phenomenon.

The bottom panel of Figure 4.6 shows the same as the top but results using HLLD or LHLLD solvers (models n1000b30v1a$\mathcal{R}\infty$D, n1000b30v1a$\mathcal{R}$16.3D, n1000b30v1a$\mathcal{R}$9.8D, n1000b30v1a$\mathcal{R}\infty$LD, n1000b30v1a$\mathcal{R}$16.3LD, and n1000b30v1a$\mathcal{R}$9.8LD). The simulation using HLLD suffers from the carbuncle phenomenon. The LHLLD scheme is designed to alleviate the carbuncle phenomenon, but after a long time integration, the growth of grid noise appears. Both schemes give similar results, but we fail to measure for $\lambda_{\rm p} > 1.0$ pc modes if we do not involve physical shear viscosity by the effects of the carbuncle phenomenon due to slower growth of the SSI than the carbuncle phenomenon (see filled purple circles and purple plus marks). It should be mentioned that the results using LHLLD are more close to the approximated analytical solution than those using HLLD at $\lambda_{\rm p} \leq 0.5$ pc.

Simulations using either HLLD or LHLLD successfully reproduce the growth of SSI for $\mathcal{R}_{\mathrm{shear}} = 9.8$.

In a conclusion, we find that the HLLD, LHLLD, and Roe solvers with adjusted physical shear viscosity can correctly calculate the growth rate of SSI over a wide scale range. We can use any of the HLLD, LHLLD, and Roe solvers to measure the linear growth rate, but in the following sections, we use the Roe solver that shows numerically more stable features in nonlinear regimes (see, Appendix).

Dispersion Relation of SSI in Molecular Clouds

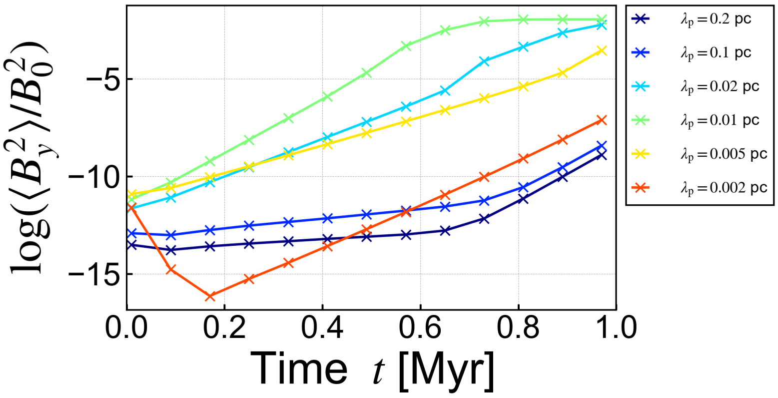

Figure 4.7: Evolution of the mean value of the perturbed magnetic field for the case with isothermal ideal MHD including physical shear viscosity (model n1000b30v1).

Since the isothermal treatment is justified in dense regions of molecular clouds, we adopt $\gamma = 1.01$. We measure the growth rate in the same way as §4.3.1. In Figure 4.7, we show the evolution of the mean value of the perturbed magnetic field for model n1000b30v1. For $\lambda_{\mathrm{p}} = 0.002$ pc, $\langle B_y^2 \rangle / B_0^2$ decreases until ~ 0.2 Myr, then a larger scale ($>$ 0.002 pc) grid noise grows after $t \sim 0.2$ Myr, which is different from the growth of $\lambda_{\mathrm{p}} = 0.002$ pc mode of the SSI. For $\lambda_{\mathrm{p}} = 0.2, 0.1, 0.02, 0.005$ pc, we can see the slope increments of the perturbed magnetic field after $t = 0.7$ Myr caused by grid noise. $\langle B_y^2 \rangle / B_0^2$ converges to -4 after $t = 0.75$ Myr for $\lambda_{\mathrm{p}} = 0.01$ due to the saturation of SSI (Stone & Edelman, 1995). As in §4.3.1, the range to measure the linear growth rate is $[t_0 = t_{\mathrm{start}} + f t_{\mathrm{growth}},\ t_0 + t_{\mathrm{range}}]$, and we choose $t_{\mathrm{start}} = 0.05$ Myr, $t_{\mathrm{range}} = 0.5$ Myr, and $f = 0.6$. We show the dispersion relation for the isothermal ideal MHD case including physical shear viscosity (model n1000b30v1) as the grey cross marks in Figure 4.9. We find that, if we use $\mathcal{R}_{\mathrm{shear}} = 19.5$, we find that a physical dispersion relation is successfully obtained by suppressing the carbuncle phenomenon.

SSI v.s. Ambipolar Diffusion

We perform a similar analysis as in §4.3.1 for the simulation results including ambipolar diffusion. In Figure 4.8, we show the evolution of the mean value of the

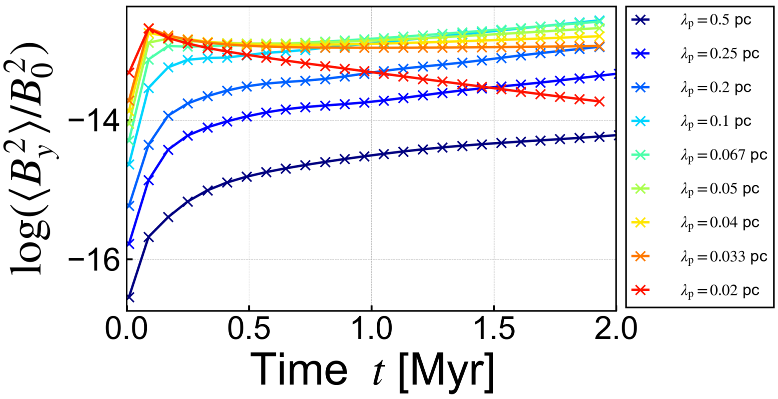

Figure 4.8: Evolution of the mean value of the perturbed magnetic field for the case with isothermal ideal MHD including ambipolar diffusion and physical shear viscosity (model n1000b30v1AD).

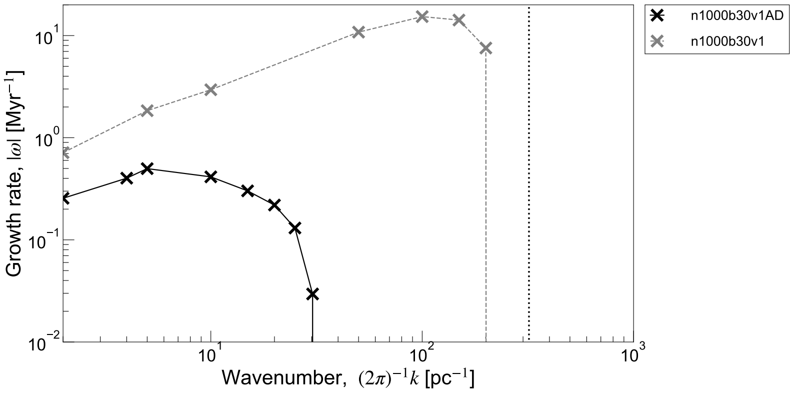

Figure 4.9: Dispersion relation for the model n1000b30v1 (grey) and n1000b30v1AD (black).

perturbed magnetic field for model n1000b30v1AD. Because the effect of ambipolar diffusion makes the phase speed of the Alfvén wave smaller, it takes more time for the eigen state to develop from the given initial perturbation compared to the ideal MHD case. Thus, for measuring the liner phase growth rate, we take longer $t_{\rm start}$ of 1.2 Myr, and $f = 0.6$ and $t_{\rm range} = 0.3$ Myr. We show the dispersion relation for the isothermal MHD case including ambipolar diffusion (model n1000b30v1AD) as the black cross marks in Figure 4.9. We can see the damping of the SSI growth by the ambipolar diffusion. We find that the most unstable scale $\ell_{\rm max} \simeq 0.2$ pc and the damping scale $\ell_{\rm damp} \simeq 0.02$ pc.

To investigate the parameter dependence on the most unstable scale, we perform a parameter survey for unperturbed magnetic field strength, density, and shock velocity. In Figure 4.10, we show the dispersion relation for models n1000b24v1AD, n1000b40v1AD, n800b30v1AD, n1600b24v1AD, n1000b30v0.8AD. We can confirm that the most unstable scale changes with the magnetic field density and

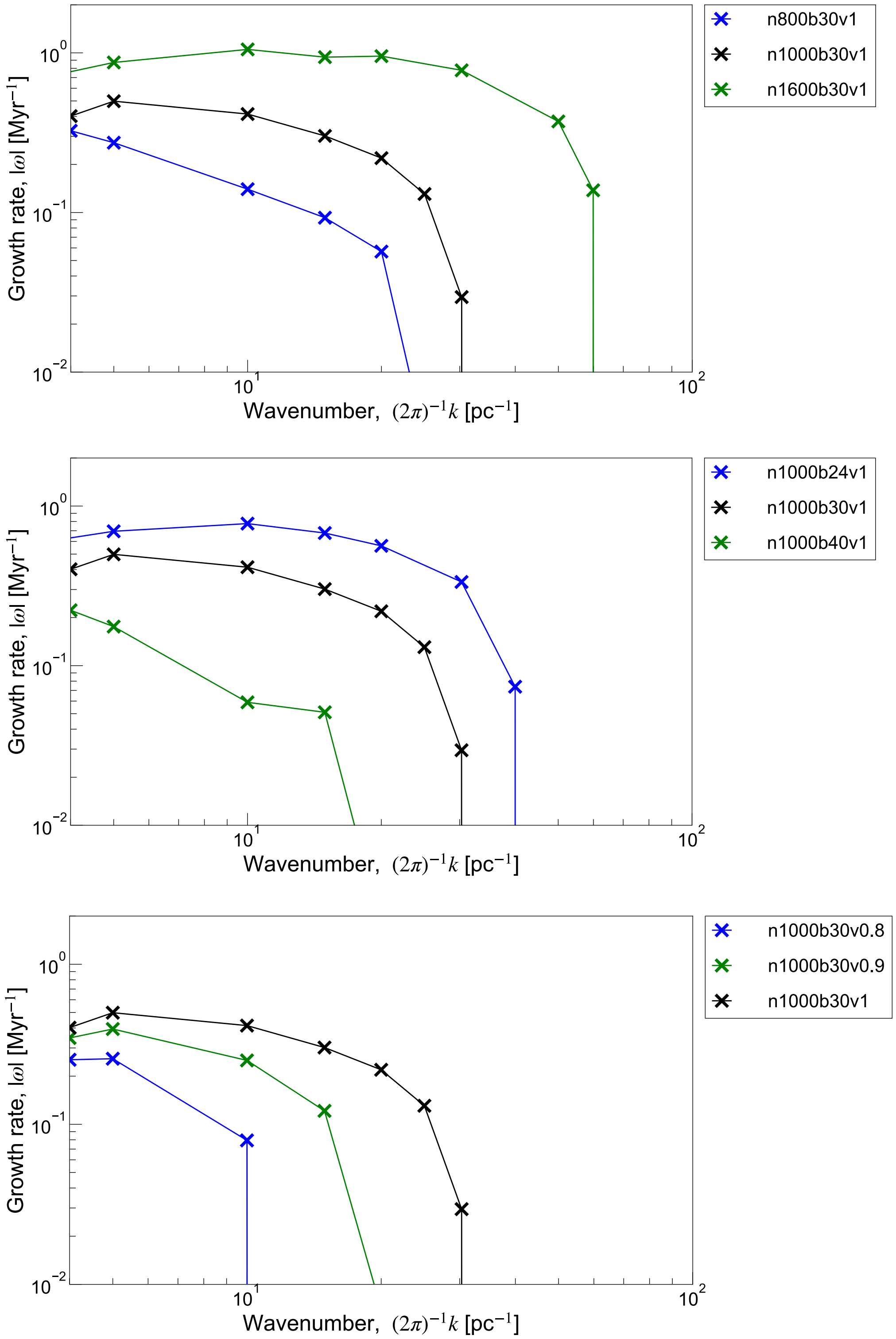

Figure 4.10: Dispersion relation for the models n1000b30v1AD, n1600b30v1AD, n800b30v1AD, n1000b24v1AD, n1000b40v1AD, and n1000b30v0.8AD.

velocity. The larger the density/velocity, the smaller the most unstable scale of ambipolar diffusion. Contrary, the larger the magnetic field, the larger the damping scale. These trends can be understood by the scale of ambipolar diffusion $\ell_{\rm damp} \sim \ell_{\rm AD} \propto B_0^2 \rho^{-3/2} v_{x0}^{-1}$ (Eq. [4.2]).

4.3.2 Nonlinear Evolution for One-shock SSI

We show the density maps of nonlinear evolution for model NL1Shock in Figure 4.11. The white lines represent the contour of the vector potential, i.e., magnetic field lines. The results are consistent with Stone & Edelman (1995). The preshock gas flows along the magnetic field lines, pushing the fluid away from the peaks and concentrating it in the valleys. This effect reduces/increases preshock densities in peak/valley and provides the observed changes in postshock densities. Changes in preshock density affect shock velocities, causing peak/valley velocities to be higher/lower than average, resulting in finger growth.

In the left panels of Figure 4.12, we show the density maps of non-linear evolution including ambipolar diffusion (model NL1ShockAD). We can confirm the growth rate of shock position fluctuation is slowed down due to ambipolar diffusion. The right panels of Figure 4.12 show the density maps of non-linear evolution including ambipolar diffusion (model NL1Shock$\lambda_{\rm p}$0.01AD). Because $\lambda_{\rm p} = 0.01$ pc $< \ell_{\rm damp} \simeq 0.03$ pc, i.e., ambipolar diffusion strongly affects, shock position fluctuation is stabilized and disappears. Figure 4.13 shows that the gas flows along the shock front (see top panel), leading to the formation of high-density regions at the valleys (see left panels of Figure 4.12). The magnetic field structure is close to the eigen state of slow shock and kinks around the shock front (see a bottom panel or white lines in Figure 4.12). These indicate that ambipolar diffusion strongly works around the shock front. This result is consistent with Snow & Hillier (2021).

4.3.3 Linear Evolution for Two-shocks SSI

We measure the growth rate to investigate the stability of odd and even mode SSI. Here we used the HLLE solver, which does not require physical shear viscosity adjustment to suppress the grid scale fluctuations, since we only need to check whether odd/even mode SSI is stable or not. The evolution of the perturbed magnetic field is shown in Figure 4.14. The cross, plus, and round markers are the results for models 2S-odd, 1S-odd, and 2S-even, respectively. For model 1S-odd, we choose $v_{x0} = v_{\rm sh} = 0.56$ km s^{-1} to consistently compare the result for 2S-odd because the shock velocity for model 2S-odd is $v_{\rm sh} = v_{x0} + v_1 \simeq v_{x0} + v_{x0}/\mathcal{M}_{\rm s}^2 = v_{x0} + v_{x0} c_{\rm s}^2 / v_{\rm sh}^2$ then $v_{\rm sh} \simeq 0.56$ km s^{-1}. We can confirm that odd mode SSI is unstable. Comparing the results for models 2S-odd and 1S-odd, the slope is almost the same indicating that the growth rate for the odd mode SSI is similar to the one-shock case. For model 2S-odd, the perturbed magnetic field is more amplified than 2S-odd at the initial stage of $t \simeq 0$ Myr, but we cannot examine the reason in our setup since the initial perturbation is not given as the eigen state for the SSI.

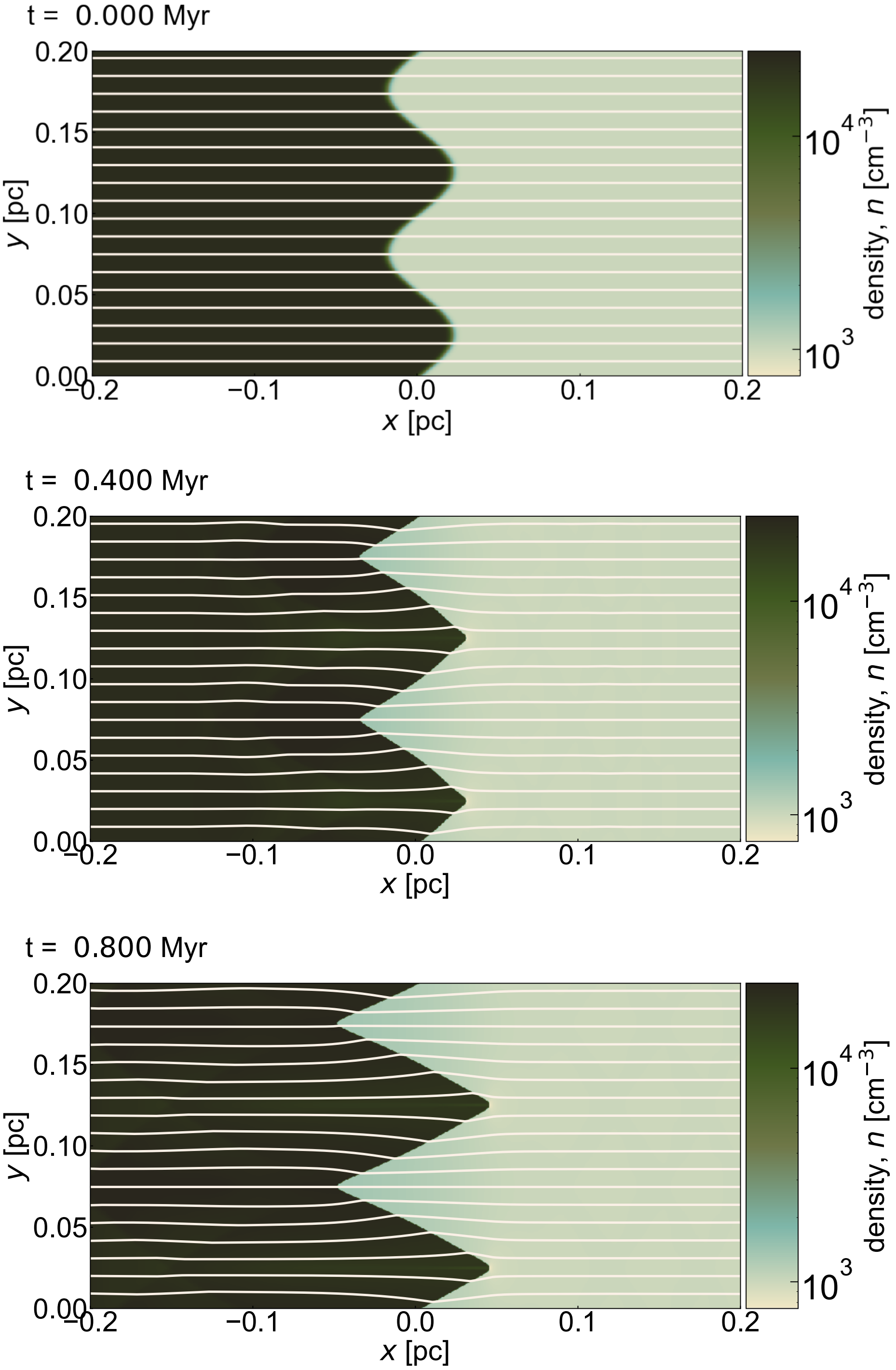

Figure 4.11: Density maps in the result of model NL1Shock at time $t = 0.0$, 0.4, and 0.8 Myr (from top to bottom). White lines represent the magnetic field lines.

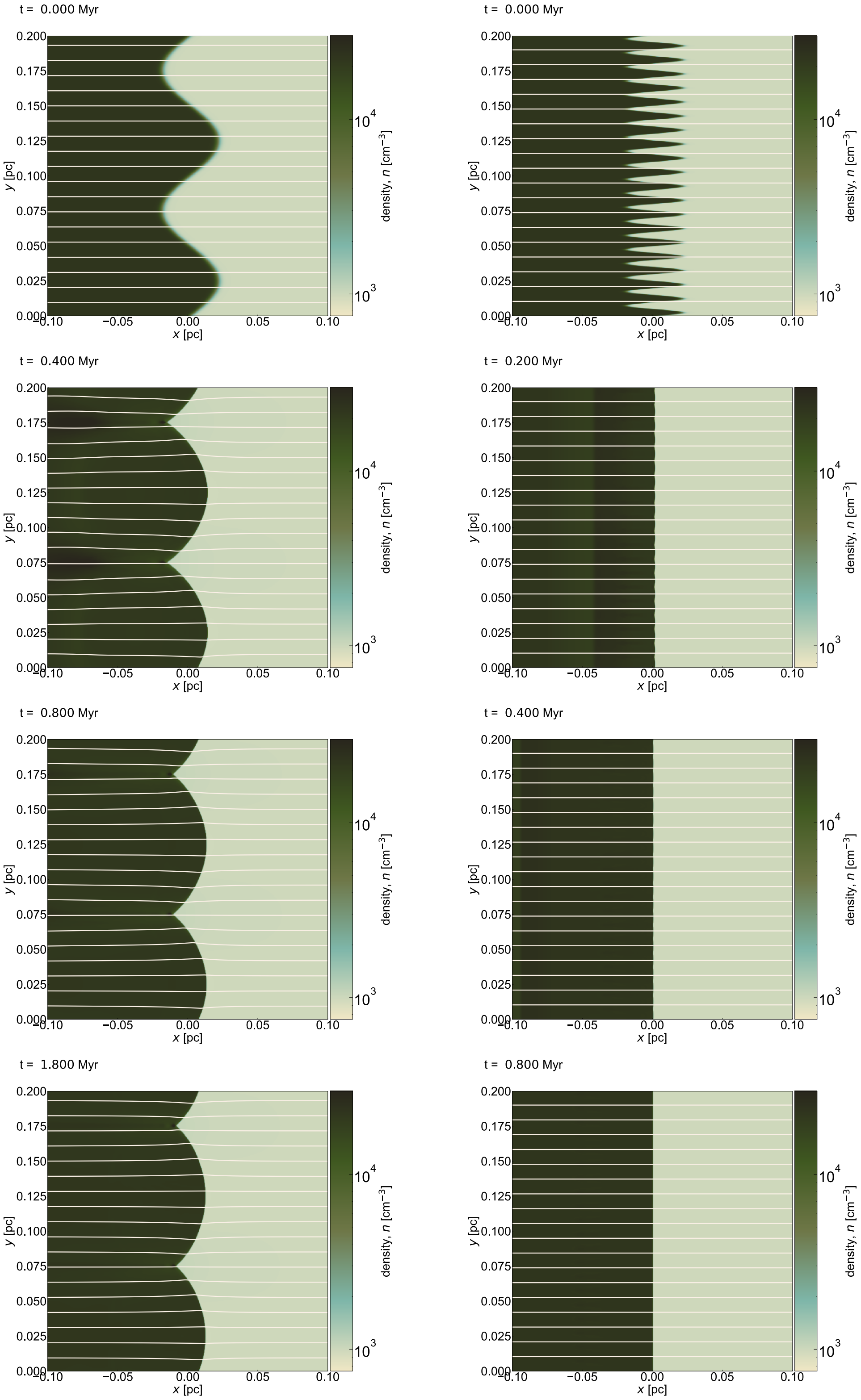

Figure 4.12: Same as Figure 4.12 but for model NL1ShockAD (left column) and NL1Shockλ_p0.01AD (right column).

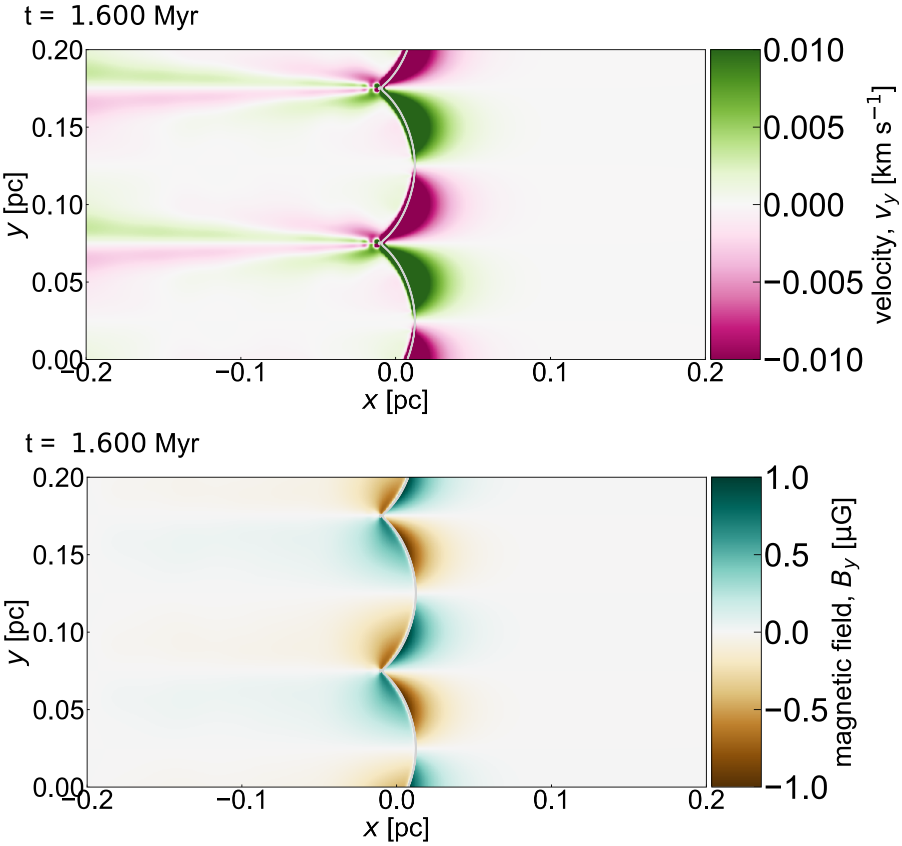

Figure 4.13: v_y and B_y maps in the result of model NL1ShockAD at time $t = 1.6$ Myr.

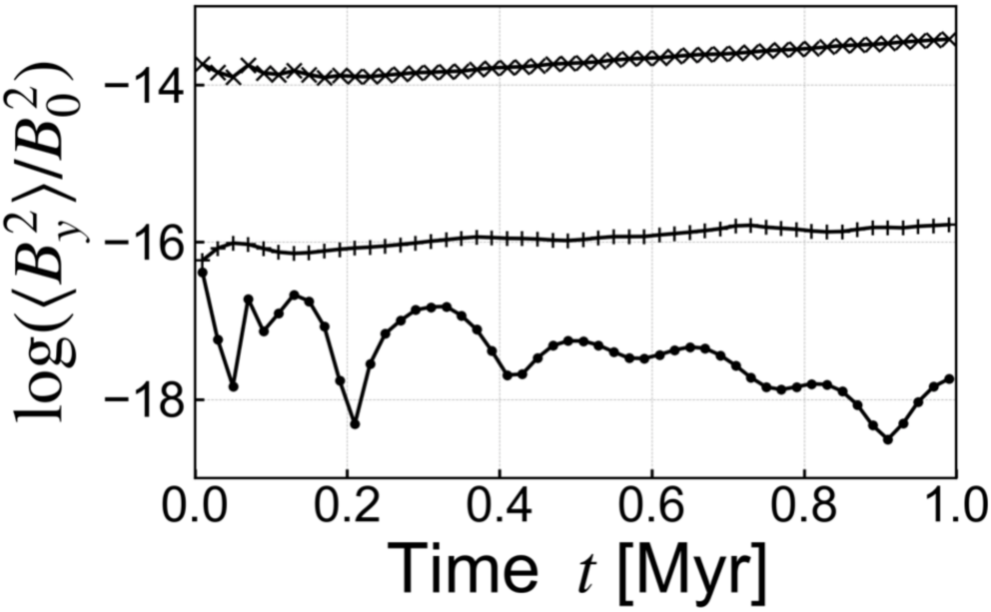

Figure 4.14: Evolution of the mean value of the perturbed magnetic field for the case with isothermal ideal MHD. The cross, plus, and, circle markers are the results for models 2S-odd, 1S-odd, and 2S-even.

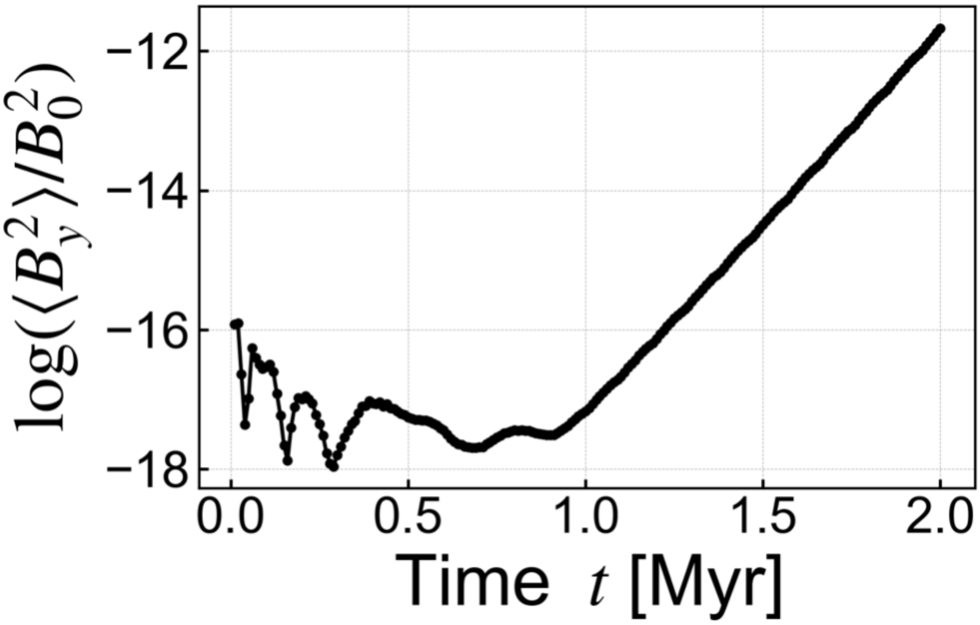

Figure 4.15: Evolution of the mean value of the perturbed magnetic field for the case with isothermal ideal MHD for model 2S-evenB24.

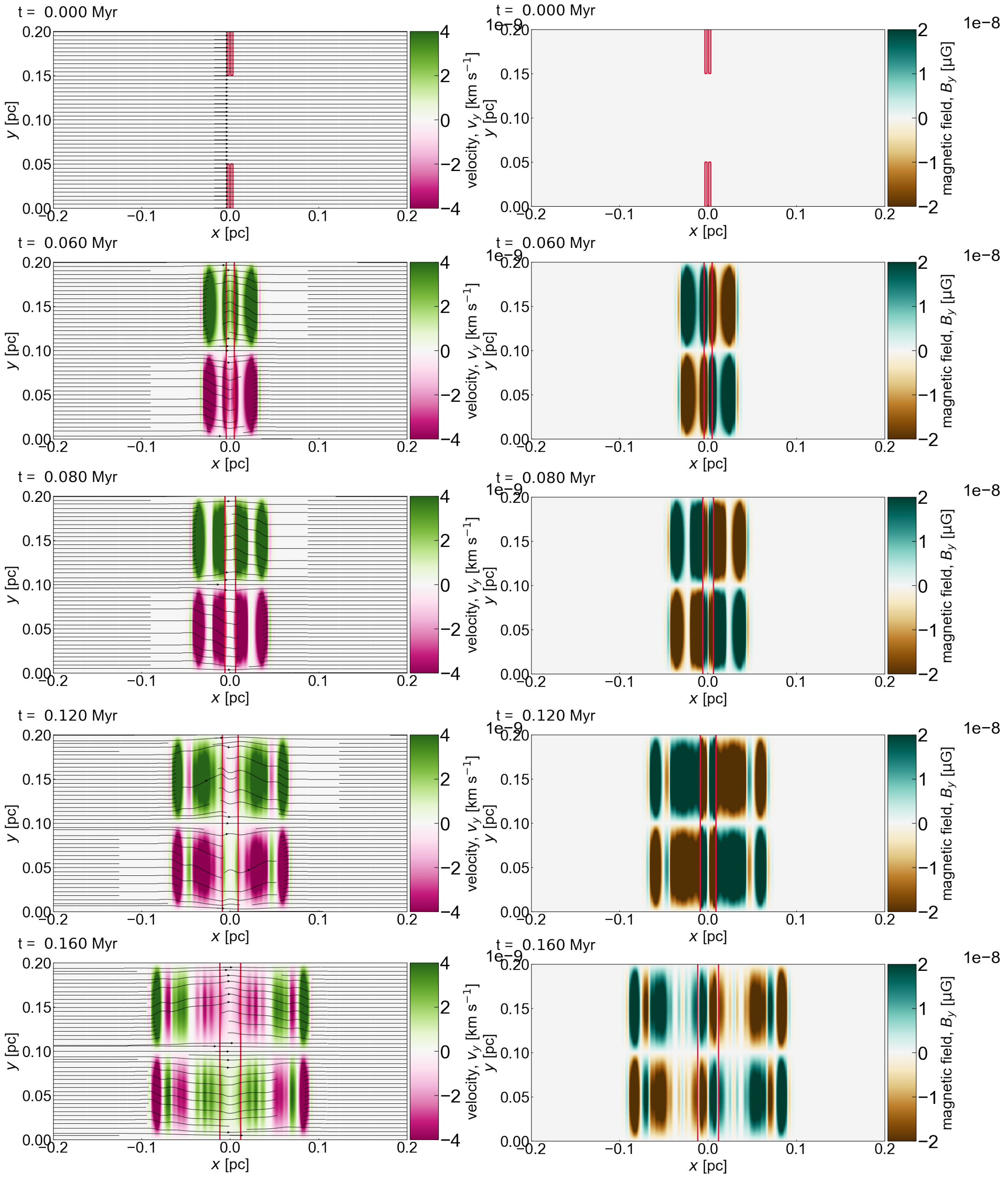

Figure 4.16: y component of velocity (left column) and magnetic field (right column) maps in the result of model 2S-even at time t = 0.0, 0.06, 0.08, 0.12, and 0.16 Myr (from top to bottom). Red lines show the density contour. Black lines represent the streamlines of the magnetic field. Note that these streamlines are not real magnetic field lines because we plot them with the B_y emphasized.

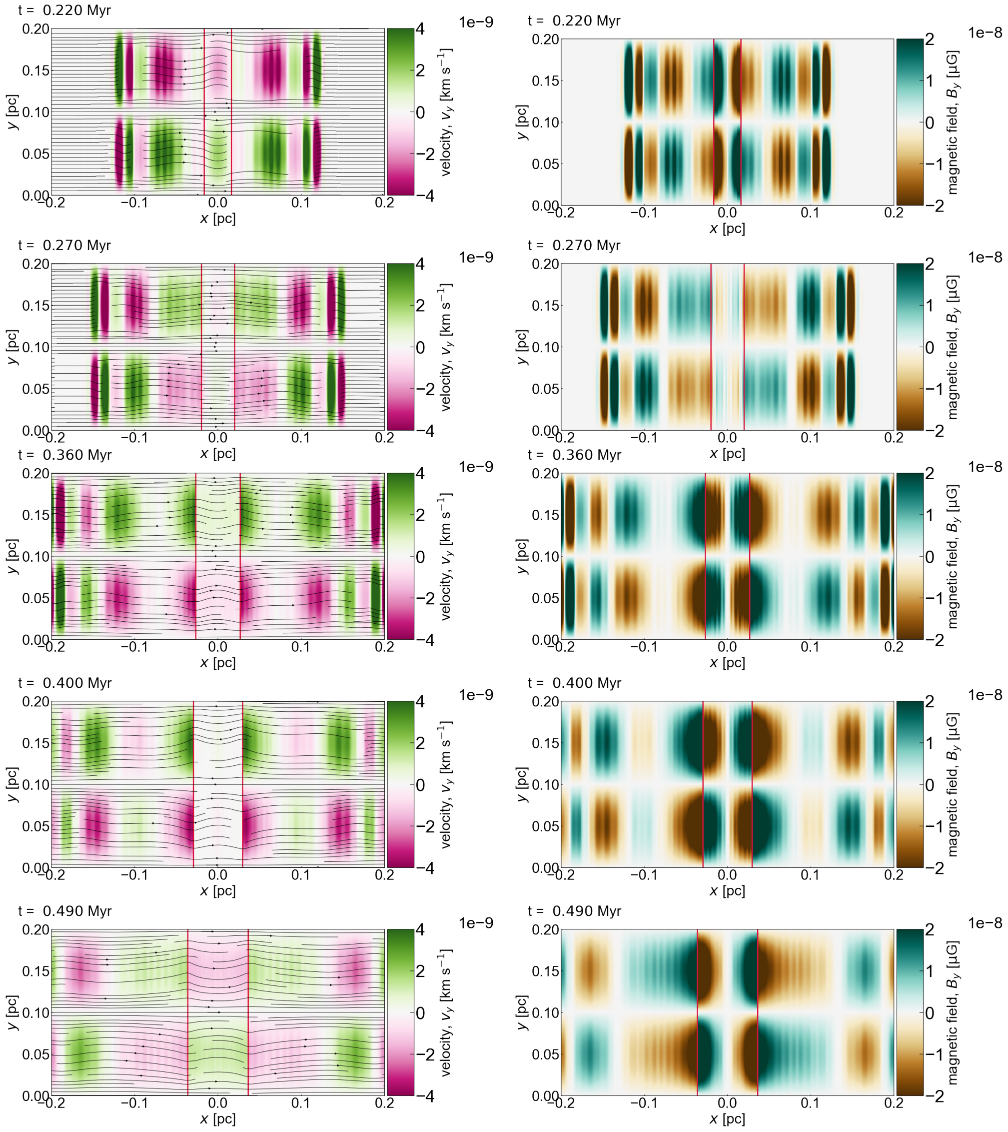

Figure 4.17: Same as Figure 4.16 but for $t = 0.22$, 0.27, 0.36, 0.40, and 0.49 Myr (from top to bottom).

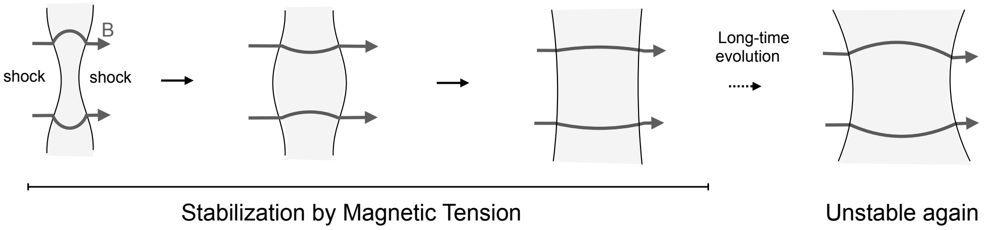

Figure 4.18: Schematic illustration of the interpretation of the result for model 2S-evenB24.

For the case in the even mode (model 2S-even), the magnitude of the perturbed magnetic field globally decreases with oscillating indicating that the even mode SSI is stable. In Figure 4.15, we show the long evolution of the perturbed magnetic field for a higher growth rate model 2S-evenB24. We can confirm that stabilization for the even mode works at the initial stage, and SSI revives after $t = 1$ Myr because the interaction between shocks is weak and each behaves as a single shock wave when two shocks are distant. To understand the stabilizing mechanism, we show B_y and v_y maps for higher growth rate model 2S-evenB24 in Figure 4.15. The left column shows v_y maps. The red lines are contours of density, and represent initial density perturbation at $t = 0$ Myr and shock fronts at $t > 0$ Myr. The black lines represent the streamlines of the magnetic field. Note that these streamlines are not real magnetic field lines because we plot them with the B_y emphasized. We can confirm the sign of B_y and v_y change with time, indicating that magnetic field lines oscillation results in the creation and annihilation of the perturbed magnetic field just behind the shock fronts. We conclude that the magnetic tension stabilizes the even mode SSI.

4.3.4 Non-linear Evolution of Two-shocks SSI

We focus on studying the nonlinear evolution for the odd mode SSI since the even mode SSI is stable (see §4.3.3). As a result of colliding flow, a filament forms at the center $x \simeq 0$ pc. In Figure 4.19, we show the density maps for model NL2Shockλ0.05 at time $t = 0.04$, 0.2, and 0.4 Myr (from top to bottom). White lines represent magnetic field lines. To compare with no SSI case, we simulate a one-dimensional case and show the density profile in Figure 4.21. Panel (a) and (b) show the result for the ideal MHD case and non-ideal MHD case, respectively. We find that turbulence is not generated, but the width of the shocked layer becomes wider than no SSI case (1D case, see panel [a] in Figure 4.21) considering the coarse visualization by observations. In Figure 4.20, we show density maps for model NL2ShockRand as a general case. We can confirm that the smaller-scale SSI grows fast. Here also, the turbulent structure does not arise.

Considering the growth of the shock position fluctuation is slowed down for the case of one-shock SSI including ambipolar diffusion, we can expect that the growth rate will also be low in two-shocks SSI including ambipolar diffusion case.

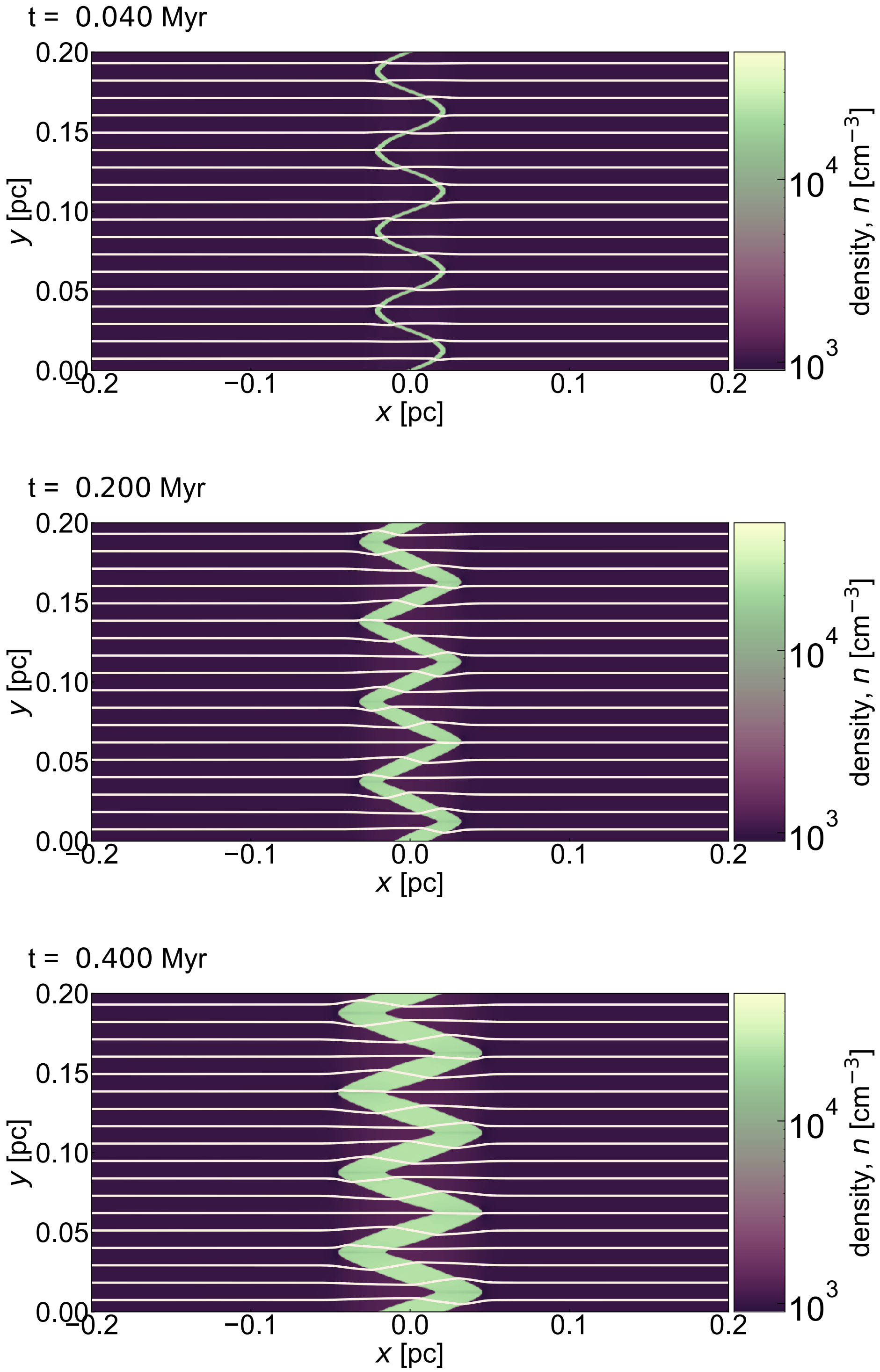

Figure 4.19: Density maps in the result of model NL2Shockλ0.05 at time t = 0.04, 0.2, and 0.4 Myr (from top to bottom). White lines represent the contour of the vector potential i.e., magnetic field lines.

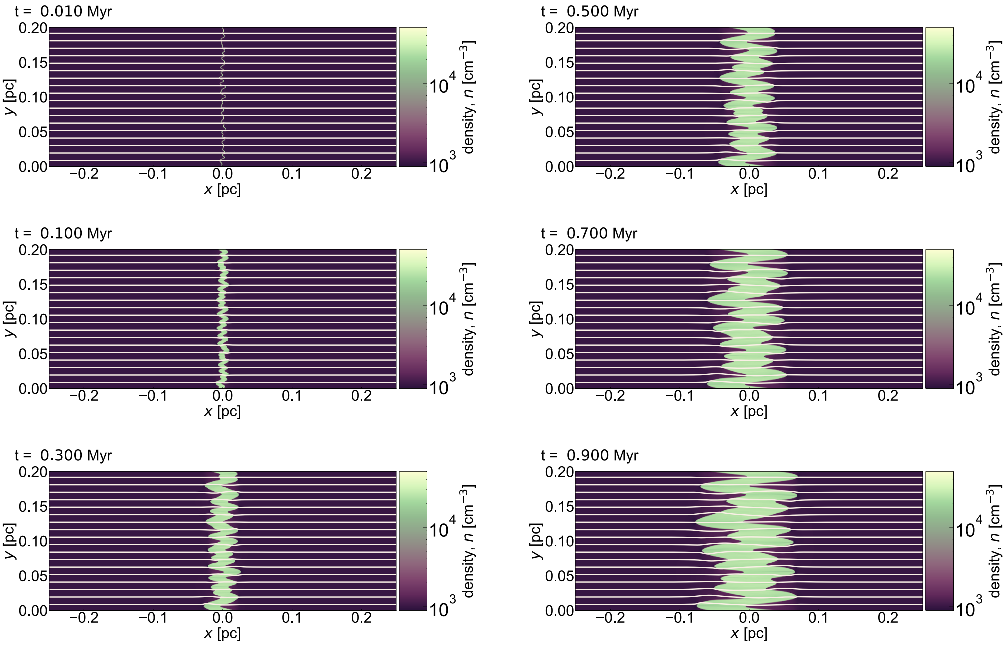

Figure 4.20: Density maps in the result of model NL2ShockRand at time $t = 0.04$, 0.1, 0.3, 0.5, 0.7, and 0.9 Myr. White lines represent magnetic field lines.

However, we find a mechanism of faster expansion than the one-shock case. In Figure 4.22, we show density maps for model NL2Shockλ0.05AD. Compared to Figure 4.19, the expanding speed of the shocked layer is more prominent. The mechanism of the fast expansion is following. Ambipolar diffusion permits the flow along the shock fronts, leading to gas accumulation and dense blobs forming in valleys. The blobs move towards the center of the shocked layer and hit the other shock front, i.e., momentum transportation occurs (see the central panel in Figure 4.23). Then, the magnitude of corrugation grows and new dense blobs are created in new valleys. We summarize this mechanism in Figure 4.24.

For the small $\lambda_{\rm p} = 0.01$ pc $< \ell_{\rm damp}$ model NL2Shockλ0.01AD, the instability survives contrary to the one-shock case because the momentum transportation is driven rather by ambipolar diffusion. At $t = 0.2 - 0.4$ Myr, longer modes different from the initial $\lambda_{\rm p}$ we set becomes prominent. This may be because the Kelvin Helmholtz instability occurs at a small scale in the shocked region and disturbs the momentum transportation. At $t = 0.6 - 0.8$ Myr, the shocked layer shrink temporally. Long modes of $\simeq 0.1$ pc start to grow at $t = 0.8$–1.4 Myr. For a more general case, we show the result with a random perturbation case (model NL2ShockRandAD). Similar to the result for model NL2Shockλ0.01AD, small-scale finger structures dominate at the initial stage ($t < 0.3$ Myr), and the larger-scale finger becomes outstanding at the later stage ($t > 0.7$ Myr)

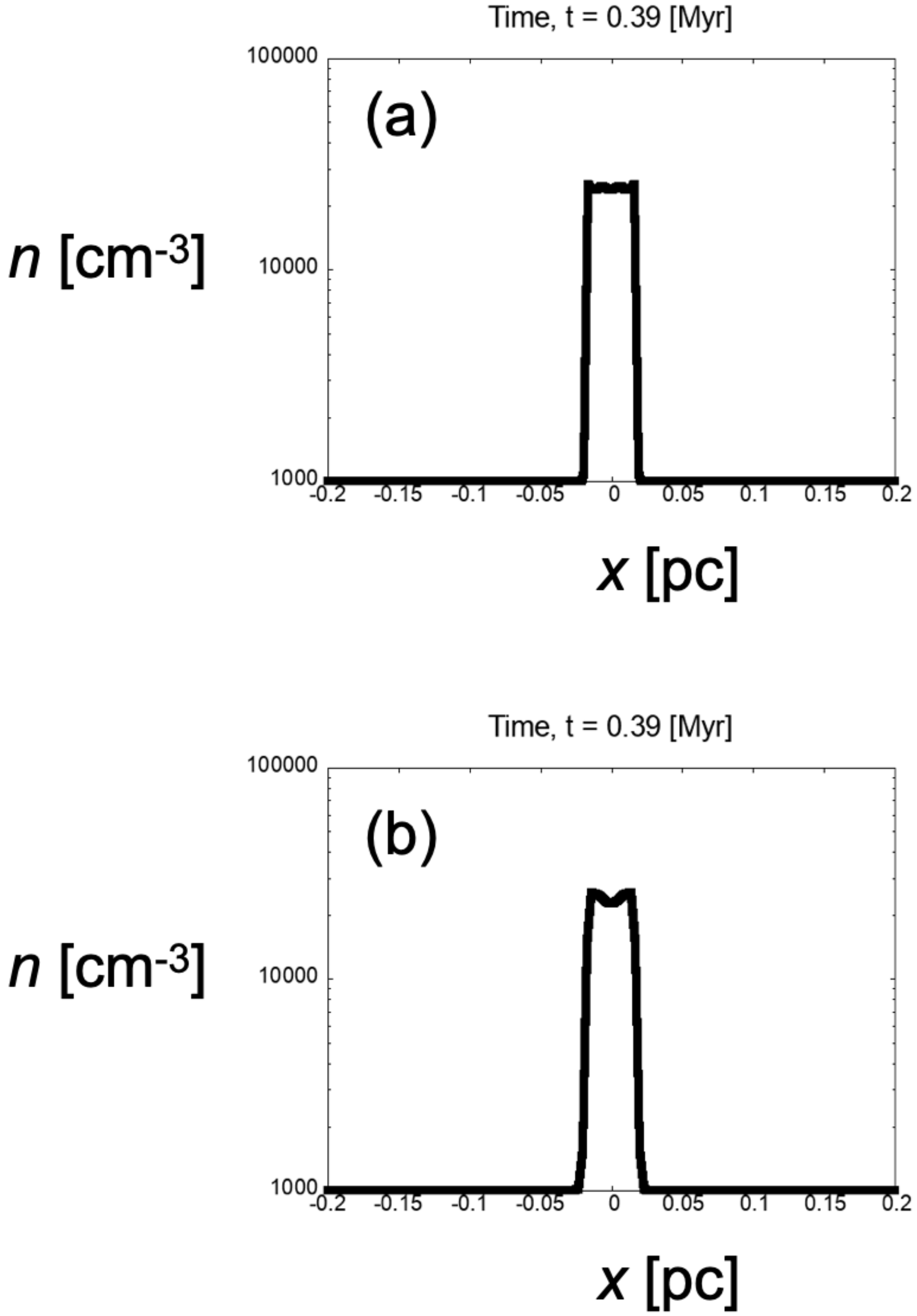

Figure 4.21: Density profile for one-dimensional simulation of slow shock. The initial condition is the same as model NL2Shockλ0.05 but calculated only on the x-axis. Note that SSI does not occur in this situation. *Panel (a)*: Result for ideal MHD case. *Panel (b)*: Same as the panel (a) but ambipolar diffusion is included.

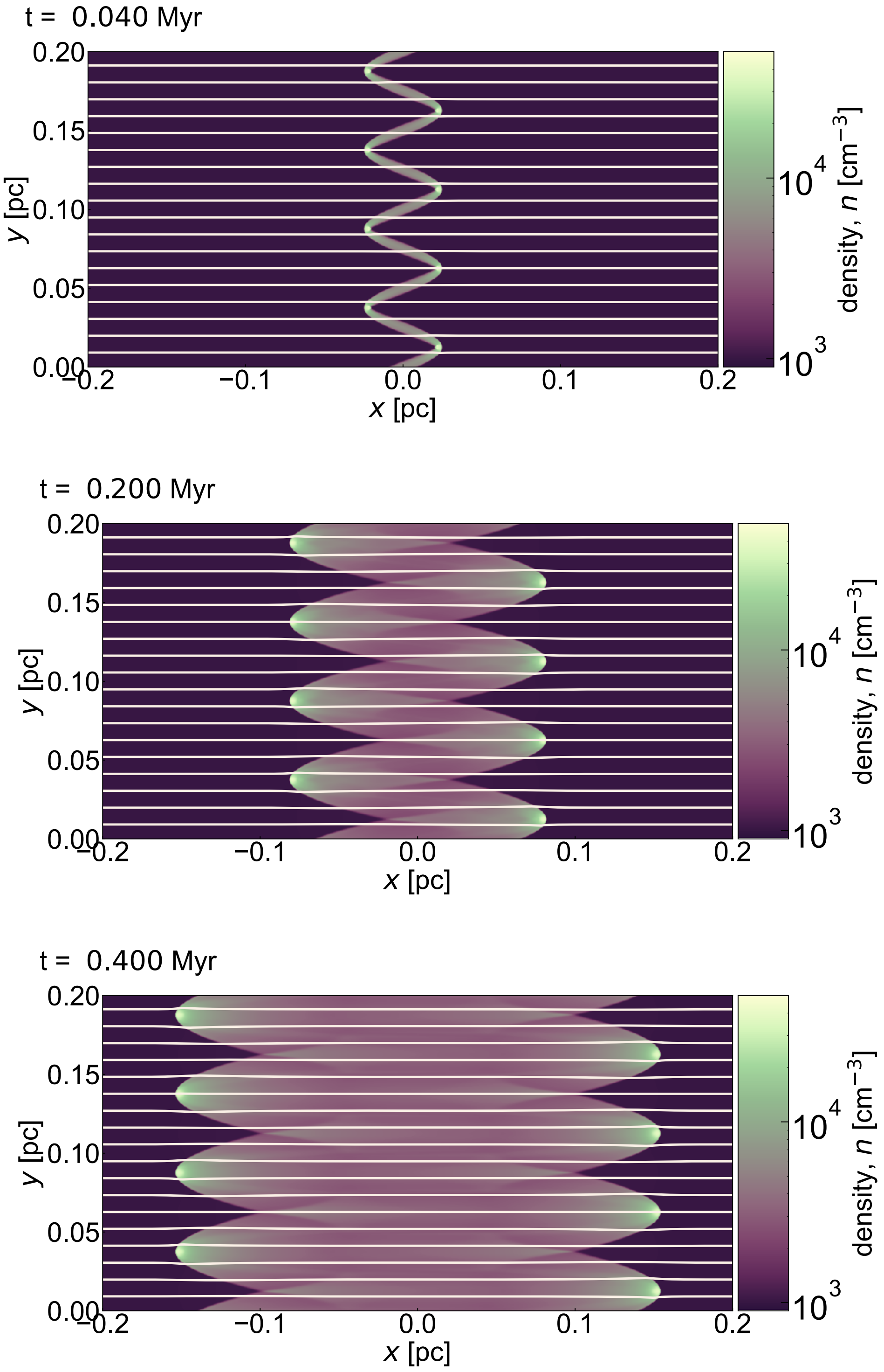

Figure 4.22: Density maps in the result of model NL2Shockλ0.05AD at time $t = 0.04$, 0.2, and 0.4 Myr (from top to bottom). White lines represent magnetic field lines.

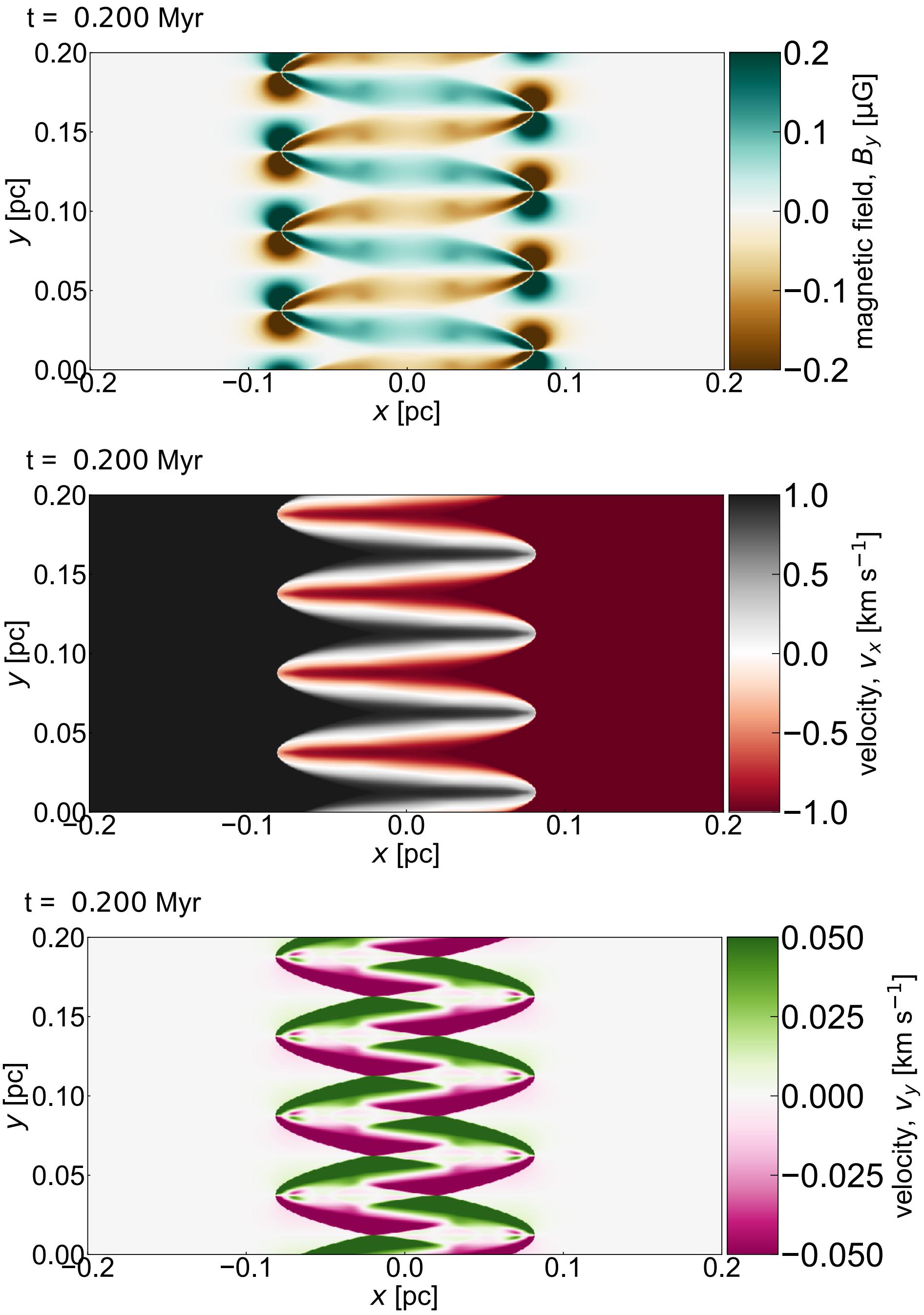

Figure 4.23: B_y, v_x, and v_y maps in the result of model NL2Shockλ0.05AD at time t = 0.2 Myr (from top to bottom).

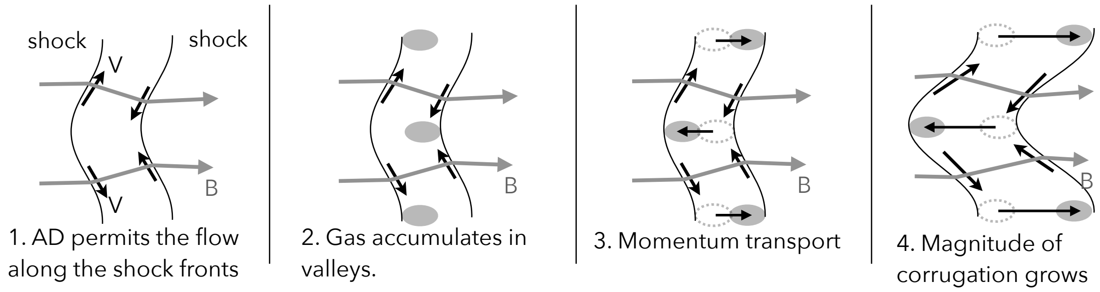

Figure 4.24: Schematic illustration of the mechanism of fast expansion driven by the nonlinear effect of two-shocks SSI including ambipolar diffusion.

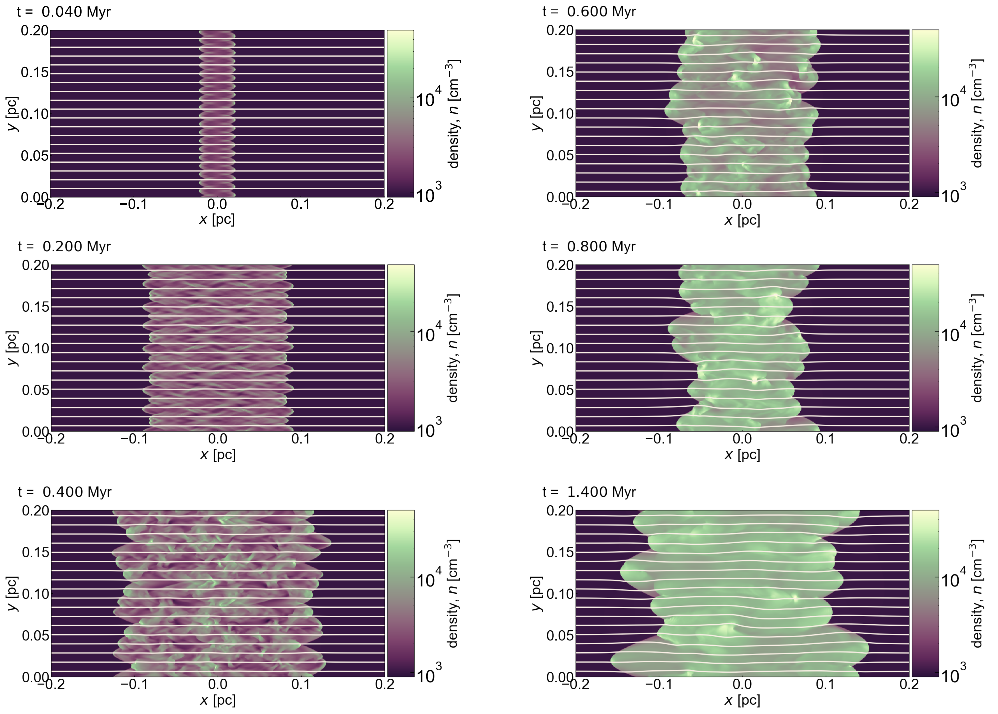

Figure 4.25: Density maps in the result of model NL2Shockλ0.01AD at time $t = 0.04$, 0.2, 0.4, 0.6, 0.8, and 1.4 Myr.

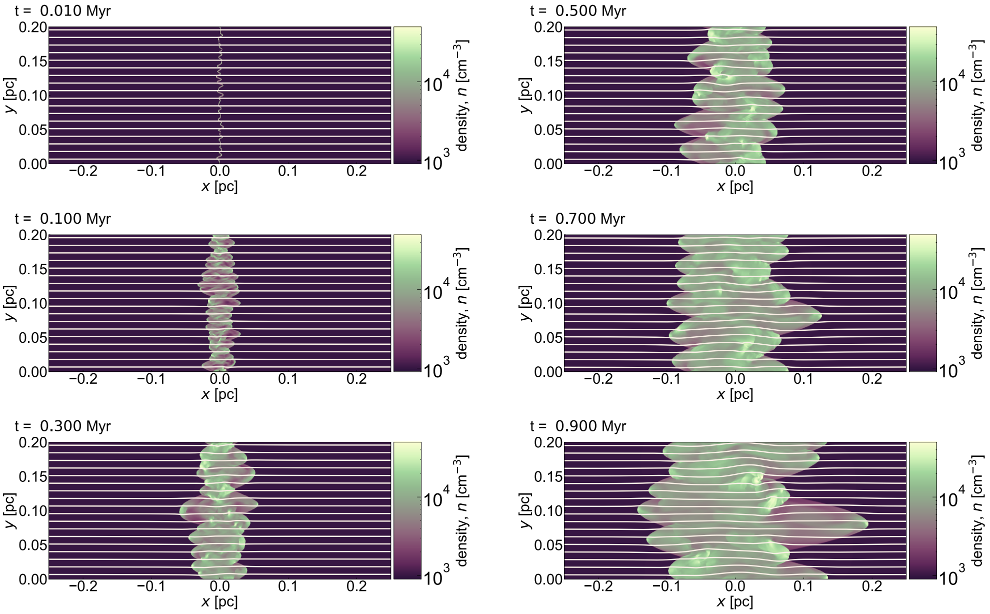

Figure 4.26: Density maps in the result of model NL2ShockRandAD at time $t = 0.04$, 0.1, 0.3, 0.5, 0.7, and 0.9 Myr.

4.3.5 Three-dimensional simulation including self-gravity

The left panels in Figure 4.27 show snapshots of the column density map of the result of three-dimensional SSI simulation including self-gravity and ambipolar diffusion at t = 0.4, 0.7, 1.0, and 1.30 Myr. The nonlinear evolution of SSI including ambipolar diffusion generates turbulence in the filament leading to fine structure formation. We show a three-dimensional density structure in Figure 4.28. A lot of finger structures (dark blue and light blue) and dense blobs (light blue) created by the instability are observed.

The right panels in Figure 4.27 are the same as the left panels in Figure 4.27 but for maps taken a smoothing of the column density using the Gaussian kernel function of a width of 0.01 pc, corresponding to the typical beam width for *Herschel* Gould Belt survey (Arzoumanian et al., 2013). We examine the column density structure and the width of the filament by computing the median along the filament smoothed by the Gaussian kernel function. The red lines in Figure 4.29 represent median radial column density profiles of the right side ($x > 0$ pc) of the filament. The dashed lines are Plummer function whose parameters are given by ($R_{\rm flat} =$ 0.017 pc, $p = 1.6$) for the left panel and ($R_{\rm flat} = 0.013$ pc, $p = 1.8$) for the right panel. The black solid lines show half of the Full-width half maximum FWHM/2, i.e., the radius of the filament (solid lines). We can confirm that the median radial column density profiles are well described by the Plumnner function. Note that the amount of the gas at $x > 0.2$ pc (the right edge of the red lines) decreases due to self-gravity and the boundary condition. We measure the line mass of the filament by tracing the dense region (> 8000 cm^{-3}) in our simulation box, and $M_{\rm line} \simeq 57\ M_\odot$ pc^{-1} at $t = 1$ Myr and $M_{\rm line} \simeq 75\ M_\odot$ pc^{-1} at $t = 1.3$ Myr. As we

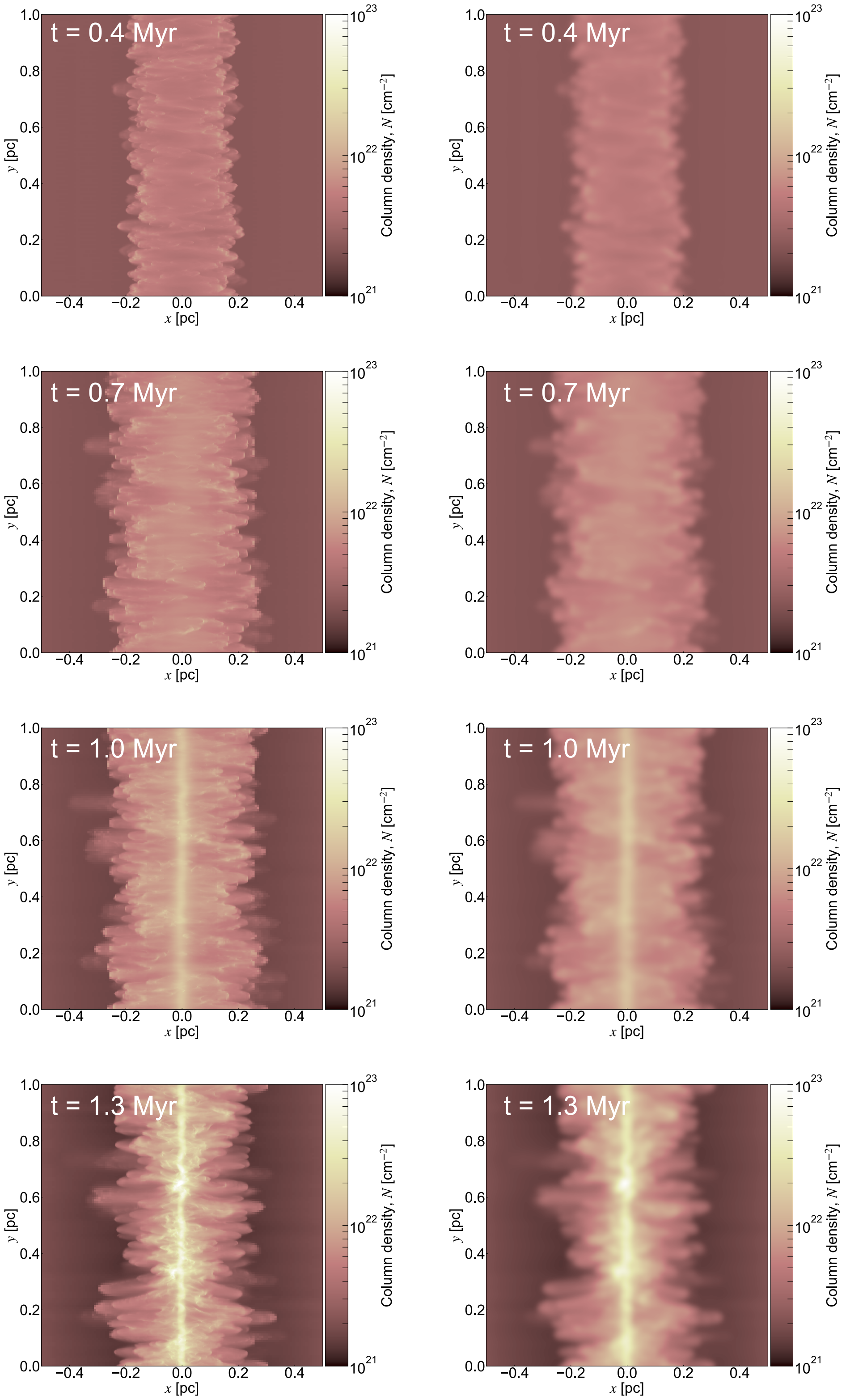

Figure 4.27: *Left column*: Column density maps result from three-dimensional SSI simulation including self-gravity and ambipolar diffusion at time t = 0.4, 0.7, 1.0, and 1.3 Myr (from top to bottom). *Right column*: Same as the left column panels but for maps taken a smoothing of the column density using the Gaussian kernel function of a width of 0.01 pc, corresponding to the typical beam width for *Herschel* Gould Belt survey (Arzoumanian et al., 2013).

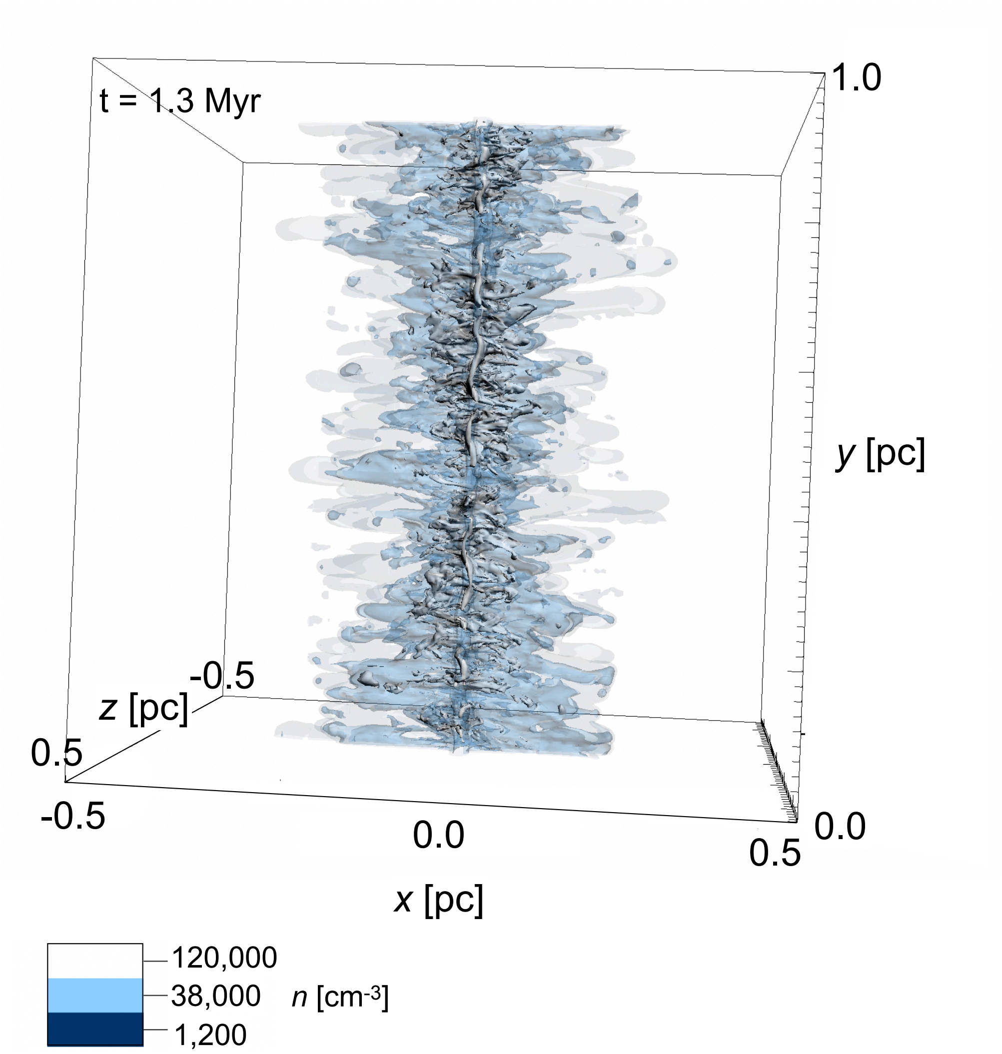

Figure 4.28: Density contour result from three-dimensional SSI simulation including self-gravity and ambipolar diffusion at time $t = 1.3$ Myr. The color bar represents the density magnitude.

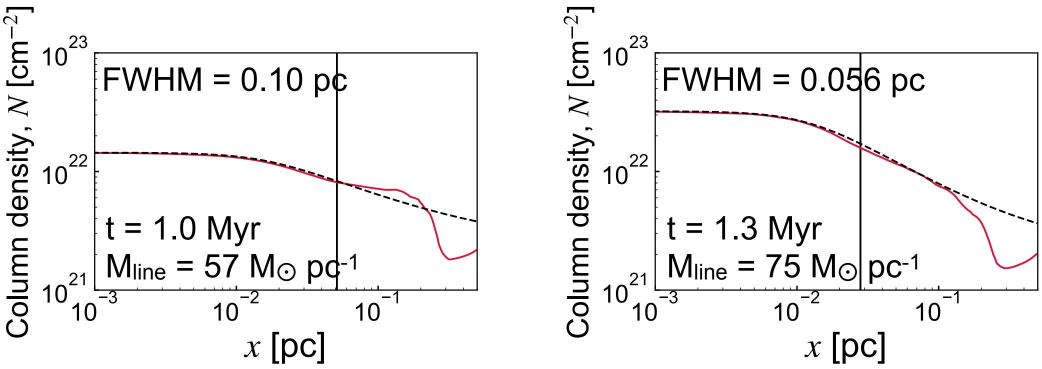

Figure 4.29: Median radial column density profile of right side ($x > 0$ pc) of the filament (red lines), Plummer function whose parameters given by ($R_{\rm flat} = 0.017$ pc, $p = 1.6$) for the left panel and ($R_{\rm flat} = 0.013$ pc, $p = 1.8$) for the right panel (dashed lines), and half of Full width half maximum FWHM/2, i.e., the radius of the filament (solid lines).

introduced in 1.2.4 and 1.2.4, Observations showed that most filaments have the slope index of $p = 1.5$–2.5 and the width of $\simeq 0.1$ pc. Our results are consistent with them even for massive filament ($M_{\rm line} \simeq 57$–$75\ M_\odot\ {\rm pc}^{-1}$). The estimated critical line mass including magnetic field (Eq. [1.18]) is given by

$$\begin{aligned} M_{\rm line,cr,B} &\simeq 11 \left(\frac{w}{0.1{\rm pc}}\right)\left(\frac{B}{50\mu{\rm G}}\right) M_\odot{\rm pc}^{-1} + 15 \left(\frac{c_s}{0.2\ {\rm km\ s}^{-1}}\right)^2 M_\odot{\rm pc}^{-1} \\ &= 26\ M_\odot{\rm pc}^{-1}, \end{aligned} \tag{4.29}$$

which is lower than our filament formed in the simulation, i.e., our filament is magnetically (and thermally) supercritical. Therefore, we propose that the nonlinear evolution of SSI including ambipolar diffusion induces an additional pressure to support the filament against gravitational collapse.

4.4 Discussion

4.4.1 Parameter dependence of damping scale

In §4.3.1, we have stated that the most unstable scale depends on the magnetic field, density, and shock velocity. In this section, we discuss how the characteristic of the SSI is scaled. In Figure 4.30, we show the damping length scale, which scales with the most unstable length, as a function of the initial density (panel a), the initial magnetic field (panel b), and the shock velocity (panel c). The grey dotted line is the scale of ambipolar diffusion evaluated in post-shock quantities which can be written as

$$\ell_{\rm AD,post} \equiv \frac{B_1^2}{4\pi\gamma_{\rm in}C\rho_1^{3/2}v_1} \simeq \frac{B_0^2 c_{\rm s}}{4\pi\gamma_{\rm in}C\rho_0^{3/2}v_0^2} = 0.017\,{\rm pc}\left(\frac{B_0}{30\ \mu{\rm G}}\right)^2\left(\frac{n_0}{10^3\ {\rm cm}^{-3}}\right)^{-3/2}\left(\frac{v_0}{1\ {\rm km/s}}\right)^{-2}, \tag{4.30}$$

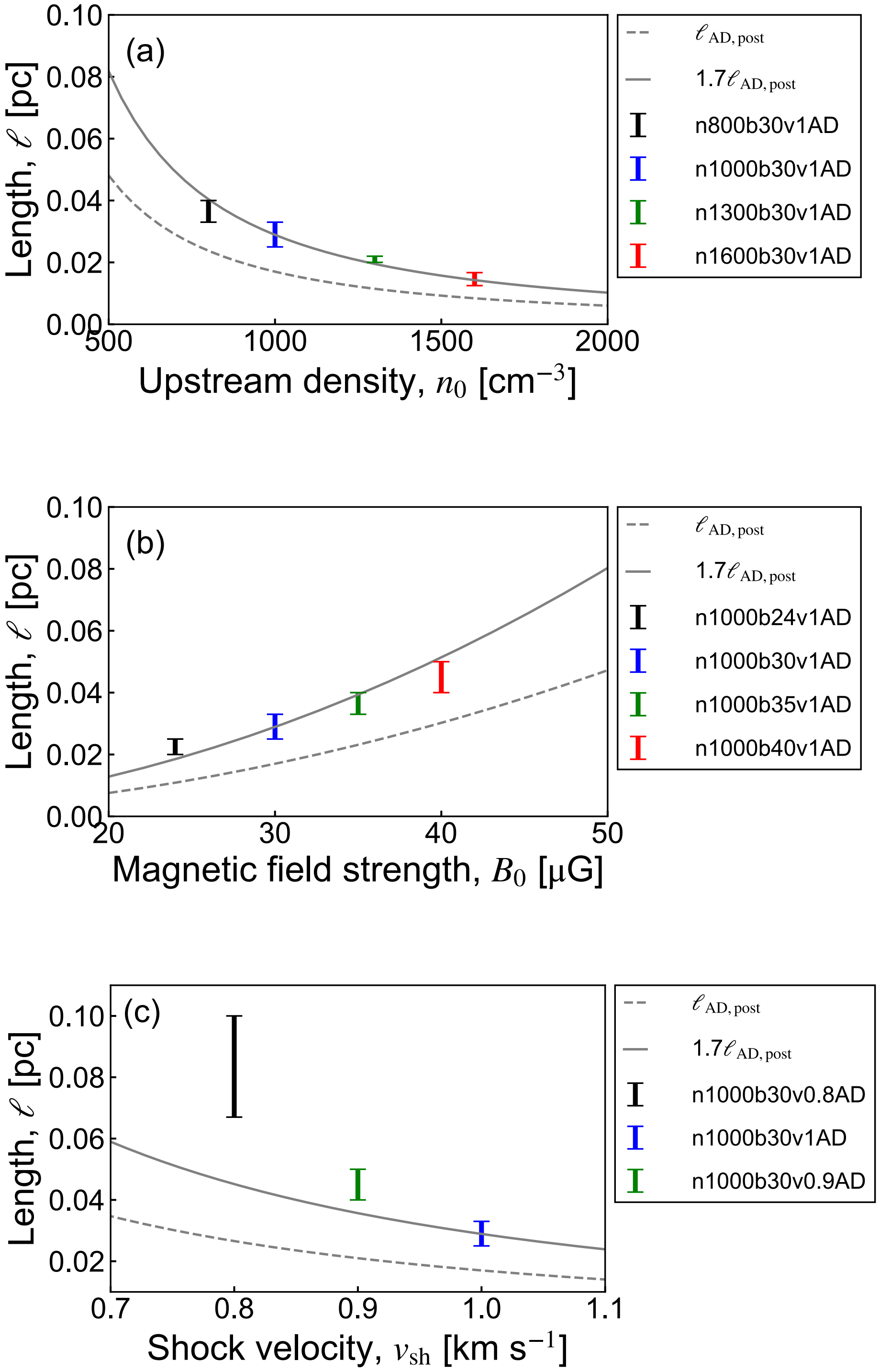

Figure 4.30: Parameter dependence of damping scale $\ell_{\rm damp}$ (solid vertical lines). The grey dashed and solid lines represent $\ell_{\rm AD,post}$ (see, eq. 4.30) and $1.7\ell_{\rm AD,post}$. (a) Upstream density versus damping scale. (b) Magnetic field versus damping scale. (c) Shock velocity versus damping scale.

where, $B_1 \simeq B_0$, $\rho_1 \simeq \mathcal{M}_{\rm s}^2\rho_0$, and $v_1 \simeq \mathcal{M}_{\rm s}^{-2}v_0$ are post-shock magnetic field strength, density, and velocity, respectively. The grey solid line represents $1.7 \times \ell_{\rm AD,post}$. The top and bottom edges of vertical lines are the minimum lengths with a positive growth rate and the maximum lengths with a negative growth rate, i.e., the vertical lines show the range in which the damping scale exists. For panels (a) and (b), the damping length scale well follows $1.7\ell_{\rm AD,post}$. For the shock velocity dependence, the dependency is not as good as n_0 and B_0, but the difference from $1.7\ell_{\rm AD,post}$ is within a factor of 2. Thus we conclude that the characteristic damping scale of the SSI can be approximately estimated by $\ell_{\rm damp} \sim 1.7\ell_{\rm AD,post}$, and the most unstable scale by $\ell_{\rm SSI} \sim 5\ell_{\rm damp} \sim 9\ell_{\rm AD,post}$.

4.4.2 Growth rate of two shocks SSI including ambipolar diffusion

To understand the property of the nonlinear two shocks SSI including ambipolar diffusion, we compare the results for model NLλ0.05AD and NLλ0.05ADξ0.005. We can confirm the expanding speed of the shocked layer depends on ξ, indicating that the shock angle is one of the key parameters to determine the expanding speed.

4.4.3 Why could a massive filament maintain a width of 0.1 pc?

In §4.3.5, the massive filament can maintain a width of 0.1 pc. We discuss why filament width could be kept. Nonlinear evolution of SSI including ambipolar diffusion drives the motion of dense gas blob from the inside of the filament toward the surface of the filament. We estimate velocity dispersion and the ram pressure of the dense blob. From simulation data, the filament has the velocity dispersion of $\simeq 0.2$ km s^{-1} (which is consistent with observations by Arzoumanian et al. (2013)), thus effective critical line mass (Eq. [1.17, 1.18]) is given by

$$\begin{aligned}
M_{\rm line,crit} &\simeq 0.24\frac{Bw}{G^{1/2}} + 1.66\frac{c_s^2 + \Delta v^2}{G} \\
&\simeq 12\left(\frac{w}{0.1\ \mathrm{pc}}\right)\left(\frac{B}{50\ \mu\mathrm{G}}\right) \\
&+ 15\left(\frac{c_s^2}{0.2\ \mathrm{km}\ ^{\mathrm{s}^{-1}}}\right) + 15\left(\frac{\Delta v^2}{0.2\ \mathrm{km}\ ^{\mathrm{s}^{-1}}}\right)\ \mathrm{M}_\odot\ \mathrm{pc}^{-1} \\
&= 42\ \mathrm{M}_\odot\ \mathrm{pc}^{-1}, \qquad (4.31)
\end{aligned}$$

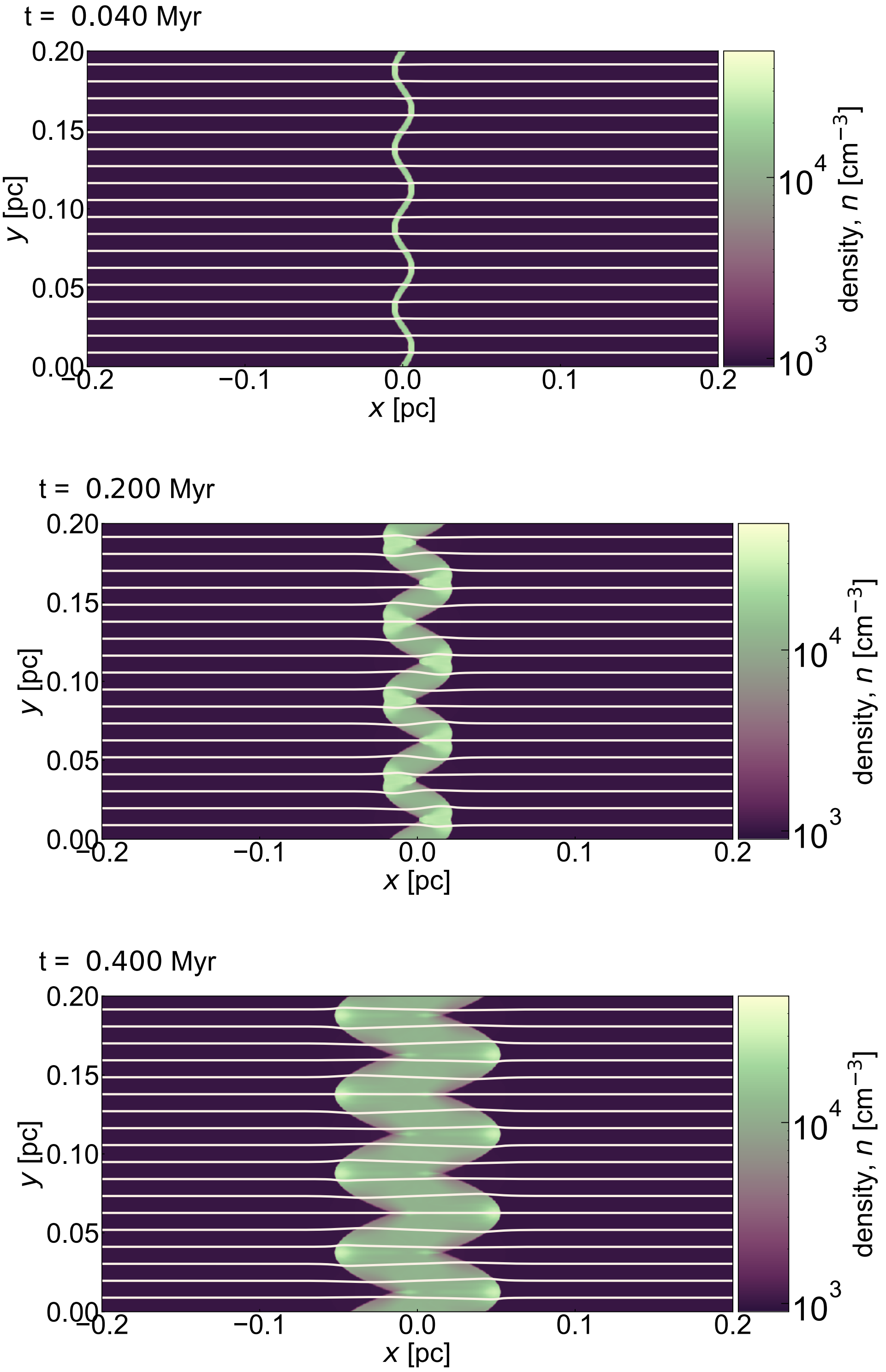

Figure 4.31: Density maps in the result of model NL2Shockλ0.05ADξ0.005 at time t = 0.04, 0.2, and 0.4 Myr (from top to bottom). White lines represent the contour of the vector potential i.e., magnetic field lines.

which is not enough to support a massive filament whose line mass of ~ 100 $\mathrm{M}_\odot$ pc^{-1}. If we use the ram pressure of blob in the filament,

$$\begin{aligned}
M_{\rm line,crit} &\simeq 0.24\frac{Bw}{G^{1/2}} + 1.66\frac{c_s^2 + \Delta v^2}{G} \\
&\simeq 12\left(\frac{w}{0.1\ \mathrm{pc}}\right)\left(\frac{B}{50\ \mu\mathrm{G}}\right) \\
&+ 15\left(\frac{c_s^2}{0.2\ \mathrm{km\ ^{s^{-1}}}}\right) + 94\left(\frac{v_{\rm blob}^2}{0.5\ \mathrm{km\ ^{s^{-1}}}}\right)\ \mathrm{M}_\odot\ \mathrm{pc}^{-1} \\
&= 121\ \mathrm{M}_\odot\ \mathrm{pc}^{-1}. \qquad (4.32)
\end{aligned}$$

If the line mass of the filament is half the critical value of the critical value and the effect of external pressure is taken into account, the width becomes around 0.1 pc (Fischera & Martin, 2012). In a conclusion, we conclude that additional pressure given by the instability works as a widening mechanism of filament width. It should be noted that we need to further investigate whether it is always 0.1 pc.

4.5 Summary

We have performed the SSI simulations in molecular clouds using isothermal ($\gamma = 1.01$) or adiabatic ($\gamma = 5/3$) using Athena++. To test the optimal solver for solving SSI, we performed simulations using HLLD, LHLLD, HLLE, and Roe solvers to decide which solver is the best for solving SSI by comparison with the approximated analytic solution (Eqs. 1.23). The stabilization length scale of SSI in molecular clouds by ambipolar diffusion was investigated. We also study the nonlinear evolution of SSI and the effect of ambipolar diffusion on it. Furthermore, we performed a three-dimensional simulation including self-gravity and ambipolar diffusion. Our main findings are as follows.

1. HLLD, LHLLD, and Roe solvers with physical kinetic viscosity are most suitable for simulating SSI. Simulations using HLLD/LHLLD solvers could cause unphysical explosions depending on the initial condition. Although such a numerical effect can be quenched using physical viscosity, we select the Roe solver as an optimal one in Athena++.

2. Ambipolar diffusion suppresses SSI on a small scale. We find that the most unstable scale of the order of ~ 0.1 pc and the damping scale of the order of ~ 0.01 pc in molecular clouds.

3. The most unstable and damping length scales depend on the density, shock velocity, and, magnetic field strength. The scaling is roughly described by $\ell_{\rm SSI} \sim 5\ell_{\rm damp} \sim 9\ell_{\rm AD,post} \propto B_0^2 \rho^{-3/2} v_{x0}^{-2}$.

4. Even/odd mode is stable/unstable for two-shocks SSI. The growth rate for the odd mode is similar to the single shock case.

5. Two shocks SSI for ideal MHD does not generate turbulence, however, turbulence (dense blob motion in a filament) is driven if we introduce ambipolar diffusion.

6. The turbulence gives additional pressure leading to the maintenance of filament width against gravitational collapse in three-dimensional simulation. Furthermore, the column density profile was also consistent with observations.

Chapter 5

Conclusion

Filament formation and evolution in molecular clouds determine the initial condition for star formation. However, there are unsolved problems. We tried to solve the following problems.

1. Theoretical research suggests that shock waves in molecular clouds trigger filament formation. Since several different mechanisms have been proposed for filament formation, the formation mechanism of the observed star-forming filaments requires clarification.

2. Previous studies have demonstrated that strong MHD shock compression allows for the formation of massive cores. However, these studies implicitly assumed a long duration of a shock wave (corresponding to collisions between large clouds). On the other hand, some studies demonstrated that gravitationally bound cores do not form in the case of short duration. Therefore, a systematic study into the effect of shock duration on the resulting filament/core formation is required.

3. Observations show that a massive star cluster formation occurs where the peak of gas column density in a cloud exceeds 10^{23} cm^{-2}. However, the physical origin of the threshold peak column density of 10^{23} cm^{-2} is unknown.

4. Observations show that the filament width takes the universal value of 0.1 pc regardless of their line-mass, even supercritical filaments subject to gravitational collapse. Theoretically, however, the width should shrink for the supercritical filaments.

In Chap. 2, we tackled the problem 1. We performed a series of isothermal MHD simulations of filament formation. We focused on the influences of shock velocity and turbulence on the formation mechanism and identified three different mechanisms for filament formation. The results indicate that when the shock is fast, at shock velocity $v_{\rm sh} = 7$ km s^{-1}, the Type O mechanism substantially works. However, at a slow shock velocity $v_{\rm sh} = 2.5$ km s^{-1}, Type C mechanism becomes important. When both the shock velocities and turbulence are low, Type G becomes important for filament formation. Moreover, we analyzed the line-mass distribution of the filaments and showed that strong shock waves can naturally create high-line-mass filaments such as those observed in the massive star-forming regions in a short time. We conclude that the dominant filament formation mode changes with the velocity of the shock wave triggering the filament formation. The filament formation mechanism is understood in a unified way by this work.

In Chap. 3, we investigated the effect of the shock-compressed layer duration on filament/star formation and how the initial conditions of massive star formation are realized, which leads to solving problems 2 and 3. We performed three-dimensional (3D) isothermal MHD simulations with gas inflow duration from the boundaries (i.e., shock wave duration) as a controlling parameter. Filaments formed behind the shock expand after the duration time for short shock duration models, whereas long-duration models lead to star formation by forming massive supercritical filaments. Moreover, when the shock duration is longer than two postshock free-fall times, the peak column density of the compressed layer exceeds 10^{23} cm^{-2}, and the gravitational collapse of the layer causes the number of OB stars expected to be formed in the shock-compressed layer reaches the order of ten (i.e., massive cluster formation). In this sense, a faster shock wave is advantageous because postshock free-fall time becomes smaller when the shock wave is faster.

In Chap. 4, to solve problem 4, focusing on the slow shock instability (SSI) that occurs at the filament boundaries, we used non-ideal MHD simulations to investigate the mechanism of filament width maintenance. The wavefront of the slow shock is known to be unstable, and we expect the conversion of the accretion flow ram pressure into thermal/turbulent pressure across the unstable shock front that potentially maintains the filament width. However, since the linear dispersion relation obtained from the ideal MHD analysis show infinitesimal scale as the most unstable scale. In the scale of dense filaments, the effect of ambipolar diffusion is non-negligible that expected to suppress the instability at small scales. As a first step, we investigated the linear dispersion relation of the SSI including ambipolar diffusion. We performed two-dimensional MHD simulations to examine the linear stage of the slow shock instability including the effect of the ambipolar diffusion. We found that the most unstable scale of the slow shock instability is given by roughly 5 times the length scale of the ambipolar diffusion calculated using postshock variables.

The filament would be sandwiched between two slow shocks. Although the wavefront of the slow shock is unstable, the stability of the two slow shocks when they are adjacent has not been investigated. Two adjacent slow shocks are expected to interact via magnetic field lines. As the second step, we aimed to understand the interaction between two adjacent slow shocks. The results show that the odd mode is as unstable as the single slow shock, the growth rate is the same as the single shock case, and the even mode is stabilized by magnetic tension.

Furthermore, as the third step, we aimed to explain the universality of the filament width and investigated whether slow shock instability with ambipolar diffusion causes turbulence generation using two-dimensional non-ideal MHD simulations. We found that turbulence is driven as a result of the nonlinear evolution of the slow shock instability with bipolar diffusion. As the final step, we also performed 3D simulations with self-gravity to investigate the radial profile of the column density. For a massive filament of about 70 $M_{\odot}$ pc^{-1}, the profile is consistent with observations and has a width of 0.06 pc. We proposed that the width is maintained by turbulent pressure driven by slow shock instability with ambipolar diffusion.

Appendix A

Procedure for Derivation of Slow Shock Instability

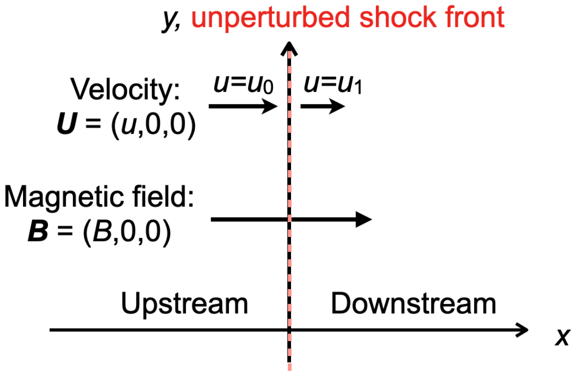

Figure A.1: Flow configuration.

In this appendix, we show the detailed derivation of the slow shock instability based on Lessen & Deshpande (1967) and Édel'Man (1989). Basic equations of isothermal MHD are given by

$$\rho \frac{\partial \mathbf{U}}{\partial t} + U \cdot \nabla U = -\nabla p - \nabla \left(\frac{B^2}{8\pi} \right) + \frac{1}{4\pi} (\mathbf{B} \cdot \nabla) \mathbf{B}, \tag{A.1}$$

$$\frac{\partial \rho}{\partial t} + \nabla \cdot (\rho \mathbf{v}) = 0, \tag{A.2}$$

$$\frac{\partial \mathbf{B}}{\partial t} = \nabla \times (\mathbf{v} \times \mathbf{B}), \tag{A.3}$$

and

$$p = \rho c_{\mathrm{s}}^2. \tag{A.4}$$

Because we consider a situation in a boundary of star-forming filament, the unperturbed gas flow, and magnetic field are set to be perpendicular to the shock wave (see Figure A.1). The steady-state jump conditions at $x = 0$ are given by

$$\langle \rho u \rangle = 0, \tag{A.5}$$

$$\langle B_x \rangle = 0, \tag{A.6}$$

and

$$\left\langle \rho u^2 + p \right\rangle = 0, \tag{A.7}$$

where $\langle \cdots \rangle$ and $\hat{n}_k$ denotes the jump in the quantity across the shock and the components of the unit normal $\hat{n}$ along the x_k axis. These equations are the same as unmagnetized fluid. When a shock wave moves with a velocity of W, these jump conditions are rewritten as

$$-\langle \rho \rangle W + \langle \rho U_i \rangle \hat{n}_i = 0 \tag{A.8}$$

$$\langle B_i \rangle \hat{n}_i = 0 \tag{A.9}$$

$$-\langle \rho U_i \rangle W + \langle \rho U_k U_i \hat{n}_k \rangle = -\left\langle p + \frac{B^2}{8\pi} \right\rangle \hat{n}_i + \frac{1}{4\pi} \langle B_i B_k \rangle \hat{n}_k \tag{A.10}$$

$$-\langle B_i \rangle W + \langle B_i U_k - B_k U_i \rangle \hat{n}_k = 0 \tag{A.11}$$

We set perturbations as follows.

$$\begin{aligned} \delta u &= f \exp\left[i \left(k_x x + k_y y - \omega t\right)\right] \\ \delta v &= \Phi \exp\left[i \left(k_x x + k_y y - \omega t\right)\right] \\ \delta B_x &= b_x \exp\left[i \left(k_x x + k_y y - \omega t\right)\right] \\ \delta B_y &= b_y \exp\left[i \left(k_x x + k_y y - \omega t\right)\right] \\ \delta \rho &= n \exp\left[i \left(k_x x + k_y y - \omega t\right)\right] \\ \delta p &= c_{\mathrm{s}}^2 \delta \rho, \end{aligned} \tag{A.12}$$

where k_x, k_y, and ω are x and y components of wave number and the frequency of disturbance, respectively. The linear equations can be written as

$$\omega_{\mathrm{L}} n + \rho \left(k_x f + k_y \Phi\right) = 0 \tag{A.13}$$

$$\omega_{\mathrm{L}} \rho f + k_x \pi = 0 \tag{A.14}$$

$$\omega_{\mathrm{L}} \rho \Phi + k_y \pi + (B/4\pi) \left(k_y b_x - k_x b_y\right) = 0 \tag{A.15}$$

$$\omega_{\mathrm{L}} b_x + k_y B \Phi = 0 \tag{A.16}$$

$$\omega_{\mathrm{L}} b_y - k_x B \Phi = 0 \tag{A.17}$$

$$k_x b_x + k_y b_y = 0 \tag{A.18}$$

where, $\omega_{\mathrm{L}} \equiv -\omega + k_x u$. To find a non-trivial solution to these equations, taking the determinant of coefficients to be zero, we get the dispersion relation

$$\omega_{\mathrm{L}}^4 - \omega_{\mathrm{L}}^2 \left(k_x^2 + k_y^2\right) \left(c_{\mathrm{s}}^2 + v_{\mathrm{A}}^2\right) + \left(k_x^2 + k_y^2\right) k_x^2 v_{\mathrm{A}}^2 c_{\mathrm{s}}^2 = 0, \tag{A.19}$$

where, $v_{\mathrm{A}} \equiv B/\sqrt{4\pi\rho}$. While the component of the wave number vector along the shock wave, k_y, is the same on both upstream and downstream, the perpendicular component k_x is different on different sides. These values are obtained from A.19. The eigenvalue obtained from the second factor of Eq. A.19 corresponds to magneto-acoustic waves. The shock wave is said to be unstable if there exists a disturbance vanishing at $x = \pm\infty$ and such that Im $\omega > 0$. It is assumed that k_y is real. The boundary condition requires that Im $k_x < 0$ ahead of the shock and Im $k_x > 0$ behind the shock. Since the solutions of the Eq. A.19 are complex, we solve it by applying approximation of $\mathcal{M}_{\mathrm{A}} \ll 1$ and $\omega/(k_y u) \ll 1$. (Édel'Man, 1989). Multiplying $\mathcal{M}_{\mathrm{A}}^2 (k_y u)^4/\omega^4$ Eq. A.19 by , we obtain

$$(-\Omega + l)^4 - (-\Omega + l)^2 \left(l^2 + l\right)\left(M_s^{-2} + M_A^2\right) + \left(l^2 + 1\right) l^2 \mathcal{M}_A^{-2} \mathcal{M}_s^{-2} = 0 \quad \text{(A.20)}$$

where, $\Omega \equiv \omega/(k_y u)$ and $l \equiv k_x/k_y$. An upstream solution that does not diverge at infinity is $k_x = -ik_y$. Solutions in downstream are $k_x = ik_y$ and $k_x = \Omega k_y/(1 + \mathcal{M}_1)$.

The eigen functions for a magneto-acoustic wave are given by

$$f = -\frac{c_{\mathrm{s}}^2 k_x}{\omega_{\mathrm{L}}} \frac{n}{\rho} \quad \text{(A.21)}$$

$$\Phi = -\frac{c_{\mathrm{s}}^2 k_y \omega_{\mathrm{L}}^2}{\omega_{\mathrm{L}} \left[\omega_{\mathrm{L}}^2 - \left(k_x^2 + k_y^2\right) v_{\mathrm{A}}^2\right]} \frac{n}{\rho} \quad \text{(A.22)}$$

$$b_x = \frac{c_{\mathrm{s}}^2 k_y^2 B_x}{\omega_{\mathrm{L}}^2 - \left(k_x^2 + k_y^2\right) v_{\mathrm{A}}^2} \frac{n}{\rho} \quad \text{(A.23)}$$

$$b_y = -\frac{c_{\mathrm{s}}^2 k_y k_x B_x}{\omega_{\mathrm{L}}^2 - \left(k_x^2 + k_y^2\right) v_{\mathrm{A}}^2} \frac{n}{\rho} \quad \text{(A.24)}$$

The surface of the perturbed shock is written as

$$\xi = \eta \exp\left(ik_y y - i\omega t\right). \quad \text{(A.25)}$$

This leads to the shock velocity normal to itself,

$$W = -i\omega\xi. \quad \text{(A.26)}$$

Note that the shock amplitude η is small. The unit normal vector to the perturbed surface is given by $\hat{n}_k = (1, -ik_y\xi)$. Using these equations and the shock jump condition, we can obtain the jump condition for the perturbation

$$i\left\langle \rho\omega - k_y \rho v \right\rangle \xi + \left\langle \rho f + un \right\rangle = 0 \quad \text{(A.27)}$$

$$\left\langle b_x \right\rangle = 0 \quad \text{(A.28)}$$

$$\left\langle 2\rho u f + u^2 n + \pi \right\rangle = 0 \quad \text{(A.29)}$$

$$i\left\langle -k_y \rho \left(v^2 + c_{\mathrm{s}}^2\right)\right\rangle \xi + \left\langle \rho u \Phi - \frac{B_x b_y}{4\pi} \right\rangle = 0 \quad \text{(A.30)}$$

$$\langle -B_x\Phi + u b_y \rangle = 0 \tag{A.31}$$

Substituting the eigen functions to Eq. A.28 and A.31, we can confirm that Eq. A.28 and A.31 are identical, i.e., there are four independent equations.

A solution of the density perturbation can be written as a superposition of each eigen function. For the slow shock, the solutions upstream and downstream are given by

$$n_0 = n_0^{(\mathrm{f})} \exp\left(ik_{x_{\mathrm{fast0}}} x\right), \tag{A.32}$$

and

$$n_1 = n_1^{(\mathrm{f})} \exp\left(ik_{x_{\mathrm{fast1}}} x\right) + n_1^{(\mathrm{s})} \exp\left(ik_{x_{\mathrm{slow1}}} x\right). \tag{A.33}$$

Substituting the eigen functions and Eq. A.32 and A.33 to the perturbed shock jump condition, the perturbed jump condition can be written as the following form

$$\|S_{ij}\| \begin{vmatrix} n_1^{(f)} \\ n_2^{(f)} \\ n_2^{(s)} \\ \eta \end{vmatrix} = 0 \tag{A.34}$$

where $\|S_{ij}\|$ is a 4×4 matrix. The determinant of S_{ij} gives a non-trivial solution, that is dispersion relation of slow shock instability.

Appendix B

High Shock Velocity Simulations

B.1 High Shock Velocity Case with Strong Turbulence

In the model v12GyTy, the velocity dispersion of the turbulence is set to 1 km s^{-1}. In this appendix, we investigate the filament formation mechanism and the distribution of the angle between the filament and the magnetic field lines in the case of larger velocity dispersion of the initial turbulence $\Delta v = 2$ km s^{-1} as model 'v12GyTy'. Panels (I)-(III) and (i)-(iii) in Figure B.1 show column density snapshots of model v12GyTy2 in the y-z and x-y planes at $t = 0.2$ Myr, 0.4 Myr, and 0.8 Myr, respectively. We can confirm that stronger turbulence makes the structure more complex than the results in model v12GyTy. To clarify the dominant filament formation mechanism, we show the local density cross-sections around the five major filaments as the results of models v12GyTy2 in Figure B.2. The snapshots show that turbulent motion parallel to the magnetic field (y-direction) create dense clamps in the pre-shock region[1] that are swept by the shock and induces type O filament formations. The curved shock morphology and velocity vectors (black arrows) shown in the cross-section panels in model v12GyTy2 support the activation of the type O mechanism.

We show angle histograms of model v12GyTy2 at $t = 0.2$ (panels a and b), 0.4 (panels c and d), and 0.8 (panels e and f) Myr in Figure B.3. Left panels (a), (c), and (e) are the angle histograms for the filaments in the column density range of 0.5 $\bar{N}_{\mathrm{sh}}$ to 1.5 $\bar{N}_{\mathrm{sh}}$. Right panels (b), (d), and (f) are the histograms for the filaments with $N > 1.5\ \bar{N}_{\mathrm{sh}}$. While dense filaments are perpendicular to the magnetic field, the distribution of the angle between the faint filament and the magnetic field is random and different from that in Figure 2.14. Remarkably, the histograms of the angle distribution are much flatter than the case of model v12GyTy (see, Fig. B.3). This may be because, when the initial turbulence is strong, various filamentation modes are mixed and the resulting filamentary structure changes its direction to the magnetic field lines. Observational study of density structure and magnetic field orientations in several molecular clouds by Planck Collaboration

---

[1] This resembles type C filament formation, but this process happens before shocked sheet formation, and thus preshock clumps are formed.

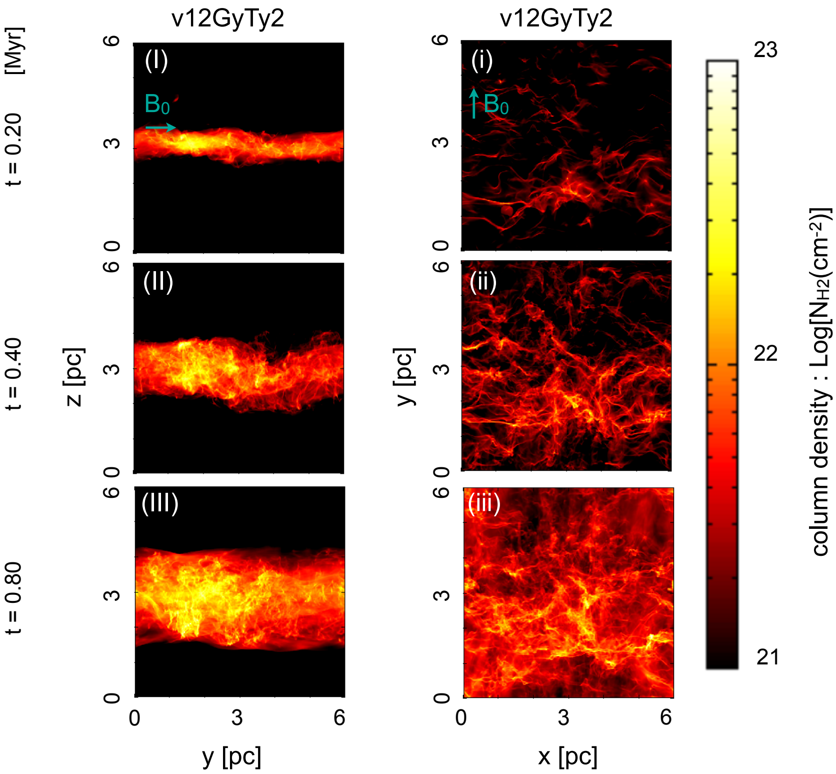

Figure B.1: Column density maps at time $t = 0.2$ (*top*), 0.4 (*middle*), and 0.8 (*bottom*) Myr. *Left row* (panels I, II, and III): Column density in the y-z plane of model v12GyTy2. *Right row* (panels i, ii, and iii): Same as the panels (I)-(III) but for the x-y plane.

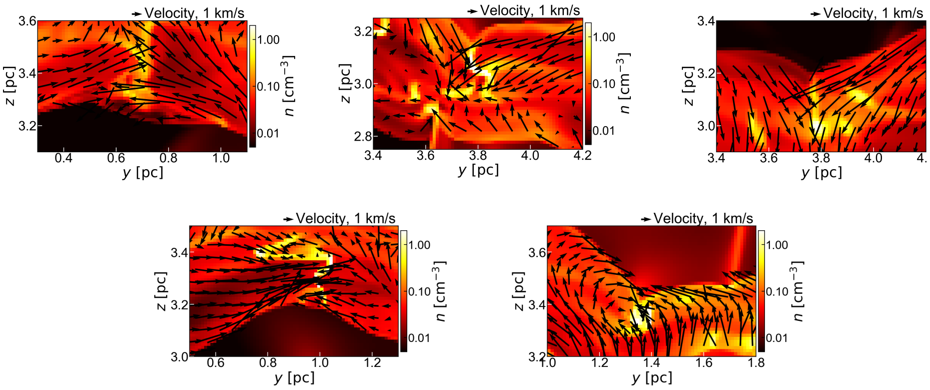

Figure B.2: Cross-section maps of the number density in the y-z plane of model v12GyTy2. The yellow blobs located roughly at the center of each panel correspond to cross-sections of the filaments. We can confirm that the oblique MHD shock compression mechanism takes a major role in filament formation even in the case of initial stronger turbulence with high shock velocity.

XXXV (2016) does not show such a flat distribution. Therefore, we conclude that this kind of initial strong turbulence model does not provide a realistic model.

B.2 High Shock Velocity Case without Magnetic Field

In this section, we describe the additional set of calculations without a magnetic field. The compression ratio of the isothermal hydrodynamics shock is given by $R \sim \mathcal{M}_{\rm s}^2$, where $\mathcal{M}_{\rm s}$ is the sonic Mach number. Thus, for instance, if we set $v_{\rm sh} = 7.0$ (or 2.5) km s^{-1}, the compression ratio becomes 1225 (or 156), which is extremely high. Note that, with the magnetic field, the compression ratio is dramatically reduced to $R \sim \sqrt{2}\mathcal{M}_{\rm A}$, where $\mathcal{M}_{\rm A}$ is the Alfvénic Mach number.

Here, we chose parameter $v_{\rm coll} \sim 8.0$ km s^{-1} ($v_{\rm sh} \sim 5$ km s^{-1}), which we call v8GnTnB0. Panels a and b in Figure B.4 show column density snapshots of model v8GnTnB0 in the y-z at $t = 0.3$ Myr, and 1.0 Myr, respectively. In contrast to other column density figures in the main text, we integrate the whole numerical domain in constructing the column density. In panel b, we see the highly unstable feature of shock surfaces. This seems to be nonlinear thin-shell instability (Vishniac, 1994), which is known to be suppressed in the case of a magnetic field. A similar feature is observed in previous similar studies (e.g., Folini et al., 2014). In both panels, compressed layers sandwiched by two shocks

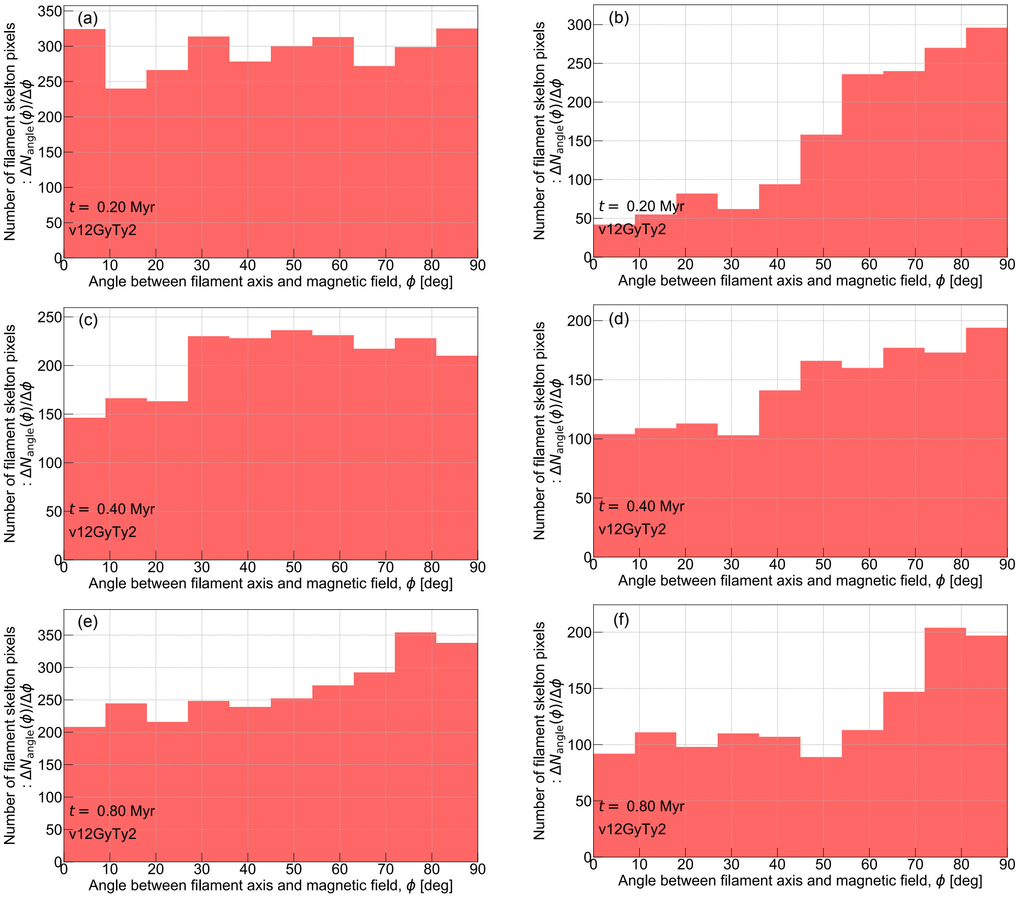

Figure B.3: Histogram of angles between filaments and magnetic field for model v12GyTy2. From top to bottom, results at time $t=$ 0.2, 0.4, and 0.8 Myr, respectively. *Left panels* (1), (3), and (5): Results when we identify filaments in the column density range of $0.5\bar{N}_{\mathrm{sh}}$ to $1.5\bar{N}_{\mathrm{sh}}$. *Right panels* (2), (4), and (6): Results when the filament identification threshold column density is chosen to be $1.5\bar{N}_{\mathrm{sh}}$.

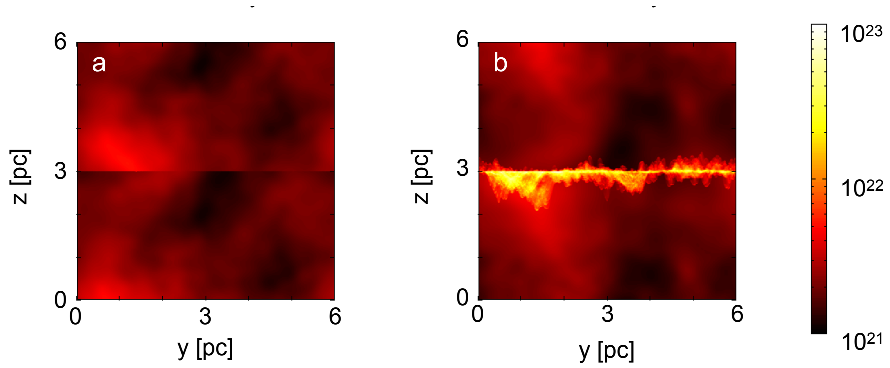

Figure B.4: Column density maps at time $t = 0.3$ ($panel a$), and 1.0 ($panel b$) Myr in the y-z plane of model v8GnTnB0.

are extremely thin and dense, which has not been observationally identified in the actual molecular clouds associated with fast shock waves as far as we are aware. Under this high compression, the length scale of the initial fluctuations becomes smaller than the spatial resolution, and thus, the smallest scale structures shown in this section are limited by numerical resolution. Nonetheless, we can identify no sign of the formation of the filamentary structure with a sufficiently large line-mass. Therefore, we think that this setup without a magnetic field is not realistic and the presence of magnetic fields is critical for creating filamentary structures in the shock-compressed region.

Appendix C

Selection of MHD solver

In Figure C.1 and C.2, we show snapshots of the density and pressure map of models n1000b30v1.3a$\mathcal{R}\infty$D and n1000b30v1.3a$\mathcal{R}\infty$LD, respectively. For long term simulations using HLLD/LHLLD without the physical shear viscosity, numerical errors around the shock front cause unphysical numerical explosions, which do not appear for simulations with Roe scheme. This numerical problem occurs if the denominator $\rho_\alpha \left(S_\alpha - u_\alpha\right)\left(S_\alpha - S_M\right) - B_x^2$ in Eq. (44)-(47) of Miyoshi & Kusano (2005) closes to zero. The latest Athena++ has been designed to prevent this issue to some extent, but it cannot prevent the unphysical explosion under the initial conditions dealt with in this study. Although such a numerical effect can be quenched by physical viscosity, we chose the Roe solver with physical shear viscosity for the safety of long-term integration.

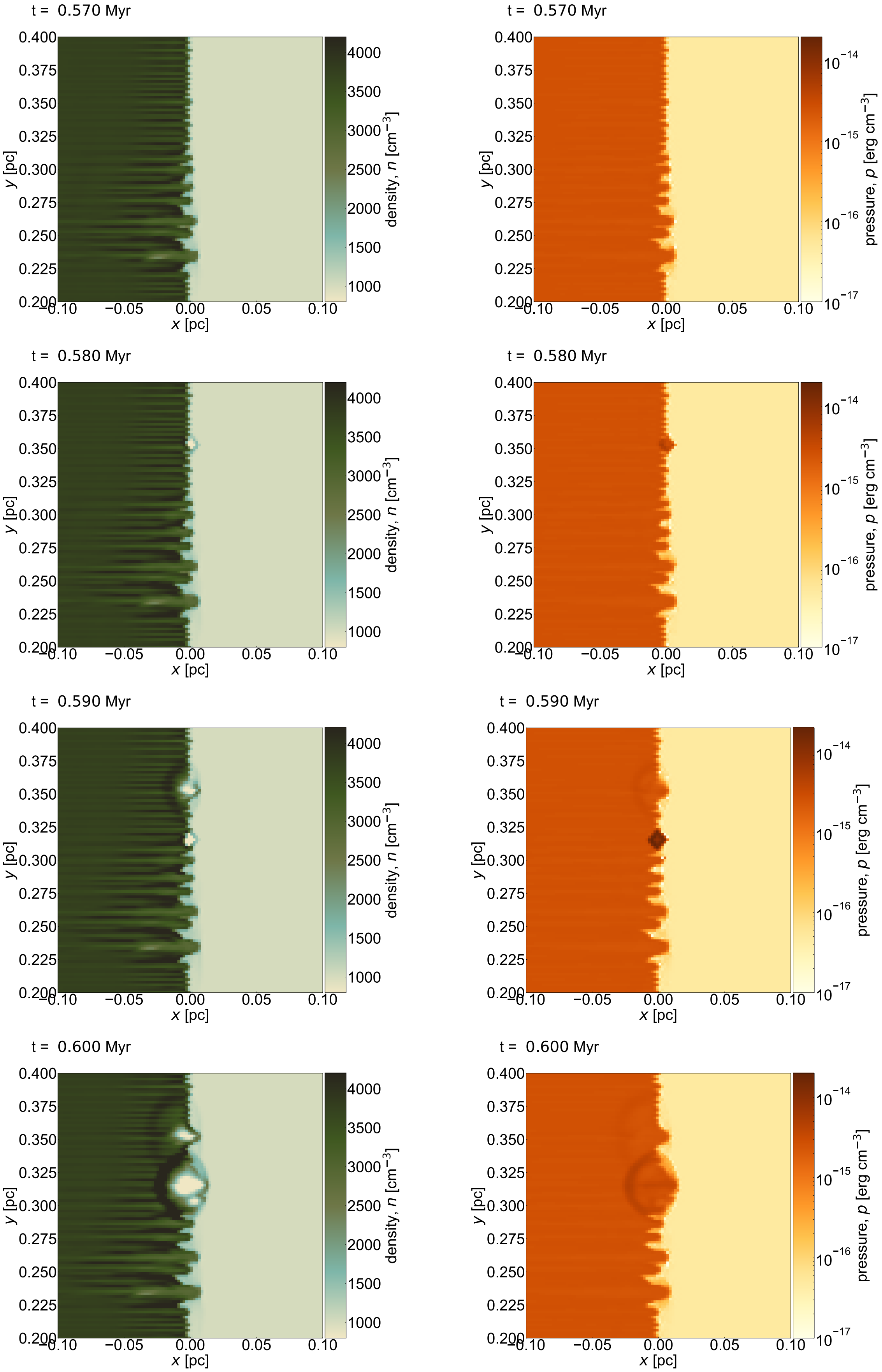

Figure C.1: Density (left row) and pressure (right row) maps in the result of model n1000b30v1.3a at time t = 0.57, 0.58, 0.59, and 0.60 Myr (from top to bottom).

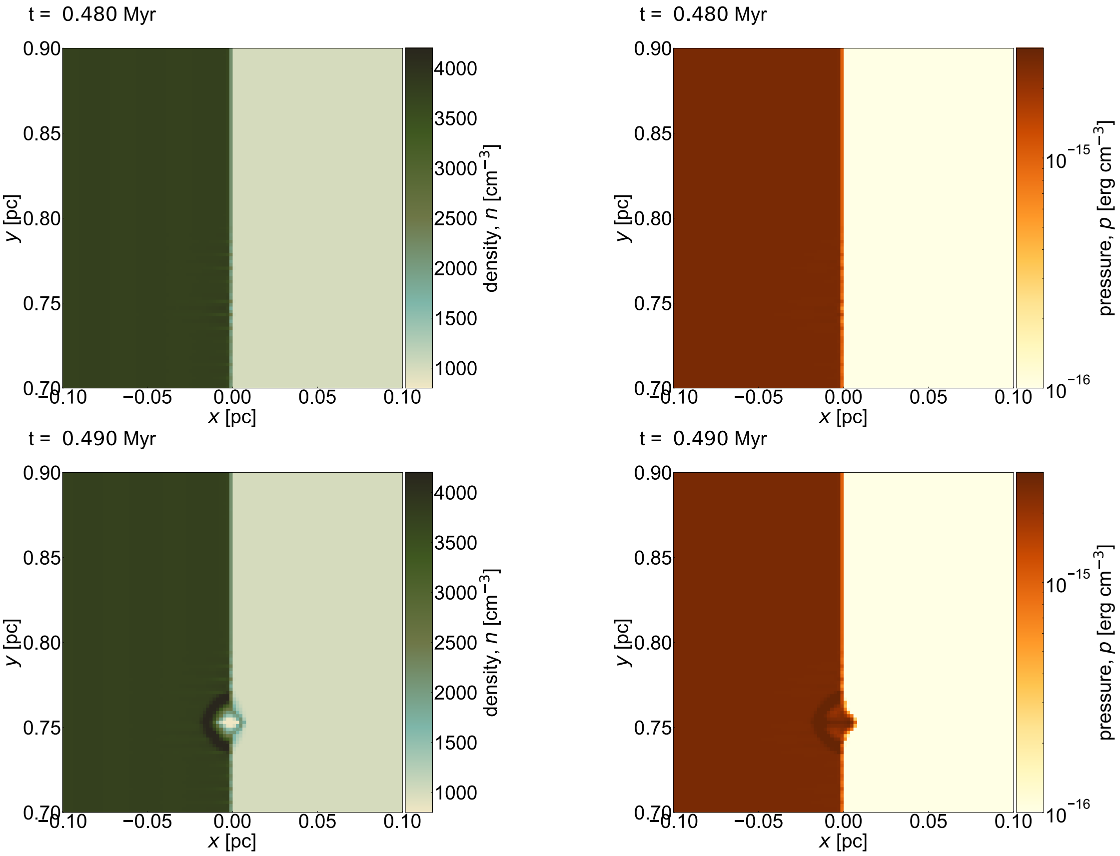

Figure C.2: Density (left row) and pressure (right row) maps in the result of model n1000b30v1.3a at time $t = 0.57$, 0.58, 0.59, and 0.60 Myr (from top to bottom).

References

Abe D., Inoue T., Inutsuka S.-i., Matsumoto T., 2021, ApJ, 916, 83

André P., et al., 2010, A&A, 518, L102

André P., Di Francesco J., Ward-Thompson D., Inutsuka S. I., Pudritz R. E., Pineda J. E., 2014, in Beuther H., Klessen R. S., Dullemond C. P., Henning T., eds, Protostars and Planets VI. p. 27

André P., Arzoumanian D., Könyves V., Shimajiri Y., Palmeirim P., 2019, Astron. Astrophys., 629, 1

Arzoumanian D., et al., 2011, A&A, 529, L6

Arzoumanian D., André P., Peretto N., Könyves V., 2013, A&A, 553, A119

Arzoumanian D., Shimajiri Y., Inutsuka S., Inoue T., Tachihara K., 2018, PASJ, 70, 96

Arzoumanian D., et al., 2019, A&A, 621, A42

Auddy S., Basu S., Kudoh T., 2016, ApJ, 831, 46

Balfour S. K., Whitworth A. P., Hubber D. A., Jaffa S. E., 2015, MNRAS, 453, 2471

Balfour S. K., Whitworth A. P., Hubber D. A., 2017, MNRAS, 465, 3483

Beresnyak A., Lazarian A., Cho J., 2005, ApJ, 624, L93

Bonne L., et al., 2020, A&A, 644, A27

Bonnell I. A., Vine S. G., Bate M. R., 2004, MNRAS, 349, 735

Bontemps S., et al., 2010, Astron. Astrophys., 518, 3

Chandrasekhar S., Fermi E., 1953, ApJ, 118, 113

Chen C.-Y., 2015, PhD thesis, pp 1–212

Chen C. Y., Ostriker E. C., 2014, ApJ, 785

Chen C.-Y., Mundy L. G., Ostriker E. C., Storm S., Dhabal A., 2020, MNRAS, 494, 3675

Chira R. A., Kainulainen J., Ibáñez-Mejía J. C., Henning T., Mac Low M. M., 2018, A&A, 610, A62

Clarke S. D., Whitworth A. P., Hubber D. A., 2016, MNRAS, 458, 319

Clarke S. D., Whitworth A. P., Duarte-Cabral A., Hubber D. A., 2017, MNRAS, 468, 2489

Crutcher R. M., 2012, ARA&A, 50, 29

Davis L., 1951, Physical Review, 81, 890

Dedner A., Kemm F., Kröner D., Munz C. D., Schnitzer T., Wesenberg M., 2002, JCoPh, 175, 645

Draine B. T., Roberge W. G., Dalgarno A., 1983, ApJ, 264, 485

Édel'Man M. A., 1989, Astrophysics, 31, 758

Elmegreen B. G., Scalo J., 2004, ARA&A, 42, 211

Enoch M. L., Glenn J., Evans Neal J. I., Sargent A. I., Young K. E., Huard T. L., 2007, ApJ, 666, 982

Enokiya R., Torii K., Fukui Y., 2021, PASJ, 73, S75

Federrath C., 2016, MNRAS, 457, 375

Federrath C., Roman-Duval J., Klessen R. S., Schmidt W., Mac Low M. M., 2010, A&A, 512, A81

Field G. B., 1965, ApJ, 142, 531

Fischera J., Martin P. G., 2012, A&A, 542, A77

Folini D., Walder R., Favre J. M., 2014, A&A, 562, A112

Fukui Y., et al., 2016, ApJ, 820, 26

Fukui Y., et al., 2019, ApJ, 886, 14

Fukui Y., Habe A., Inoue T., Enokiya R., Tachihara K., 2020, arXiv e-prints, p. arXiv:2009.05077

Fukui Y., Habe A., Inoue T., Enokiya R., Tachihara K., 2021, PASJ, 73, S1

Goodman A. A., Pineda J. E., Schnee S. L., 2009, ApJ, 692, 91

Heigl S., Burkert A., Gritschneder M., 2018, MNRAS, 474, 4881

Heigl S., Gritschneder M., Burkert A., 2020, MNRAS, 495, 758

Heiles C., Crutcher R., 2005, Cosm. Magn. Fields, pp 137–182

Hennebelle P., 2013, A&A, 556, A153

Hennebelle P., Inutsuka S., 2019, Frontiers in Astronomy and Space Sciences, 6, 5

Henshaw J. D., Caselli P., Fontani F., Jiménez-Serra I., Tan J. C., 2014, MNRAS, 440, 2860

Heyer M. H., Brunt C. M., 2004, ApJ, 615, L45

Inoue T., Fukui Y., 2013, ApJ, 774, L31

Inoue T., Inutsuka S.-i., 2009, ApJ, 704, 161

Inoue T., Inutsuka S., 2012a, ApJ, 759, 35

Inoue T., Inutsuka S.-i., 2012b, ApJ, 759, 35

Inoue T., Inutsuka S., 2016, ApJ, 833, 10

Inoue T., Inutsuka S.-i., Koyama H., 2006, ApJ, 652, 1331

Inoue T., Yamazaki R., Inutsuka S.-i., Fukui Y., 2012, ApJ, 744, 71

Inoue T., Hennebelle P., Fukui Y., Matsumoto T., Iwasaki K., Inutsuka S.-i., 2018, PASJ, 70, S53

Inutsuka S., 2001, ApJ, 559, L149

Inutsuka S., Miyama S. M., 1992a, ApJ, 388, 392

Inutsuka S.-I., Miyama S. M., 1992b, ApJ, 388, 392

Inutsuka S., Miyama S. M., 1997, ApJ, 480, 681

Inutsuka S.-i., Inoue T., Iwasaki K., Hosokawa T., 2015, A&A, 580, A49

Kandori R., et al., 2020a, ApJ, 892, 128

Kandori R., et al., 2020b, ApJ, 900, 20

Kashiwagi R., Tomisaka K., 2021, ApJ, 911, 106

Kim S.-s., Kim C., Rho O.-H., Kyu Hong S., 2003, Journal of Computational Physics, 185, 342

Kitsionas S., Whitworth A. P., 2007, MNRAS, 378, 507

Klessen R. S., Hennebelle P., 2010, A&A, 520, A17

Kobayashi M. I. N., Inoue T., Tomida K., Iwasaki K., Nakatsugawa H., 2022, arXiv e-prints, p. arXiv:2203.00699

Koch E. W., Rosolowsky E. W., 2015, MNRAS, 452, 3435

Könyves V., et al., 2010, Astron. Astrophys., 518, 1

Könyves V., et al., 2015, A&A, 584, A91

Körtgen B., Soler J. D., 2020, MNRAS, 499, 4785

Koyama H., Inutsuka S., 2000, ApJ, 532, 980

Kroupa P., 2001, MNRAS, 322, 231

Krumholz M. R., McKee C. F., 2008, Nature, 451, 1082

Krumholz M. R., Klein R. I., McKee C. F., Offner S. S. R., Cunningham A. J., 2009, Science, 323, 754

Krumholz M. R., Klein R. I., McKee C. F., 2012, ApJ, 754, 71

Lada C. J., Lombardi M., Alves J. F., 2010, ApJ, 724, 687

Larson R. B., 1981, MNRAS, 194, 809

Lessen M., Deshpande N. V., 1967, Journal of Plasma Physics, 1, 463

Liou M.-S., 2000, Journal of Computational Physics, 160, 623

Matsumoto T., 2007, PASJ, 59, 905

Matsumoto T., Dobashi K., Shimoikura T., 2015, ApJ, 801, 77

Meyer C. D., Balsara D. S., Aslam T. D., 2014, Journal of Computational Physics, 257, 594

Miyama S. M., Narita S., Hayashi C., 1987a, PThPh, 78, 1051

Miyama S. M., Narita S., Hayashi C., 1987b, PThPh, 78, 1273

Miyoshi T., Kusano K., 2005, JCoPh, 208, 315

Molina F. Z., Glover S. C. O., Federrath C., Klessen R. S., 2012, MNRAS, 423, 2680

Nagai T., Inutsuka S.-i., Miyama S. M., 1998, ApJ, 506, 306

Ntormousi E., Hennebelle P., 2019, A&A, 625, A82

Orkisz J. H., et al., 2019, A&A, 624, A113

Osterbrock D. E., 1961, ApJ, 134, 270

Ostriker J., 1964, ApJ, 140, 1056

Padoan P., Nordlund Å., 1999, ApJ, 526, 279

Padoan P., Federrath C., Chabrier G., Evans N. J. I., Johnstone D., Jørgensen J. K., McKee C. F., Nordlund Å., 2014, in Beuther H., Klessen R. S., Dullemond C. P., Henning T., eds, Protostars and Planets VI. p. 77

Palmeirim P., et al., 2013, A&A, 550, A38

Passot T., Vázquez-Semadeni E., 2003, A&A, 398, 845

Peretto N., et al., 2014, A&A, 561, A83

Pineda J. E., et al., 2022, arXiv e-prints, p. arXiv:2205.03935

Planck Collaboration XXXV 2016, A&A, 586, A138

Priestley F. D., Whitworth A. P., 2022, MNRAS, 512, 1407

Pudritz R. E., Kevlahan N. K. R., 2013, Philosophical Transactions of the Royal Society of London Series A, 371, 20120248

Quirk J. J., 1994, International Journal for Numerical Methods in Fluids, 18, 555

Sakre N., Habe A., Pettitt A. R., Okamoto T., 2021, PASJ, 73, S385

Sakre N., Habe A., Pettitt A. R., Okamoto T., Enokiya R., Fukui Y., Hosokawa T., 2022, arXiv e-prints, p. arXiv:2205.07057

Scalo J., Elmegreen B. G., 2004, ARA&A, 42, 275

Seifried D., Walch S., 2015, MNRAS, 452

Shimajiri Y., André P., Ntormousi E., Men'shchikov A., Arzoumanian D., Palmeirim P., 2019, A&A, 632, A83

Shu F. H., 1992, The physics of astrophysics. Volume II: Gas dynamics.

Snow B., Hillier A., 2021, MNRAS, 506, 1334

Soler J. D., Hennebelle P., 2017, A&A, 607, A2

Soler J. D., Hennebelle P., Martin P. G., Miville-Deschênes M. A., Netterfield C. B., Fissel L. M., 2013, ApJ, 774, 128

Stodólkiewicz J. S., 1963, Acta Astron., 13, 30

Stone J. M., Edelman M., 1995, ApJ, 454, 182

Stone J. M., Gardiner T., 2009, New Astron., 14, 139

Stone J. M., Tomida K., White C. J., Felker K. G., 2020, ApJS, 249, 4

Suri S., et al., 2019, A&A, 623, A142

Tahani M., Plume R., Brown J. C., Kainulainen J., 2018, A&A, 614, A100

Tahani M., Plume R., Brown J. C., Soler J. D., Kainulainen J., 2019, A&A, 632, A68

Takahira K., Tasker E. J., Habe A., 2014, ApJ, 792, 63

Tokuda K., et al., 2019, ApJ, 886, 15

Tomisaka K., 2014, ApJ, 785

Tomisaka K., Ikeuchi S., 1983, PASJ, 35, 187

Truelove J. K., Klein R. I., McKee C. F., Holliman John H. I., Howell L. H., Greenough J. A., 1997, ApJ, 489, L179

Vaidya B., Hartquist T. W., Falle S. A. E. G., 2013, MNRAS, 433, 1258

Vishniac E. T., 1994, ApJ, 428, 186

Wolfire M. G., Hollenbach D., McKee C. F., Tielens A. G. G. M., Bakes E. L. O., 1995, ApJ, 443, 152

Xu S., Ji S., Lazarian A., 2019, ApJ, 878, 157

Yamada R. I., et al., 2022, MNRAS,

Zucker C., et al., 2022, Nature, 601, 334

Zuckerman B., Evans N. J. I., 1974, ApJ, 192, L149